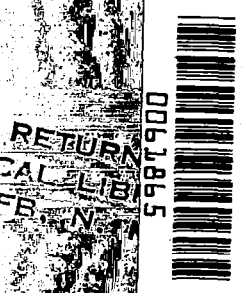

NASA Contractor Report 3035

A Method for Predicting Full Scale Buffet Response With Rigid Wind Tunnel Model Fluctuating Pressure Data

Volume I: Prediction Method Development and Assessment

Atlee M. Cunningham, Jr., David B. Benepe,
Darlene Watts, and Paul G. Waner

CONTRACT NAS2-7091
NOVEMBER 1978

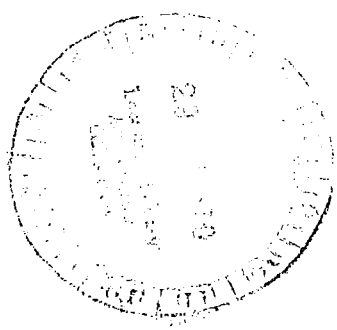

NASA

NASA Contractor Report 3035

A Method for Predicting Full Scale Buffet Response With Rigid Wind Tunnel Model Fluctuating Pressure Data

Volume I: Prediction Method Development and Assessment

Atlee M. Cunningham, Jr., David B. Benepe,
Darlene Watts, and Paul G. Waner
General Dynamics Corporation
Fort Worth, Texas

Prepared for
Ames Research Center
under Contract NAS2-7091

NASA
National Aeronautics
and Space Administration

Scientific and Technical
Information Office

1978

A METHOD FOR PREDICTING FULL SCALE BUFFET RESPONSE WITH RIGID WIND TUNNEL MODEL FLUCTUATING PRESSURE DATA

VOLUME I

PREDICTION METHOD DEVELOPMENT AND ASSESSMENT

By
Atlee M. Cunningham, Jr., David B. Benepe,
Darlene Watts, and Paul G. Waner
Fort Worth Division of General Dynamics

Abstract

This report documents the development and assessment of a method with which fluctuating pressure data obtained from rigid scaled wind-tunnel models can be used to predict flexible full-scale buffet response. The method requires unsteady aerodynamic forces, natural airplane modes, and the measured pressure data as input. A gust response computer program is used to calculate buffet response due to the forcing function posed by the measured pressure data. By calculating both symmetric and antisymmetric solutions, upper and lower bounds on full-scale buffet response are formed. Final results are given in the form of upper and lower bounds on the power spectral densities and the RMS values for angle of attack variation in maneuvers at several Mach-altitudes. Comparisons of predictions with flight test results are made and the effects of horizontal tail loads and static aeroelasticity are shown. Discussions are also presented on the effects of primary wing torsion modes, chordwise and spanwise phase angles, and altitude.

This first volume presents a description of the prediction method, how the method was evolved, and comparisons of predicted rms responses with flight test data for assessing the capability of the method. Included with the comparisons are complete descriptions of the flight test maneuver and data points, airplane conditions, and calculated modes and wind-tunnel data points used in the prediction. The second volume presents the power spectral density plots made for all of the predictions.

Abstract (continued)

The supporting analysis of F-111A flight data was conducted in two phases. Phase I concentrated on wing and fuselage buffeting response at a wing leading edge sweep of 26 degrees and subsonic speeds and supported the initial development of the the prediction method. That work is reported in three contractor reports.

Benepe, D. B., Cunningham, A. M., Jr., and Dunmyer, W. D.: An investigation of Wing Buffeting Response at Subsonic and Transonic Speeds: Phase I F-111A Flight Data Analysis.

Volume I - Summary of Technical Approach, Results and Conclusions, NASA CR-152109.

Volume II - Plotted Power Spectra, NASA CR-152110.

Volume III - Tabulated Power Spectra, NASA CR-152111.

Phase II extended the analysis effort to wing leading edge sweeps of 50 and 72.5 degrees at both subsonic and low supersonic speeds and provided data for assessing horizontal tail response and evaluating the final prediction method. The Phase II effort is reported in three additional contractor reports.

Benepe, D. B., Cunningham, A. M., Jr., Traylor, S., Jr., and Dunmyer, W. D.: An Investigation of Wing Buffeting Response at Subsonic and Transonic Speeds: Phase II F-111A Flight Data Analysis.

Volume I - Summary of Technical Approach, Results and Conclusions, NASA CR-152112.

Volume II - Plotted Power Spectra, NASA CR-152113.

Volume III - Tabulated Power Spectra, NASA CR-152114.

CONTENTS

	Page
LIST OF TABLES	v
LIST OF FIGURES	vii
SUMMARY	1
INTRODUCTION	1
SYMBOLS	3
THE PREDICTION METHOD	5
Existing Dynamic Response Capability	5
Computation of normal modes	5
Mode interpolation and computation of generalized masses	6
Computation of unsteady aerodynamics	7
Computation of $[Q_{rs}]$ and $\{\overline{F}_r\}$ at additional frequencies	8
Computation of dynamic response	9
The Buffet Forcing Function	14
Calculation of static aeroelastic effects	14
Conversion of wind tunnel data to pressure distributions	15
Calculation of the horizontal tail buffet pressures	19
Calculation of the buffet forcing function and response terms	21
Buffet Response Prediction	22

Page

EVOLVMENT OF THE PREDICTION METHOD 23

Effects of Static Aeroelasticity 23

Asymmetric Responses 24

Effect of Horizontal Tail Loads 25

Effect of Buffet Pressure Spanwise and Chordwise Phasing 26

The Influence of Wing Torsional Motion 28

Effect of Maneuver Transients 30

CAPABILITY ASSESSMENT OF THE METHOD 31

Prediction Results 33

Case 1 33

Case 2 34

Case 3 34

Case 4 35

Case 5 35

Case 6 35

Case 7 35

Summary of the Capability Assessment 36

CONCLUSIONS 37

REFERENCES 38

LIST OF TABLES

Table	Title	Page
1	BY7 ANALYSIS/TEST COMPARISON OF F-111A SYMMETRIC VIBRATION FREQUENCIES, $\Lambda = 26^{o}$	40
2	BY7 ANALYSIS/TEST COMPARISON OF F-111A ANTISYMMETRIC VIBRATION FREQUENCIES, $\Lambda = 26^{o}$	41
3	CROSS REFERENCE FOR CASE NUMBERS AND TABLES AND FIGURES	43
4	CASE 1, WING ALONE, $\Lambda = 26^{o}$, M = 0.80, ALT = 6035m (19,800 FT)	43
5	CASE 2, TOTAL AIRPLANE (HALF HORIZONTAL TAIL), $\Lambda = 26^{o}$, M = 0.80, ALT = 6035m (19,800 FT)	44
6	CASE 3, TOTAL AIRPLANE (FINAL METHOD), $\Lambda = 26^{o}$, M = 0.70, ALT = 7559m (24,800 FT)	44
7	CASE 4, TOTAL AIRPLANE (FINAL METHOD), $\Lambda = 50^{o}$, M = 0.85, ALT = 8382m (27,500 FT)	45
8	CASE 5, TOTAL AIRPLANE (FINAL METHOD), $\Lambda = 72.5^{o}$, M = 0.85, ALT = 7285m (23,900 FT)	45
9	CASE 6, WING ALONE (FINAL METHOD), $\Lambda = 50^{o}$, M = 1.20, ALT = 9053m (29,700 FT)	46
10	CASE 7, WING ALONE (FINAL METHOD), $\Lambda = 72.5^{o}$, M = 1.20, ALT = 9083m (29,800 FT)	46

LIST OF FIGURES

Figure	Title	Page
1	Buffet Prediction Method Flow Diagram	47
2	Approximation for the Real Part of Q_{11} Term for Wing Translation - Comparison with Calculated Values	48
3	Approximation for the Real Part of Q_{12} Term for Wing Translation and Pitch - Comparison with Calculated Values	49
4	Effect of Wing Flexibility on the Lift Curve Slope for the F-111A	50
5	Conversion of Wind Tunnel Pressure PSDs into Complex Pressure Distributions	
	(a) Relationship Between the NASA ARC Spectral Density Analysis and the Pressure Transducer Locations	51
	(b) Spline Fit of Model Pressure for $M = 0.80$, $\alpha = 10.18^{\circ}$ and $f_{model} = 48.0$ Hz	51
6	Rigid and Flexible Wing Bending for $\Lambda = 26^{\circ}$, $M = 0.80$, ALT = 6035m	52
7	Predicted Bounds on Wing Tip Accelerometer PSD for $\Lambda = 26^{\circ}$, $M = 0.80$, ALT = 6035m	53
8	Predicted Bounds on Wing Bending PSD for $\Lambda = 26^{\circ}$, $M = 0.80$, ALT = 6035m	54
9	Effect of Horizontal Tail Loads on Wing Shear for $\Lambda = 26^{\circ}$, $M = 0.80$, ALT = 6035m	55
10	Effect of Horizontal Tail Loads on Wing Tip Accelerometer for $\Lambda = 26^{\circ}$, $M = 0.80$, ALT = 6035m	56
11	Effect of Horizontal Tail Loads on C.G. Accelerometer for $\Lambda = 26^{\circ}$, $M = 0.80$, ALT = 6035m	57

Figure	Title	Page
12	Effect of Buffet Pressure Spanwise and Chordwise Phasing on Wing Alone Response PSDs for $\Lambda = 26^{o}$, M = 0.80, ALT = 6035m	
	(a) $\alpha = 6.6^{o}$	58
	(b) $\alpha = 11.1^{o}$	59
	(c) $\alpha = 14.4^{o}$	60
13	Effect of Buffet Pressure Spanwise and Chordwise Phasing on Wing Alone Response RMS and N_{O} Results for $\Lambda = 26^{o}$, M = 0.80, ALT = 6035m	
	(a) Accelerometer Response	61
	(b) Wing Loading Response	62
14	Effect of Matching Torsion Mode Frequencies and Total Airplane Aerodynamics on Wing Torsion Response	
	(a) Wing Alone with Direct Frequency Scaling	63
	(b) Wing + Full Tail with Matched Torsion Frequencies	63
	(c) Wing + Half Tail with Matched Torsion Frequencies	63
15	Flight Parameters for the Flight 79 Maneuver	64
16	Comparison of Flight Test and Predicted Response for Wing Tip Accelerometer During the Flight 79 Maneuver	
	(a) $\alpha_{FLT} = 7.5^{o}$	65
	(b) $\alpha_{FLT} = 8.9^{o}$	65
	(c) $\alpha_{FLT} = 10.4^{o}$	65
17	Calculated Symmetric Natural Modes for Cases 1 and 2, $\Lambda = 26^{o}$ and G.W. = 266,044N	66
18	Calculated Antisymmetric Natural Modes for Cases 1 and 2, $\Lambda = 26^{o}$ and G.W. = 266,044N	70
19	Response Predictions for Case 1	74
20	Response Predictions for Case 2	77

Figure	Title	Page
21	Calculated Symmetric Natural Modes for Case 3, $\Lambda = 26^{o}$ and G.W. = 293,138N	81
22	Calculated Antisymmetric Natural Modes for Case 3, $\Lambda = 26^{o}$ and G.W. = 293,138N	85
23	Response Predictions for Case 3	90
24	Calculated Symmetric Natural Modes for Case 4, $\Lambda = 50^{o}$ and G.W. = 331,392N	94
25	Calculated Antisymmetric Natural Modes for Case 4, $\Lambda = 50^{o}$ and G.W. = 331,392N	98
26	Response Predictions for Case 4	103
27	Calculated Symmetric Natural Modes for Cases 5 and 7, $\Lambda = 72.5^{o}$ and G.W. = 268,673N	107
28	Calculated Antisymmetric Natural Modes for Cases 5 and 7, $\Lambda = 72.5^{o}$ and G.W. = 268,673N	111
29	Response Predictions for Case 5	116
30	Calculated Symmetric Natural Modes for Case 6, $\Lambda = 50^{o}$ and G.W. = 261,778N	120
31	Calculated Antisymmetric Natural Modes for Case 6, $\Lambda = 50^{o}$ and G.W. = 261,778N	124
32	Response Predictions for Case 6	129
33	Response Predictions for Case 7	132
34	Frequency of Flight Test Data Distribution as Fraction of Upper Bounds	135

A METHOD FOR PREDICTING FULL SCALE BUFFET RESPONSE WITH RIGID WIND TUNNEL MODEL FLUCTUATING PRESSURE DATA

VOLUME I

PREDICTION METHOD DEVELOPMENT AND ASSESSMENT

By
Atlee M. Cunningham, Jr., David B. Benepe,
Darlene Watts, and Paul G. Waner
Fort Worth Division of General Dynamics

Abstract

This report documents the development and assessment of a method with which fluctuating pressure data obtained from rigid scaled wind-tunnel models can be used to predict flexible full-scale buffet response. The method requires unsteady aerodynamic forces, natural airplane modes, and the measured pressure data as input. A gust response computer program is used to calculate buffet response due to the forcing function posed by the measured pressure data. By calculating both symmetric and antisymmetric solutions, upper and lower bounds on full-scale buffet response are formed. Final results are given in the form of upper and lower bounds on the power spectral densities and the RMS values for angle of attack variation in maneuvers at several Mach-altitudes. Comparisons of predictions with flight test results are made and the effects of horizontal tail loads and static aeroelasticity are shown. Discussions are also presented on the effects of primary wing torsion modes, chordwise and spanwise phase angles, and altitude.

This first volume presents a description of the prediction method, how the method was evolved, and comparisons of predicted rms responses with flight test data for assessing the capability of the method. Included with the comparisons are complete descriptions of the flight test maneuver and data points, airplane conditions, and calculated modes and wind-tunnel data points used in the prediction. The second volume presents the power spectral density plots made for all of the predictions.

quite low when compared with the maneuver loads spectrum. Local loadings can be high, however, and can result in troublesome but not usually serious secondary structural fatigue. As a result, the prime concern with high intensity buffet is the dynamic response caused by buffeting loads and how it limits the operational envelope of the total airplane system.

The buffet problem, particularly transonic buffet, has received increased interest in government and airframe industry supported research programs. The Air Force Flight Dynamics Laboratory and the NASA Langley, Ames, and Flight Research Centers have supported many flight test, wind tunnel, and theoretical investigations aimed at developing the capability to better understand and predict buffet characteristics of new aircraft designs. Diverse opinions among the investigators has led to much confusion on the nature of the buffet problem and how characteristics may be predicted. All prediction methods currently in use are semi or purely empirical with which buffet onset can be predicted with fair accuracy. The problem of predicting buffet intensity is far more complex and requires consideration of many factors besides the aerodynamics of separated flow.

A wind tunnel study was conducted at NASA Ames Research Center to determine the nature of fluctuating pressures during buffeting flow at subsonic and transonic speeds (ref. 1). The model used was a rigid 1/6 scale semispan model of the F-111A. The wing had variable sweep and was heavily instrumented with high response pressure transducers. It was desired to correlate the model data with flight test results; however, this was no simple task.

A supporting study was initiated at the Fort Worth Division of General Dynamics for NASA to collect and analyze flight test data for correlation and to develop a means for performing the correlations. Since the principle objective of the total program was to better understand the mechanics of high intensity buffet, the F-111A was an ideal test bed because of the large amount of flight test data available from the loads program and the wide variety of Mach-altitude-wing sweep configurations available. Some results of analysis of this flight test data are given in references 2 and 3. The complete results of the flight test data analyzed are given in reference 4. These results were invaluable in the development of the prediction method to be given in this report.

This report documents the development and assessment of a method with which fluctuating pressure data obtained from rigid scaled wind-tunnel models can be used to predict flexible full-scale buffet response. The method requires unsteady aerodynamic forces, natural airplane modes, and the measured pressure data as input. A gust response computer program is used to calculate buffet response due to the forcing function posed by the measured pressure data. This method is similar to that given in reference 5 except that the latter does not include aerodynamic forces due to airplane rigid and elastic motions. By calculating both symmetric and antisymmetric solutions, upper and lower bounds on full-scale buffet response are formed. Final results are given in the form of upper and lower bounds on the power spectral densities and the RMS values for angle of attack variation in maneuvers at several Mach-altitudes. Comparisons of predictions with flight test results are made and the effects of horizontal tail loads and static aeroelasticity are shown. Discussions are also presented on the effects of primary wing torsion modes, chordwise and spanwise phase angles, and altitude.

The report is broken up into two volumes. The first volume presents a description of the prediction method, how the method was evolved, and comparisons of predicted rms responses with flight test data for assessing the capability of the method. Included with the comparisons are complete descriptions of the flight test maneuver and data points, airplane conditions, and calculated modes and wind-tunnel data points used in the prediction. The second volume is composed primarily of the power spectral density plots made for all of the predictions. On these plots, the flight test power spectral density distributions are shown for a detailed comparison. Included with the plots are repeats of the flight test and prediction conditions for each case.

SYMBOLS

b_r	reference length
$\overline{F}_r$	aerodynamic loading or moment due to the rth mode
$\overline{F}_B$	aerodynamic loading or moment due to the buffeting pressure field

$h_r(x,y)$	deflection of the r^{th} mode at point x,y
$\sigma_m(x,y)$	mass concentrated at point x,y
M	free stream Mach number
M_{rs}	generalized mass in the modal coordinates for the airplane dynamic model
N_o	characteristic frequency (frequency centroid of the power spectral density distribution)
q	free stream dynamic pressure
$\overline{q}_r$	generalized coordinate
Q_{rs}	generalized force in the rth mode due to aerodynamics in the s^{th} mode
Q_{rB}	generalized force in the rth mode due to the buffeting pressure field
α	wing angle of attack
$\Delta p(x,y,\omega)$	buffeting pressure amplitude at point x,y and frequency ω
$\theta_{ij}(\omega)$	phase angle between points i and j for the buffeting pressure field at frequency ω
Λ	wing sweep angle
$\phi_i(\omega)$	power spectra of the buffeting pressure field at point i and frequency ω
ω	circular frequency

THE PREDICTION METHOD

A method has been developed for predicting full scale buffet response characteristics by the use of wind tunnel buffet pressure measurements on rigid models and conventional gust response analysis methods. The wind tunnel pressure data is in the form of power spectral densities (PSDs) for each pressure transducer. Phase relationships (phase angles, θ_{ij}) are available from cross power spectral densities (CPSDs) between pressure transducers. From the PSDs and phase angles, θ_{ij}, complex pressure distributions over the wing are constructed. The structural characteristics are obtained from a math model of the airplane with the proper mass distribution for the flight condition being analyzed. Aerodynamic stiffness and damping for the desired Mach-altitude condition are computed from oscillatory lifting surface theory based on linearized uniform potential flow. All of these items are combined into the dynamic equations which are solved in the conventional manner of gust response analyses.

The relationships between the above functions are shown in figure 1. Each block represents an individual computer program or computer run. The unsteady aerodynamic terms, $[Q_{rs}]$ and $\{\overline{F}_r\}$ are both computed with the same program. These terms are also expanded in frequency with a single program. Likewise, the buffet forcing function terms $\{Qf_B\}$ and $\{\overline{F}_B\}$ are calculated in the same manner. Each program used in the flow diagram will be described in the following subsections where major emphasis will be placed on the programs to convert wind tunnel data and to calculate the wing and tail pressures at the aerodynamic panel points.

Existing Dynamic Response Capability

The dynamic response capability at the Fort Worth Division is composed of several computer programs, all of which together represent a state-of-the-art capability, typical of the major airframe companies. The basic programs are described in the following paragraphs.

Computation of normal modes.- Normal modes of vibration are computed with a two-dimensional finite-element computer program with the Fort Worth Division designation of BY7 (ref. 6). The BY7 program computes a matrix of stiffness influence coefficients

for arbitrary vehicle configuration components such as wing surfaces, vertical and horizontal tail surfaces, and control surfaces. The procedure also has an anisotropic capability. When appropriate mass data is supplied, normal modes can be computed for cantilevered vehicle components or an entire vehicle with free-free boundary conditions.

The main reasons for using the BY7 program rather than NASTRAN are economy and convenience. Although NASTRAN has been set up at the Fort Worth Division and routinely used since 1970 it has been found that for airfoil type surfaces, the cost increases by an order of magnitude with little or no gain in accuracy when compared with the BY7 program. Perhaps the strongest reason for not using NASTRAN is that a math model had been previously set up of the F-111A/FB-111A for BY7 (ref. 7). Tables 1 and 2 show the comparison between the predicted frequencies obtained with the BY7 math model and those from ground vibration tests for Airplane #12. The total vehicle was represented with free-free boundary conditions. The closeness of agreement clearly illustrates how well the model represents the airplane.

Mode interpolation and computation of generalized masses.- Mode interpolation for the unsteady aerodynamic programs is accomplished with a surface spline method which is applicable to entire airplane configurations. The method is based on the surface spline technique of Harder and Desmarais (ref. 8). The interpolation procedure also calculates the generalized mass terms, M_{rs}, with the following equation

$$M_{rs} = \frac{1}{4 \rho b_r^3} \iint_A h_r(x,y)\ h_s(x,y)\ \sigma_M(x,y)\ d\,x\,dy$$

where

ρ = density

b_r = reference length

$h_r(x,y), h_s(x,y)$ = deflection of the r^{th}, s^{th} modes at point x,y

$\sigma_M(x,y)$ = mass distribution per unit area.

Computation of unsteady aerodynamics.- Several programs are available for computing unsteady aerodynamics based on linear potential flow theory. These include kernel function methods as well as the doublet lattice and Mach box methods.

The subsonic doublet lattice method (ref. 9) as it exists at the Fort Worth Division is designated as procedure TS5. This program has the capability of treating up to ten trapezoidal surfaces lying in the same plane. Thus, planar representations of wing-body-horizontal tail configurations can be achieved as has been demonstrated in previous work. As will be discussed later, this program is used to compute total airplane aerodynamics and make estimates of loads induced on the horizontal tail due to buffet loads on the wing.

Supersonic aerodynamics are calculated with a Mach box procedure based on the method of Pines and Dugundji (ref. 10). This procedure, designated as BQ8 at the Fort Worth Division, is limited to wing alone configurations. Hence, the supersonic response predictions in this report are limited to wing alone simulations.

The aerodynamic programs are used to compute the generalized force matrices, $[Q_{rs}]$. These terms are computed as

$$Q_{rs}(\omega) = \frac{1}{4\rho b_r^3 \omega^2} \iint_{A_W} hr(x,y)\left[-\Delta p_s(x,y,\omega)\right] dxdy$$

where

ρ = density

b_r = reference length

ω = exciting frequency

$h_r(x,y)$ = deflection of the r^{th} mode at point x,y

$\Delta p_s(x,y,w)$ = pressure distribution amplitude induced at point x,y by the s^{th} mode oscillating at frequency, ω

A_W = wing area

Other terms that are computed are the $\overline{F}_r$ terms which represent aerodynamic loads, moments, and stresses induced by each mode for response calculations. These terms will be discussed in the section on dynamic response.

Computation of $[Q_{rs}]$ and $\{\overline{F}_r\}$ at additional frequencies.- The dependence of the $[Q_{rs}]$ and $\{\overline{F}_r\}$ terms on frequency is implicit and very complex. The variation with frequency is generally quite smooth, however, and is easily amendable to interpolation or approximation schemes with a high degree of confidence.

An approximation scheme has been developed at the Fort Worth Division which has proven to be very dependable and efficient (ref. 11). The method uses a parabolic fit to condition the terms near zero frequency. The conditioned terms are then fitted with Tschebychev polynomials of the first kind for up to 10 fitting points. By the use of an exponential transformation, the approximation becomes theoretically valid for the frequency range $0 < \omega < \infty$. In practice, the upper and lower values input are used as the real limits.

Shown in figures 2 and 3 are some examples of application of the approximation scheme. The Q11 term shown in figure 2 is the real part generalized force resulting from a rectangular wing of aspect ratio 2 oscillating in a unit translation mode for M=1.2. The circles are the fitting points and the squares are values computed at other points. As can be seen, the approximation is quite good at off-fitting points. In figure 3, the real part of Q12 is shown where the second mode is wing pitch about its leading edge. With the approximation fitted at the circle symbols, the agreement with the square symbols is again quite good.

This method was used to expand the $[Q_{rs}]$ and $\{\overline{F}_r\}$ terms as calculated with the unsteady aerodynamic programs. The calculated values were obtained at six fitting points and expanded to match the full scale frequencies of the wind tunnel model data. The approximation method is available in the doublet lattice procedure, TS5, and is usable as a separate capability if desired.

Computation of dynamic response.- The dynamic response procedure, designated as SB2 at the Fort Worth Division, solves the equations of motion for such linear systems as a total airplane subjected to an arbitrary harmonic forcing function (ref. 12). The airplane must be balanced aerodynamically, thus, rigid body motions are obtained as well as elastic response motions. The equations of motion are expressed in terms of generalized coordinates. In matrix notation, this becomes

$$\begin{Bmatrix} \bar{q}_1 \\ \bar{q}_2 \\ \cdot \\ \cdot \\ \cdot \\ \bar{q}_{Nq} \end{Bmatrix} = - \begin{bmatrix} A_{11} & A_{12} & \cdots & A_{1Nq} \\ A_{21} & A_{22} & \cdots & A_{2Nq} \\ \cdot & \cdot & & \cdot \\ \cdot & \cdot & & \cdot \\ \cdot & \cdot & & \cdot \\ A_{Nq1} & A_{Nq2} & \cdots & A_{NqNq} \end{bmatrix}^{-1} \begin{Bmatrix} Q_{1_f} \\ Q_{2_f} \\ \cdot \\ \cdot \\ \cdot \\ Q_{Nq_f} \end{Bmatrix}$$

or

$$\left\{ \bar{q}_r \right\} = - \left[A \right]^{-1} \left\{ Q_{r_f} \right\}$$

where

$$A_{rr} = \left[1 - \left(\frac{\omega_r}{\omega} \right)^2 (1 + i\, g_r) - i2\gamma_r \left(\frac{\omega_r}{\omega} \right) \right] M_{rr} + Q_{rr}, \quad r=s$$

$$A_{rs} = M_{rs} + Q_{rs}, \quad r \neq s$$

ω = exciting frequency, rad/sec

ω_r = undamped natural frequency of the r^{th} normal mode, rad/sec

g_r = structural damping coefficient for the r^{th} mode (usually assumed as $g_r = 0.03$)

γ_r = ratio of viscous damping to critical damping

N_q = total number of generalized coordinates or degrees of freedom, $1 \leq N_q \leq 20$

M_{rs} = generalized mass as described previously

Q_{rs} = generalized work of the unsteady aerodynamic loads on the oscillating airplane as described previously

Q_{rf} = generalized work of the forcing function on the oscillating airplane

$i = \sqrt{-1}$.

The Q_{rf} terms are computed in the same manner as the Q_{rs} terms where $\Delta pf(x,y)$ of the forcing function is used in the integral rather than $\Delta p_s(x,y)$.

Once the equation of motion is solved for each frequency of the forcing function, the $\{\bar{q}_r\}$ are obtained with which deflections, velocities, accelerations, loads, moments, or stresses can be computed.

Normally, in procedure SB2, the response characteristics are computed as transfer functions in terms of response per unit input as a function of frequency. Total response is then calculated with an input spectrum of the forcing function (a Dryden or Von Karman gust spectrum, etc.) to yield an output spectrum. The transfer function, $H_L(\omega)$, for the L^{th} point and exciting frequency, ω, is expressed as

$$H_L(\omega) = \sum_{r=1}^{N_q} \left[(i\omega)^p F_{rL} + \bar{F}_{rL}(\omega) \right] \bar{q}_r$$

$$+ (i\omega)^p F_{fL} + \bar{F}_{fL}(\omega)$$

where

N_q = number of degrees of freedom or modes $(1 \leq N_q \leq 20)$

$(i\omega)^p F_{rL}$ = inertia component of the response in each mode where p is a function of the type of response item

$\overline{F}_{rL}(\omega)$ = load, moment, or stress component of the response in the r^{th} mode

$(i\omega)^p F_{fL}$ = inertia component of the response due to the forcing function

$\overline{F}_{fL}(\omega)$ = load, moment, or stress component of the response due to the forcing function

The above terms will be discussed in more detail.

The first term, $(i\omega)^p F_{rL}$, which is the contribution of inertia to the L^{th} response point, will vary in form depending on the type of response desired. If acceleration response is desired at the L^{th} point, then $p = 2$ and $F_{rL} = h_{rL}$ or

$$(i\omega)^p F_{rL} = (i\omega)^2 h_{rL}$$

where h_{rL} is the deflection of the r^{th} mode at point L. If velocity or displacement is desired then $p = 1$ or 0, respectively. For loads computation, $p = 2$, and F_{rL} is defined for shear as

$$\left[(i\omega)^p F_{rL}\right]_{SHEAR} = -\omega^2 \iint_{A_L} m(x,y)hr(x,y)\, dxdy$$

where

$m(x,y)$ = mass distribution

$h_r(x,y)$ = r^{th} mode shape

A_L = area for calculating the total shear

The area, A_L, is defined by the planform and the station and axis at which the shear is desired. For bending moment, F_{rL} becomes

$$\left[(i\omega)^p F_{rL}\right]_{B.M.} = -\omega^2 \iint_{A_L} (Y-Y_{REF})^* m(x,y)h_r(x,y)\, dxdy$$

where $(Y-Y_{REF})^*$ is the moment arm perpendicular to the bending moment axis. Likewise, torsion is defined as

$$\left[(i\omega)^p F_{rL}\right]_{TORS.} = -\omega^2 \iint_{A_L} (X-X_{REF})^* \, m(x,y) h_r(x,y) \, dxdy$$

where again $(X-X_{REF})^*$ is the moment arm perpendicular to the torsion axis.

The second term, $\overline{F}_{rL}(\omega)$, is simply the total aerodynamic load, moment, or stress induced at the L^{th} point due to the motion of the r^{th} mode. For the computation of displacements, velocities and accelerations, $\overline{F}_{rL}(\omega)$ is set to zero. It is expressed as

$$\overline{F}_{rL}(\omega) = \iint_{A_L} \Delta p_r(x,y) \, f_L(x,y) \, dxdy$$

where

$\Delta p_r(x,y)$ = unsteady aerodynamic pressure distribution induced by the r^{th} mode of unit amplitude

$$f_L(x,y) = \begin{cases} 1 & \text{, shear} \\ (Y-Y_{REF})^* & \text{, bending moment} \\ (X-X_{REF})^* & \text{, torsion} \end{cases}$$

The terms for $f_L(x,y)$ are the same as those used in the computation of F_{rL}.

The third term, $(i\omega)^p F_{fL}$, is the inertia component which is due to the forcing function. For gust response, this term is zero, hence it is also zero for buffet response. Cases for which the term is non-zero are response due to forced control oscillation, forced fuel sloshing, or internal inertial shakers for flutter testing. The expression for $(i\omega)^p F_{fL}$ is identical to that for $(i\omega)^p F_{rL}$.

The fourth term, $\overline{F}_{fL}(\omega)$, is the aerodynamic load, moment or stress induced at the L^{th} point by the forcing function. This term is also zero if displacements, velocities, or accelerations are being computed. The expression is

$$\overline{F}_{fL}(\omega) = \iint_{A_L} \Delta p_f(x,y)\ f_L(x,y)\ dxdy$$

where $\Delta p_f(x,y)$ is the loading distribution of the forcing function and f_L is as defined previously.

For the present task of calculating buffet response, the input forcing function is actually "shaped" as will be shown in the next section. Thus, the transfer function as computed from the above quantities will not be a true transfer function but will instead be the square root of the power spectral density. This is seen from the expression for calculating the output spectrum, $\phi_2(\omega_i)$, resulting from the effect of a transfer function, $H_{21}(\omega_i)$ on an input spectrum, $\phi_1(\omega_i)$:

$$\phi_2(\omega_i) = \left[H_{21}(\omega_i)\right]^2 \phi_1(\omega_i)$$

In the case of buffet response, the ϕ_1 is set to a constant value of unity, i.e.,

$$\phi_1(\omega_i) = 1.0, \quad \omega_1 \leq \omega_i \leq \omega_k$$

where ω_1 and ω_k are the first and last frequencies in the spectrum being analyzed.

Results from SB2 are in the form of a PSD, total RMS, and N_O of each response item. Other data are also output, however, they are not of major interest at this point. The RMS values are calculated over the frequency range of the prediction, hence comparisons with flight test data must be made over the same frequency range. The N_O values are also calculated over the same range. This term represents the total number of times that the function being analyzed crosses the mean axis with a positive slope. Hence, N_O is a characteristic frequency. Where RMS is calculated as

$$RMS = \left[\sum_{i=1}^{K} (\Delta\omega)_i\ \phi(\omega_i) \right]^{\frac{1}{2}}$$

N_o is calculated as

$$N_o = \frac{\left[\sum_{i=1}^{K} \omega_i^2 \, (\Delta\omega)_i \, \phi \, (\omega_i) \right]^{\frac{1}{2}}}{RMS}$$

In addition to the PSD, the integrated quantities, RMS and N_o, provide a convenient means for comparison with flight test.

The next section will describe the process by which the wind tunnel pressure PSD and CPSD data are combined with the structural modes to produce the $\{Q_{rf}\}$ and $\{\overline{F}_r\}$ terms used in the dynamic response program. In order to distinguish between the more conventional forcing function terms and those due to buffeting pressures, these terms are designated as $\{Q_{rB}\}$ and $\{\overline{F}_B\}$.

The Buffet Forcing Function

Referring to figure 1, the process of converting wind tunnel data PSDs and phase angles into generalized forces is a three step process. First the wind tunnel data is transformed into a complex pressure distribution over the wing for each frequency at which a PSD estimate is made. These pressures are then interpolated at the load points on the doublet lattice panels. The interpolated values are used in conjunction with the doublet lattice unsteady aerodynamic matrices to calculate estimated pressures induced on the horizontal tail by downwash produced by the wing buffet pressures. Finally, the wing and tail pressures are used in the doublet lattice program to calculate the generalized forcing function terms, $\{Q_{rB}\}$, and the response terms, $\{\overline{F}_B\}$, for shear, bending moment and torsion on the wing and tail.

The following paragraphs will describe (1) the means by which static aeroelastic effects are accounted for, (2) conversion of the wind tunnel data, (3) calculation of horizontal tail buffet pressures, and (4) calculation of the generalized forcing function and response terms.

Calculation of static aeroelastic effects.- The wind tunnel buffet pressure data is obtained from a rigid model and hence does not represent the flexible airplane in flight. In order to

approximately account for the static aeroelastic effects, the rigid angle of attack values, α_{RIG}, used to obtain the wind tunnel data are modified with theoretical results taken from aeroelastic analyses of the F-111A. The appropriate flexible to rigid lift coefficient ratio is used to calculate the angle of attack, α_{FLEX}, required for the flexible airplane to produce the equivalent lift that would be produced by the rigid airplane at α_{RIG}.

The flexible to rigid ratios used in this study are summarized in figure 4 for the three wing sweeps considered. The values for α_{FLEX} are calculated as

$$\alpha_{FLEX} = \frac{\alpha_{RIG}}{\left(\frac{C_{L\ FLEX}}{C_{L\ RIG}}\right)_{M,\ h,\ \Lambda}}$$

for the desired Mach-altitude-wing sweep condition. Thus, the buffet response calculated for a given wind tunnel model angle of attack, α_{RIG}, is used as a prediction for an airplane angle of attack, α_{FLEX}.

This technique is not exact in that it assumes that the aeroelastic twist has no effect on changing the buffet pressure distributions, that is, the buffeting forces are directly related to total normal forces on the wing. It is suspected that aeroelastic twist tends to "soften" the buffeting pressures which makes the above assumption conservative. If the suspicion is correct, then even the predictions which are shifted in α due to gross aeroelastic effects should overpredict flight test results. Since the results which will be presented later in this report are overpredicted, it is felt that this reasoning may be valid, however, further research is needed in this area.

Conversion of wind tunnel data to pressure distributions.- The wind tunnel data which is used to generate buffet forcing functions in the prediction method is received on magnetic tape as a collection of PSDs, CPSDs, phase angles, coherency functions and convection velocities. The data is available for multiple sets of three pressure transducers which are referred to as x, y and z. A complete coverage of the transducers on the wing is available for each Mach and angle of attack condition. The means by which this data is processed into complex pressure

distributions over the wing is embodied in a computer program, the methodology of which will be described below.

The only data that are used on the magnetic tape are the PSDs, $\phi_m(\omega_i)$, and the phase angles, $\theta_{mn}(\omega_i)$. These quantities are combined to obtain complex pressure distributions in the manner illustrated in the following example for a chordwise distribution. Consider the two dimensional distribution in figure 5a where six transducers are located along the chord. Because the data processing used at NASA ARC on the wind tunnel data requires that the data be composed of sets of three items, three sets are used to describe the $\phi_m(\omega_i)$ and $\theta_{mn}(\omega_i)$ for the example as shown. The first set translates to

$$(\phi_x , \phi_y , \phi_z)_1 = (\phi_1 , \phi_2 , \phi_3)$$

$$(\theta_{xy}, \theta_{xz}, \theta_{yz})_1 = (\theta_{12}, \theta_{13}, \theta_{23})$$

the second set to

$$(\phi_x , \phi_y , \phi_z)_2 = (\phi_3 , \phi_4 , \phi_5)$$

$$(\theta_{xy}, \theta_{xz}, \theta_{yz})_2 = (\theta_{34}, \theta_{35}, \theta_{45})$$

and the third set to

$$(\phi_x , \phi_y , \phi_z)_3 = (\phi_5 , \phi_6 , \phi_7)$$

$$(\theta_{xy}, \theta_{xz}, \theta_{yz})_3 = (\theta_{56}, \theta_{57}, \theta_{67})$$

where each term is a function of frequency. The ϕ_7 may be a repeat of ϕ_6 or some other quantity which is not needed.

The main problem of translating the above data into a complex pressure function is determining the reference point from which the phase angle is measured. Currently, a point is chosen as the "leading edge" point and its phase angle is set at zero. Points which are forward of that location are nulled to zero in both phase and amplitude. In this manner the effect of shock induced separation can be simulated. The determination of the forward reference point is based on a scan of the PSDs and the coherency functions along the chord by the program user.

The coherency functions are usually low or show considerable scatter for points forward of the shock or the point of separation. Aft of the shock or separation point, the opposite is true which indicates good correlation particularly for adjacent transducers.

For the example, let the reference be the second transducer. Thus the amplitudes become

$$\phi_1 = 0.0 \qquad \theta_1 = 0.0$$

$$\phi_2 = \phi \qquad \theta_2 = 0.0$$

$$\phi_3 = \phi_3 \qquad \theta_3 = \theta_{23}$$

$$\phi_4 = \phi_4 \qquad \theta_4 = \theta_{23} + \theta_{34}$$

$$\phi_5 = \phi_5 \qquad \theta_5 = \theta_{23} + \theta_{34} + \theta_{45}$$

$$\phi_6 = \phi_6 \qquad \theta_6 = \theta_{23} + \theta_{34} + \theta_{45} + \theta_{56}$$

$$\phi_7 \text{ --------ignored-------} \qquad \theta_7 \text{ ----------}$$

and the complex pressure distribution is obtained as follows

$$\frac{\Delta p_1(\omega_i)}{q\sqrt{(\Delta\omega)_i}} = 0.0$$

$$\frac{\Delta p_2(\omega_i)}{q\sqrt{(\Delta\omega)_i}} = \left[\phi_2(\omega_i)\right]^{\frac{1}{2}}$$

$$\frac{\Delta p_3(\omega_i)}{q\sqrt{(\Delta\omega)_i}} = \left[\phi_3(\omega_i)\right]^{\frac{1}{2}} \text{EXP}\left[i\theta_3(\omega_i)\right]$$

$$\vdots$$

$$\frac{\Delta p_6(\omega_i)}{q\sqrt{(\Delta\omega)_i}} = \left[\phi_6(\omega_i)\right]^{\frac{1}{2}} \text{EXP}\left[i\theta_6(\omega_i)\right]$$

where the dependence on ω_i is indicated for clarity. The $(\Delta\omega)_i$ quantity is the finite bandwidth used in the NASA ARC spectral analysis. Its value changes as ω_i in order to provide a wide frequency coverage with a minimum of estimates.

Three important characteristics of the above scheme should be noted. First, the only phase angles used are those between adjacent transducers, i.e., only θ_{xy} or θ_{yz} are used. These are used primarily because the coherency between adjacent points is better which leads to a higher confidence in the cross correlations. Second, the items to be nulled are still used but set to zero and those to be ignored are discarded. Thus care must be exercised in the selection of points to insure that all points are used properly. And third, the $\sqrt{(\Delta\omega)_i}$ quantity is retained in the pressure distributions. This is done so that the resulting response transfer functions will be of the form $\sqrt{PSD}$ which eliminates points of confusion that would be caused by a varying $(\Delta\omega)_i$.

The only difference between the two-dimensional case described above and a three dimensional case for an entire wing is that several chords must be treated and the spanwise phase angle must be accounted for. In each chord a reference point is selected and a set of transducers is assigned. The phase angle construction then proceeds for each chord in the manner described above. The spanwise data is received in the same form of $\emptyset$ and θ for the running loads. These data are processed in the same manner as the chordwise data into the form of complex running load distributions. The reference point in the spanwise data is always taken to be the inboard chord station which has a zero phase angle. The spanwise data are used to determine the proper absolute phase angles for the chordwise data.

The spanwise data are physically calculated as integrals of the chordwise data at each span station. Thus, the phase angle of the integral of the processed chordwise pressure must be equal to that of the processed running loads data at its respective span station. Rather than calculate the phase angle change necessary to satisfy this condition at each span station, the complex chordwise pressures are processed directly as

$$\left[\frac{\Delta p_{nm}(\omega_i)}{q\sqrt{(\Delta\omega)_i}}\right]_{\theta_s} = \frac{\Delta p_{nm}(\omega_i)}{q\sqrt{(\Delta\omega)_i}} \frac{C_{\ell_m}}{|C_{\ell_m}|} \frac{\int \Delta p_m^*}{\left|\int \Delta p_m\right|}$$

where

$\left[\frac{\Delta p_{nm}(\omega_i)}{q\sqrt{(\Delta\omega)_i}}\right]_{\theta_s}$ = complex pressure value at the n^{th} chordwise point on the m^{th} span station with the desired absolute phase angle

$\frac{\Delta p_{nm}(\omega_i)}{q\sqrt{(\Delta\omega)_i}}$ = complex pressure value with phase angle referenced to zero at the leading edge independent of span station

$C_{\ell m}$ = complex running load at the m^{th} span station

Δp_m^* = complex conjugate of the chordwise integral of $\frac{\Delta p_{nm}(\omega_i)}{q\sqrt{(\Delta\omega)_i}}$

The final result from the wind tunnel data conversion program is a magnetic tape containing the following data:

(1) The reduced frequencies, $k_i = \frac{\omega_i b r}{U_\infty}$ for each spectral estimate, $k_1, \ldots k_K$.

(2) Complex pressure distribution, $\frac{\Delta p(x,y,\omega_i)}{q\sqrt{(\Delta\omega)_i}}$

.
.
.
.

(K + 1) Complex pressure distribution, $\frac{\Delta p(x,y,\omega_K)}{q\sqrt{(\Delta\omega)_K}}$

For K total frequencies. This tape is valid for a single Mach-alpha condition assuming that density and/or Reynold's number effects are of second order magnitude.

Calculation of the horizontal tail buffet pressures.- Horizontal tail buffet pressures were not measured in the wind tunnel test program (ref. 1). However, in the prediction of airplane buffet response, these data were needed for the forcing function. Thus, a method was developed with which the tail pressures could be estimated with linear theory aerodynamic

matrices. It was assumed that the wake in the vicinity of the horizontal tail due to buffeting pressures on the wing could be predicted with doublet lattice unsteady aerodynamic influence coefficients from a known wing load distribution. Such an assumption is not unreasonable for distances of several panel chords downstream.

In matrix form, the aerodynamic problem is

$$\begin{bmatrix} Aww & Awt \\ Atw & Att \end{bmatrix} \begin{Bmatrix} p_w \\ p_t \end{Bmatrix} = \begin{Bmatrix} W_w \\ W_t \end{Bmatrix}$$

where the aerodynamic influence coefficient submatrices are

A_{ww} = wing on wing
A_{wt} = tail on wing
A_{tw} = wing on tail
A_{tt} = tail on tail

and

$\{p_w\}$, $\{W_w\}$ = pressure and downwash on the wing

$\{p_t\}$, $\{W_t\}$ = pressure and downwash on the tail

Since the wing is buffeting, p_w is known from the wind-tunnel data as p_{wB}. The horizontal tail is usually at a negative angle of attack during a high-α maneuver; hence, it is assumed to be in a buffet free condition. Also, the tail upper surface is effectively the only portion feeling the buffeting wake from the wing upper surface; thus,

$$\tfrac{1}{2}\left[A_{tw}\right] \left\{P_{wB}\right\} + \left[A_{tt}\right] \left\{P_{tB}\right\} = \left\{W_t\right\} = 0$$

which yields

$$\left\{p_{tB}\right\} = -\tfrac{1}{2} \left[A_{tt}\right]^{-1} \left[A_{tw}\right] \left\{p_{wB}\right\}$$

With this form, all that is necessary to obtain p_{tB} from p_{wB} is to calculate the doublet lattice unsteady aerodynamic matrices (ref. 9) at the same frequencies for which wind tunnel data PSD estimates are made. In actual practice, the matrices are not calculated directly at all frequencies but are interpolated from

a smaller set since about forty frequencies are used. Otherwise the cost would be prohibitive.

Calculation of the buffet forcing function and response terms.- The doublet lattice program (ref. 9) is used to combine the buffet pressures with structural modes to obtain the generalized forcing function terms. It is also used to determine the shear, bending moment and torsion due to the buffet pressures for response calculations. The aerodynamic matrices generated by the doublet lattice program for the wing-tail unsteady aerodynamic pressures are also used to predict horizontal tail pressures due to the downwash produced by the wing buffet pressures in subsonic flow. Thus, the first step in obtaining these data items is to interpolate the wing buffet pressures from the transducer locations to the doublet lattice panel load points.

The interpolation of the buffet pressures is performed with a surface spline technique similar to that used to interpolate the structural mode shapes. The surface spline simulates the deflected shape of an infinite plate pinned at the points which are being interpolated from. The governing equation is

$$w_j = a_1 + a_2 x_j + a_3 y_j + \sum_{n=1}^{N} bn(rnj)^2 \ln\left|(n_j)^2\right|$$

For n=1, N where w_j is the function value at point (x_j,y_j) and

$$r_{nj}^2 = (x_n-x_j)^2 + (y_n-y_j)^2$$

The points (x_n,y_n) are the fitting points which in this case are the transducer locations. The coefficients $[a_1, a_2, a_3, b_1,\ldots b_N]$ are determined by equating the w_j to the known pressures at points $(x_j,y_j) = (x_n,y_n)$ for n=1, N. Three other equations are also satisfied,

$$\sum_{n=1}^{N} b_n = \sum_{n=1}^{N} x_n\, b_n = \sum_{n=1}^{N} y_n\, b_n = 0$$

to give the necessary N+3 total equations to solve for the N+3 unknown coefficients. With the known coefficients, the pressures at the doublet lattice points are calculated.

An example of the surface spline fit is shown in figure 5b. The condition is M=0.80, α_w=10.18° (α_{body}=9.18°) and f_{model}=48 Hz. The two span stations shown are η=0.600 and η=0.77. The plotted symbols are the processed values obtained from the wind tunnel data conversion program. The surface spline is the smooth curve which shows a well behaved fit of the data. This comparison is typical of other conditions and serves to illustrate the power of the surface spline to smooth the incredibly ragged data which is being used.

The wing pressure values obtained from interpolation, p_{wB}, are the values used to calculate the tail pressures, p_{tB}, discussed in the previous section. The p_{wB} and p_{tB} are then input to the doublet lattice program for final calculation of the Q_{rB} and $\overline{F}_B$ terms to be used in the response procedure, SB2.

Buffet Response Prediction

With the input data completed for the dynamic response program, the final step in figure 1 is to calculate the buffet response in terms of accelerations, loads, and moments. Predictions are made for both pure symmetric and antisymmetric airplane motions. Since flight test results (refs. 2, 3, 4) indicate that the airplane response is usually asymmetric, even in a "pure" symmetric maneuver, both the symmetric and antisymmetric responses are combined to produce an upper and lower bounds on buffet characteristics. These bounds are given as a function of angle of attack at a particular Mach-altitude-sweep-gross weight configuration. Since airplane buffet is subject to many variables other than those already accounted for (such as pilot characteristics and atmospheric conditions) the concept of a predicted bounds seems to be a very attractive means for treating the high intensity buffet problem.

The upper and lower bounds spectra, ϕ_u and ϕ_L, are based on the following assumptions:

1. The maximum response possible is obtained when both symmetric response spectra, ϕ_S, and antisymmetric spectra, ϕ_A, are in phase and 100% active at all frequencies:

$$\phi_u = \left[\phi_S^{\frac{1}{2}} + \phi_A^{\frac{1}{2}} \right]^2$$

2. The minimum response possible is obtained when (1) ϕ_S and ϕ_A are 100% active and 180° out of phase, (2) ϕ_S is active only, or (3) ϕ_A is active only:

$$\phi_L = \text{Min.} \left(\begin{array}{c} \left[\phi_S^{\frac{1}{2}} - \phi_A^{\frac{1}{2}} \right]^2 \\ \phi_S \\ \phi_A \end{array} \right)$$

The ϕ_u and ϕ_L can also be used to obtain upper and lower bounds on the RMS values of response. Examples of both will be presented in the application of the method.

The above equations for ϕ_u and ϕ_L represent two extremes between which all flight test results should fall. Since 100% excitation is not possible, it would be expected that excursions outside of the bounds would be more frequent for the lower than the upper. Hence, the norm of the flight test data for all cases should be weighted toward the lower bounds. Comparisons between predictions and flight results confirm this hypothesis.

EVOLVMENT OF THE PREDICTION METHOD

Throughout the development of the prediction method, extensive comparisons with flight test data were made in order to determine the importance of various phenomenon. Results of these comparisons were used to guide the development of the final form of the prediction method which was summarized in the previous section. This section presents a summary of the more important effects as observed during the method development.

Effects of Static Aeroelasticity

Shown in figure 6 are the predicted upper and lower bounds RMS values for the wing bending moment and the corresponding characteristic frequencies, N_O. Also shown are the flight test results at the same configuration (given in the figure). The N_O is the frequency centroid of the PSD curve; hence, its use in conjunction with the RMS provides a much better means for comparing integrated quantities. It is also interesting to note the variation of N_O with α in the results to be presented.

Figure 6 illustrates the improvement of agreement with flight test results if the predicted α values are shifted according to the flexible to rigid lift coefficient ratio as determined from figure 4. The plots on the left are shown with the predictions plotted at the rigid values of α from the wind tunnel data. The right hand plots use the flexibilized value of α. In both cases the flight test data are plotted at their actual α values.

All of the predictions to be given in the following paragraphs will be shown as functions of the flexible α values.

Asymmetric Responses

The examination of flight buffet data has clearly shown that in general the airplane responds in an asymmetric manner under high intensity buffet (refs. 2 and 3). The presence of major response in both symmetric and antisymmetric modes led to the formulation of the upper and lower bounds concept as the only reasonable means by which airplane buffet response could be predicted. Thus, such uncontrollable items as pilot characteristics, atmospheric turbulence, airplane mass and geometric asymmetries, and control system inputs could be covered to a large extent.

The upper bound was taken to be the sum of both predicted symmetric and antisymmetric responses acting in phase at all frequencies. Although this may seem conservative, it will be shown that this point can sometimes be exceeded. The lower bound was taken as either the symmetric or antisymmetric responses or the differences between the symmetric and antisymmetric responses, whichever was the lowest value at that corresponding frequency.

An example of an upper and lower bounds PSD plot is shown in figure 7 for the wing tip accelerometer. Comparison is made with both the right and left wing tip results from flight test. It will be noted that even though there is a wide separation between the bounds, there are several points at which the flight test data confirms the difference. At about 12, 21, and 27 Hz, the right and left wing tips indicate such a superpositioning of symmetric and antisymmetric responses. Also, exceedence of the upper bounds from about 15 to 21 Hz was felt to be due to some non-linearities not covered in the prediction method.

Another example of the upper and lower bounds is shown in figure 8 to illustrate variation with α. This prediction is for

the wing bending moment (same condition as in figure 7) where comparison is made with one wing only. These plots are the PSD's for the RMS-N_O results given in figure 6. Comparison of figures 6 and 8 shows how the change in spectral shape toward the first wing bending modes (sym. = 4.8 Hz, anti. = 7.4 Hz) with increasing buffet intensity is reflected by a steady decrease in N_O. The flight test data are well bounded by the predictions.

Effect of Horizontal Tail Loads

During the prediction method development the effect of adding horizontal tail unsteady aerodynamics and buffet loads was studied. Shortcomings of the initial prediction method which used wing aerodynamics only, led to this investigation. However, measured buffet pressure data were not available for the horizontal tail since the model was not instrumented as such. Thus, the semi-empirical scheme which used the doublet lattice aerodynamic matrices as described in the previous section was developed.

The results shown in figure 9 illustrate the effect of varying horizontal tail loads on the wing shear. The wing alone results are obtained with wing buffet pressures and wing unsteady aerodynamics. For this simulation, the lower bounds seem to be more representative of the flight data and the N_O plot does not agree at all. The PSD's for this case verified the disagreement. The second solution with total airplane unsteady aerodynamics and full horizontal tail buffet loads showed a significant improvement, particularly for the N_O comparison as was reflected by the PSD's. It was apparent, however, from examination of the horizontal tail pivot loads, from both flight test and prediction that the tail buffet pressures were too high. Further thought on the matter led to the conclusion that the estimated tail buffet pressures should be divided by two. This conclusion was based on the fact that at high angle of attack, the buffet wake which leaves primarily from the wing upper surface has very little effect on the tail lower surface. In addition, the tail is usually at negative incidence relative to the wing. The final solution with 1/2 horizontal tail buffet loads as shown in figure 9 verifies the reasoning in that the RMS loads are well bounded and the N_O results show excellent agreement. (This solution has another variation included where the wing first torsion frequencies of the airplane and wind tunnel model were matched which reduced the frequency limit of the prediction from 38 to 31 Hz. The frequency matching contribution to the improved agreement was insignificant compared to that due to using 1/2 tail buffet loads.)

Figure 10 shows the effect of the same variation of horizontal tail buffet loads on the wing tip accelerometer predictions. For this response item, the final method does not appear to be any more accurate than the wing alone method. Since the wing tip accelerometer is sensitive to all wing modes and the wing root shear is more affected by the lower wing bending modes this is not surprising. Total airplane motion which is affected by the horizontal tail has a greater influence in the lower wing mode responses, hence it would be expected to significantly affect the wing root loads. Likewise, it would not have as great of an influence on the higher wing modes which are equally important for wing tip motion.

Figure 11 shows the results for the C.G. vertical accelerometer. Although the wing alone results show excellent agreement for $\alpha = 6.9^{\circ}$ and 11.7°, they do not have the decrease in response at $\alpha = 14.1^{\circ}$ as indicated by the flight test data. Also, since it is felt that it is impossible for the airplane to response at 100% as the wing alone results show, the final method seems to be more realistic.

From this study it was concluded that the horizontal tail was important in the prediction of airplane buffet characteristics under conditions well beyond buffet onset. It also appeared that the concept for estimating the tail buffet loads was correct; however, even with the 1/2 factor, the predicted tail loads were high as compared with flight test data.

Effect of Buffet Pressure Spanwise and Chordwise Phasing

The effect of including various combinations of spanwise and chordwise phase angle data in the buffet pressures used to form the forcing function were studied. The variations included use of the span loadings with and without spanwise phase angles as well as chordwise distributions with and without spanwise phase angles. The spanwise loadings were assumed to have a constant chordwise distribution, hence, generalized forces resulting from torsion modes or those with significant twist were not accurate for the variations which made use of these loadings.

Shown in figure 12 are the PSD results for the wing tip accelerometer for the case discussed in the previous paragraphs. Predicted responses are shown for symmetric conditions only. Figures 12a, 12b and 12c correspond to the four variations made

for $\alpha = 6.6^{o}$, 11.1^{o} and 14.4^{o}, respectively. The buffet loading variations noted in the figures are defined as:

- No Phasing - Spanwise loadings without spanwise phase angle data as obtained from the processed wind tunnel buffet data (section normal force data discussed in ref. 1);

- Spanwise Phasing - Spanwise loadings with spanwise phase angle data;

- Chordwise Phasing - Chordwise distributions with chordwise phase angle data and leading edge pressures assumed to be in phase at all span stations; and

- Spanwise and Chordwise Phasing - Chordwise distributions with chordwise phase angle data and spanwise phasing as determined from the spanwise loading data.

The techniques with which the buffet pressure data are used to form the forcing function have been discussed under the paragraph "Conversion of Wind Tunnel Data to Pressure Distributions."

Comparisons with flight test data made in figures 12 are given only for relative purposes since the predictions are made only for symmetric responses. It can be seen in all cases, however, that the inclusion of the elastic degrees of freedom (9 DOF) in the predictions result in consistently improved solutions as compared to those obtained with rigid body translation (1 DOF). Although individual peaks are not directly comparable, the order of magnitude of the predicted flexible PSDs agrees very well with that of the flight test data.

Comparisons of the four variations in figures 12 for the 1 DOF response curves show the direct effect of phase angle variation on the total fluctuating normal force. Since this degree of freedom is vertical translation, the total normal force PSD is directly proportional to the wing tip accelerometer PSD. In all cases the largest total normal force results from the use of no phasing as might be expected. The inclusion of either spanwise or chordwise phasing or both reduces the total normal force in varying degrees. The most notable change is seen in figure 12c where inclusion of chordwise phasing shows little change in the

1 DOF curve but inclusion of spanwise phasing results in a drastic change. In this case, the flow has become separated at the leading edge and the buffet pressures apparently have such large spanwise phase angles that the total normal force becomes nearly zero at 15, 25 and 32 Hz. This canceling effect is noticeable in figure 12b ($\alpha = 11.1^{o}$) to a lesser degree at different frequencies and even less in figure 12a ($\alpha = 6.6^{o}$). As a result it could be concluded that spanwise phase angle is more important for vortex or leading edge separated flows than for conditions at lower angles of attack where the buffeting forces are due primarily to oscillating shocks or shock induced separation.

Effects of the four variations on the flexible airplane responses vary with the value of α and the type of mode shape. The first wing bending mode (4.794 Hz) shows the greatest response for no phasing and least response for both chordwise and spanwise phasing for $\alpha = 6.6^{o}$ and $\alpha = 11.1^{o}$. For $\alpha = 14.4^{o}$, however, the response for spanwise and chordwise phasing is almost as large as no phasing. The first wing torsion mode (24.064 Hz) is most sensitive to chordwise phasing which is well illustrated in figure 12a ($\alpha = 6.6^{o}$). At the higher angles, the effect of phasing is not too dramatic. This is felt to be more due to the nature of the response item since, as will be shown, wing torsion response is sensitive to chordwise phasing at all angles of attack. Finally, a combined wing second bending mode with some twist (37.573 Hz) always shows maximum response for no phasing and minimum for spanwise and chordwise phasing with a range of almost two orders of magnitude for $\alpha = 14.4^{o}$. This mode shows greater sensitivity to spanwise phasing at $\alpha = 11.1^{o}$ and 14.4^{o}, and about the same sensitivity to either chordwise or spanwise at $\alpha = 6.6^{o}$.

Figure 13 shows the effect of phasing on the total RMS and N_o results for various accelerometers and wing loads and moments. Almost all items have the highest response for no phasing at all angles of attack with exception of wing bending moment at $\alpha = 14.4^{o}$. The minimum response varies with angle of attack where chordwise and spanwise phasing is minimum at $\alpha = 11.1^{o}$ and spanwise phasing is minimum at $\alpha = 14.4^{o}$.

The Influence of Wing Torsional Motion

The strong coupling between torsional motion of the airfoil and shock oscillation is one of the important characteristics of transonic Mach buffet. As the airfoil oscillates in low frequency

torsion, the shock on the upper surface moves forward with nose up displacement and aft with nose down. Thus, the lift increment on the airfoil due to shock movement is negative for a positive increment in angle of attack, $\Delta\alpha$. For low values of mean angle of attack, α, the total incremental lift due to $\Delta\alpha$ is positive as a result of increased lift forward of the shock. As α increases, the mean shock position moves forward on the upper surface in an orderly fashion until it nears the crest of the airfoil relative to the freestream direction. As it nears the crest, it moves larger distances for a constant $\Delta\alpha$, and, at the crest, it becomes very unstable and tends to move forward of the crest for a very small $\Delta\alpha$. At this point, the total incremental lift due to the small $\Delta\alpha$ is negative in two-dimensional flow as a result of shock movement. The additional lift upstream of the shock due to the small $\Delta\alpha$ is negligible; hence a "glich" results in the lift-vs.-α curve.

In a dynamic sense, the above mechanism creates a very strong forcing function, which results in significant buffet response at the first wing-torsion-mode frequency. This "torsion mode peak" should occur at $\alpha \approx 10^{\circ}$ for Mach = 0.80 and $\Lambda = 26^{\circ}$ on the rigid F-111A, as indicated by the rigid-body responses in the predicted PSDs. Approximate accounting for static aeroelastic effects increases the value to $\alpha \approx 10.9^{\circ}$ at an altitude of 6035M and to $\alpha \approx 11.5^{\circ}$ at 1490M. The increased twist of the wing due to static aeroelasticity, however, will tend to soften the mechanism by preventing the shock from crossing the crest at all span stations at the same value of α. This effect cannot be accounted for in the linear static aeroelastic correction but is undoubtedly significant. The significance has long been observed as a flattening or complete disappearance of the transonic "glich" on static aeroelastic models.

Shown in figure 14 are comparisons of predicted rigid and elastic responses with flight test results for several variations of the theoretical model. In figure 14a results are shown for a wing-alone prediction with directly scaled wind tunnel model data. These results show how the "torsion mode peak" in the model data at $\alpha \approx 10^{\circ}$ (rigid) did not scale to correspond with the airplane first torsion mode frequency. In reality, this peak was scaled to occur at about 30 Hz as can be observed in figure 14a rather than at about 25 Hz which is the airplane first torsion frequency.

Figure 14b shows how prediction compares with flight test results for a theoretical model which uses total airplane aero-

dynamics and matched model and airplane first torsion frequencies. The total airplane aerodynamics included 100% buffet forces on the horizontal tail. The frequencies were matched by changing the frequency scale factor such that the model first wing torsion mode frequency became 25 Hz. Comparison of figures 14a and 14b shows that although frequency matching resulted in improving the prediction in the vicinity of 25 Hz, the large peak observed in the flight test data was still not predicted.

Figure 14c shows results of the final perturbation where 1/2 of the horizontal tail buffet loads were used. In this case, overall agreement is improved, however, the "torsion mode peak" is further degraded.

This study illustrates the importance of the coupling between the torsional motion and shock movement as a mechanism for producing severe buffeting forces. Since the wind tunnel model was significantly more rigid than the airplane, its torsional motion could not produce a forcing function as strong as that which occurred in the airplane via the coupling mechanism. Also, linear theory unsteady aerodynamics as used which do not consider the presence of shocks in the flow would not produce the shock motion induced loads. Thus, failure to predict the "torsion mode peak" is felt to be a result of not including the torsion-shock coupling mechanism in the theoretical model.

Effect of Maneuver Transients

The buffet prediction method was developed on the assumption that buffet response can be represented by a stationary random process at any point during a maneuver. In actuality, however, the maneuvers in which high intensity buffet are encountered are often highly transient. In such instances, predictions made at the limits of the maneuver should represent an upper and lower bound for measured flight test results. (The bounding of transient response should not be confused with the bounds at a given α due to combined symmetric and antisymmetric response.)

A pullup maneuver performed during Flight 79 for M = 0.8, alt. = 1490M, G.W. = 324,000N and $\Lambda = 26^{\circ}$, (discussed in ref. 4) serves as an excellent example for illustrating the transient case. The time history of angle of attack, load factor, Mach number, and dynamic pressure is shown in figure 15. Flight test data analyses were made at $\alpha = 4.1^{\circ}$, 7.5°, 8.9° and 10.4°. Because of the short

duration of the maneuver, the data samples were only one second long; however, the variation of α within these samples was still quite large as summarized in the table below.

VARIATION OF IN THE FLIGHT 79
DATA ANALYSIS POINTS

α_{NOM}	α_1	α_2	α_{MAX}	$\Delta\alpha$
4.1	2.95	5.50	5.50	2.55
7.5	5.12	10.10	10.10	4.98
8.9	6.20	11.60	11.60	5.40
10.4	9.00	9.60	12.10	3.10

Predictions were made with a wing-alone representation for symmetric modes only at $\alpha = 6.1^{\circ}$ and 10.18° (rigid) which are equivalent to $\alpha = 7.0^{\circ}$ and 11.7° (flexibilized). Comparisons with flight test results are shown in figure 16 for the wing tip accelerometer. In each plot, the bounds are represented by the symmetric predictions for $\alpha = 7.0^{\circ}$ (lower bound) and $\alpha = 11.7^{\circ}$ (upper bound), where static flexibility was accounted for. Flight test results are shown for $\alpha = 7.5^{\circ}$, 8.9° and 10.4° which should all fall within the bounds. Noting the range of variation for the three flight test points in the above table, it is evident that the comparisons of figure 16 verify the concept.

CAPABILITY ASSESSMENT OF THE METHOD

As a test of the final version of the prediction method, results were calculated for a wide variety of flight conditions and compared with flight test data. The comparisons presented in this section are made on the basis of RMS response and characteristic frequencies, N_O. The predictions are given in the form of an upper and lower bounds for all response items except pilot seat and C.G. accelerometers. In addition, the calculated natural mode shapes used in the predictions are given for all cases.

The second volume of this report presents the predicted upper and lower bounds power spectra for all of the cases and response items given in this section. The flight test power spectra are shown on each prediction plot for the nominal value of angle of attack that most closely agrees with the flexible angle for the prediction. The flight test and prediction conditions are given

in both this volume and Volume 2 in tabular form for all cases considered. The order in which the plots are given corresponds to that of the results given in this section.

The conditions used for assessment of the prediction method are summarized as the following cases:

Case 1: Wing alone prediction
$\Lambda = 26^{o}$, M = 0.80, Alt = 6035m

Case 2: Total airplane prediction (half horizontal tail, matched first wing torsion mode frequencies)
$\Lambda = 26^{o}$, M = 0.80, Alt = 6035m

Case 3: Total airplane prediction (final method)
$\Lambda = 26^{o}$, M = 0.70, Alt = 7559m

Case 4: Total airplane prediction (final method)
$\Lambda = 50^{o}$, M = 0.85, Alt = 8383m

Case 5: Total airplane prediction (final method)
$\Lambda = 72.5^{o}$, M = 0.85, Alt = 7285m

Case 6: Wing alone prediction (final method)
$\Lambda = 50^{o}$, M = 1.20, Alt = 9053m

Case 7: Wing alone prediction (final method)
$\Lambda = 72.5^{o}$, M = 1.20, Alt = 9083m

The methods are referred to in each case since not all cases were treated in the same manner. The wing alone predictions were made with no aerodynamic loadings on the horizontal tail or airplane fuselage forward and aft of the wing. In Case 1, the spanwise phase angles were not used whereas they were used for the wing alone predictions in Cases 6 and 7. In Case 2, spanwise phasing was not used, however, total airplane aerodynamics were used. Case 2 was the only prediction to use shifted frequencies in order to match the first wing torsion modes of the full scale airplane and the model. Cases 3, 4 and 5 made use of the complete final prediction method.

Before beginning a detailed discussion of the prediction results to follow, some general remarks are appropriate on the overall characteristics of the RMS-N_o and PSD results. The wing tip accelerometer results usually show the best agreement with

flight test whereas the horizontal tail loads are usually the worst. Since the horizontal tail buffet pressures were estimated from wing loads, this is not surprising. The predicted wing bending moment and shear are also generally in agreement with flight test results. Due to the short moment arm, wing torsion is usually less in agreement with flight test.

An interesting observation can be made on the c.g. and pilot seat accelerometers. Since they are on the centerline, upper and lower bounds cannot be defined for these items as they are for the other response items. Hence, lateral accelerations are due to antisymmetric responses and vertical accelerations are due to symmetric responses. To the contrary, flight test results show that both vertical and lateral accelerometers each respond in both symmetric and antisymmetric modes. This is perhaps the strongest indication of the presence of asymmetric modes that has been observed.

Prediction Results

The case conditions are described in tables and the prediction results and natural modes in figures. A cross-reference for case numbers, descriptive tables, natural mode figures and response figures is given in Table 3.

Case 1.- This case refers to a wing alone analysis of the same maneuver for which a total airplane analysis is performed under Case 2. The conditions were at a wing sweep of 26° and M = 0.80. This particular maneuver, performed during Flight 77, has been the subject of much of the developmental analysis performed in the previous section on the method evolution.

The wing alone analysis made use of the chordwise pressure distributions without spanwise phase angle and hence does not completely represent the final method. The modes were calculated for the total airplane as shown in figures 17 for symmetric motions and figures 18 for antisymmetric motions. The predicted RMS and N_O responses shown in figures 19 indicate reasonable agreement with flight test data for both the wing tip and c.g. accelerometers which is also backed up by the PSD results in Volume II (figures 1). Wing bending moment and shear are over predicted in a totally unrealistic manner. Wing torsion appears to show excellent agreement in figure 19, which is also verified by the PSD results (Volume II, figure 1) with exception of response

near the first torsion mode frequency (about 25 Hz).

Case 2.- For this case, unsteady aerodynamics and estimated buffet loads were added for the horizontal tail in the analysis of the maneuver which was studied in Case 1. In addition, the scaled model first wing torsion frequency was matched with that of the airplane as indicated by the change in the RMS frequency limit from 38 Hz to 31 Hz. As discussed in the previous section under the effect of horizontal tail buffet loads, all predicted accelerometer responses were improved as shown in figures 20. Since the modes used were the same (shown in figures 17 and 18), the improvement is due only to the change in aerodynamic representations. Wing bending moment and shear RMS are well bounded by the total airplane prediction. The excellent agreement with N_O is further emphasized by corresponding agreement for the PSD results (Volume II, figures 2f and 2g). Wing torsion is under predicted even with the upper bounds at the intermediate angle, $\alpha = 11.7^{o}$. This is primarily due to the fact that the methodology cannot predict the torsion mode peak as shown in the PSDs. The horizontal tail loads are over predicted as discussed previously. The PSDs indicate the problem is due to large inertia loads encountered near the horizontal tail modes at about 15, 25 and 30 Hz (Volume II, figures 2i, 2j and 2k). This characteristic is repeated in the following cases where the total airplane is considered.

Case 3.- Whereas Cases 1 and 2 were concerned with a flow condition in which the buffeting forces were dominated by shock induced loadings, this case is concerned with a lower Mach number, M = 0.7, where the forces are caused by a leading edge separated flow. The modes used are shown in figures 21 and 22 and the RMS-N_O results are shown in figures 23. The predictions are obtained with the final method with chordwise and spanwise phasing and total airplane aerodynamics. Shifting of the frequencies to obtain torsion mode frequency matching was not done in this or any of the remaining cases.

The RMS-N_O results tend to follow the peaky characteristics of the flight test data as discussed by Benepe (ref. 2). The trend is further verified by the PSD results (Volume II, figure 3). Good agreement is shown for the accelerometer results except for the pilots seat. The wing loadings are well bounded with exception of one point for wing torsion. The horizontal tail loads are again over predicted with large inertia loads introduced in the first pitch and bending modes as shown by the PSDs. (Volume II,

figures 3i, 3j and 3k).

Case 4.- For this case, the wing sweep was increased to 50° at a higher Mach number of 0.85. This case also made use of the final prediction method as in Case 3 above. The modes are shown in figures 24 and 25.

The RMS-N_o predictions shown in figures 26 are higher relative to flight test results in that the latter tend to fall along the lower bounds. The characteristics seem to be well predicted, however, as shown by the PSDs (Volume II, figures 4) in which the flight test data are well bounded. The horizontal tail loads are again plagued by the large inertia loadings due to horizontal tail modes (Volume II, figures 4i, 4j and 4k).

Case 5.- The wing sweep was further increased to 72.5° with about the same Mach number of 0.85. The final prediction method was used and the modes are shown in figures 27 and 28.

Comparison of results for this case in figures 29 and Case 4 shows a significant drop in response levels for both flight test data and predicted results. The accelerometer characteristics are well predicted as is more evident by the PSD results (Volume II, figure 5). The wing loads are bounded for both RMS and PSD comparisons. The horizontal tail loads are again over predicted where in this case the inertia loads in the PSDs are more pronounced near the pitch mode frequencies (about 30-34 Hz).

Case 6.- For a wing sweep of 50°, the Mach number was increased from M = 0.85 to M = 1.2. The predictions were made with the final method for which wing loads only were used due to restrictions in the unsteady supersonic aerodynamic procedure. The modes used are shown in figures 30 and 31.

The accelerometer and wing loads predictions as shown in figures 32 bound the flight test data very well. Comparison with results in Case 4 for the same sweep at a lower Mach number shows a significant decrease in buffet intensity. The only item which does not agree in either the RMS-N_o or PSD comparisons is the c.g. accelerometer. This is felt to be in part due to not having a total airplane simulation.

Case 7.- For a wing sweep of 72.5°, the Mach number was also increased from M = 0.85 to M = 1.2. Wing alone aerodynamics were used with the final method in the same manner as was done in

Case 6 above. The modes used are also given in figures 27 and 28 (same as for Case 5). An important exception for this case was that the unsteady aerodynamics would not correctly handle a subsonic trailing edge configuration. Hence, the stiffness and damping were over predicted for this case.

The RMS-N_O results in figures 33 show the effect of too much aerodynamic damping. The responses tend to under predict as opposed to previously observed trends. The PSD results (Volume II, figures 7) further emphasize the behavior in that characteristics are not well predicted. The bounding of the flight test data is very poor for $\alpha = 8.4^{\circ}$ and 15.5° when compared with the other predictions for Cases 1-6. Although this case is a failure in comparison with the flight test data, it illustrates the importance of having the correct unsteady aerodynamic representation.

Summary of the Capability Assessment

The preceding results have illustrated the capability of the buffet prediction method to predict buffet response bounds on full scale aircraft in flight. Comparison of Cases 1 and 2 shows the importance of considering the total airplane when predicting the buffet response of an aerodynamically balanced airplane in flight. Case 7 shows the importance of using accurate unsteady aerodynamic forces.

Comparison of Cases 2 and 3 shows the effect of different types of buffeting flow at subsonic speeds and $\Lambda = 26^{\circ}$. In Case 3, the flow at M = 0.7 is primarily of the leading edge separation type for which the response exhibits the peaky characteristic as discussed by Benepe (ref. 2). In Case 2 the flow at M = 0.80 is dominated by shocks on the wing which produces a far more severe buffeting condition. Comparison of these cases shows that Case 2 responses are more than double those of Case 3 as indicated by both predictions and flight test data.

Cases 2, 4 and 5 show the effects of increasing sweep from 26° to 50° to 72.5° at about M = 0.80 - 0.85. Although gross weight and altitude are also changing, the major influence is due to sweep. In these cases, the decrease in buffet intensity with sweep as shown by flight test data, is well predicted with the method.

Case 6 shows the results for $\Lambda = 50^{o}$ and M = 1.2 which were obtained with a wing alone simulation. Comparison with Case 4 for M = 0.85 illustrates primarily the changes which take place due to the Mach number changing from subsonic to supersonic. Again, the decrease in buffet intensity with increased Mach number is well predicted by the method. The supersonic results would be improved, however, if a total airplane simulation were used.

Figure 34 shows a frequency plot of the RMS-N_O flight test data points for the wing tip accelerometer and the wing shear. The data are plotted according to how many points fell between various 10% fractional bands of the upper bounds. For example, 14 points fell between 20% and 30% of the upper bounds for the wing tip accelerometer. Although the sample is small, the results shown in this figure establish the fact that a reasonable relationship does exist between the predictions and flight test. The data points used include all of those obtained for Cases 2-6.

CONCLUSIONS

A method has been presented in this report for predicting the high intensity buffet response characteristics of highly maneuverable airplanes in flight. The method appears to contain the major ingredients responsible for airplane buffet. Since high intensity buffet response of aircraft is highly dependent on type of maneuver, atmospheric conditions, pilot characteristics and other items, it was felt that a peak-by-peak discussion of each power spectrum was not warranted. What is more important is that the upper bound which represents the maximum possible response is rarely exceeded except in special cases or for certain items. Likewise, the lower bound which is the minimum possible response level rarely falls above flight test data. These were the desired results.

Predictions were presented in the form of an upper and lower bounds which were verified by extensive comparison with flight test data. The changing spectral characteristics of flight test data were shown to be predictable with the method. Static aeroelastic effects were shown to have a significant impact on the predictions. The horizontal tail loads were found to have a significant influence on wing and fuselage responses, hence, the total airplane should be considered. The means for estimating the tail buffet loads from wing data seems to be correct in concept.

In constructing the buffet forcing function, it was shown that the chordwise and spanwise phasing in the pressure data was important. The influence of wing torsional motion in the existing prediction model was found to be insignificant. This was felt to be due to not being able to consider normal shock motions in the development of the unsteady aerodynamic forces due to structural response. It was also shown that maneuver transient effects could be quite pronounced but that the response could be bounded by considering the extremities of the angle of attack range achieved during the maneuver.

Although the prediction of buffet response as described in this report is a formidable task, it is felt that the mechanics of high intensity buffet are much better understood as a result of the study. Since the buffet forcing function was the most difficult input data to obtain, the next step would be to develop a means for calculating this data through a theoretical approach. The fact that linear theory can be used to estimate the horizontal tail loads due to buffeting is strong evidence that such a development is possible.

REFERENCES

1. Riddle, D. W.: Wind Tunnel Investigation of Surface Pressure Fluctuations Associated with Aircraft Buffet. AIAA Paper No. 75-67, January 1975.

2. Benepe, D. B.; Cunningham, A. M., Jr.; and Dunmyer, W. D.: A Detailed Investigation of Flight Buffeting Response at Subsonic and Transonic Speeds. AIAA Paper No. 74-358, April 1974.

3. Benepe, D. B.; Cunningham, A. M., Jr.; Traylor, S., Jr.; and Dunmyer, W. D.: Update on an Investigation of Flight Buffeting of a Variable Sweep Aircraft. AIAA Paper No. 75-68, January 1975.

4. Benepe, D. B., et al.: An Investigation of Wing Buffeting Response at Subsonic and Transonic Speeds; Phase I F-111A Flight Data Analysis; Vol. I - Summary of Technical Approach, Results and Conclusions, NASA CR-152109; Phase II F-111A Flight Data Analysis, Vol. I - Summary of Technical Approach, Results and Conclusions, NASA CR-152112, April 1978.

5. Mullans, R. E.; and Lemley, C. E.: Buffet Dynamic Loads During Transonic Maneuvers. Air Force Flight Dynamic Laboratory Technical Report AFFDL-TR-72-46, September 1972.

6. Allen, M. G.: Structures Analysis Digital Procedure C28 (now Digital Procedure BY7). Report No. ERR-FW-751-1, Fort Worth Division of General Dynamics, September 1968.

7. Watts, D.; and Allen, M. G.: FB-111 Natural Modes and Frequencies as Calculated in C28. (Confidential) MRL-37, Fort Worth Division of General Dynamics, September 1967.

8. Harder, R. L.; and Desmarias, R. N.: Interpolation Using Surface Splines. Journal of Aircraft, vol. 9, no. 2, February 1972, pp. 189-191.

9. Albano, E.; Perkinson, F.; and Rodden, W. P.: Subsonic Lifting Surface Theory Aerodynamics and Flutter Analysis of Interfering Wing/Horizontal-Tail Configurations. Air Force Flight Dynamics Laboratory Technical Report AFFDL-TR-70-59, September 1970.

10. Pines, S.; and Dugundji, J.: Application of Aerodynamic Flutter Derivatives to Flexible Wings with Supersonic and Subsonic Edges. Republic Aviation Report E-SAF-2, April 1954.

11. Cunningham, A. M., Jr: Accurate Approximation of Generalized Aerodynamic Forces as Explicit Functions of Frequency. MRL-200, Fort Worth Division of General Dynamics, December 1973.

12. Woods, D. J.: Program to Compute Response to Random or Discrete Excitation. Report No. ERR-FW-921, Fort Worth Division of General Dynamics, November 1969.

TABLE 1.- BY7 ANALYSIS/TEST COMPARISON OF F-111A SYMMETRIC VIBRATION FREQUENCIES, $\Lambda = 26.0^{o}$

GW=201,000 N =45,180 lb			GW=211,500 N =47,500 lb		
Analysis Results			Test Results (A/P #12)		
Order #	Freq.	Mode	Order #	Freq.	Mode
1	5.17	1st Wing Bend	1	5.2	1st Wing Bend
			2	7.9	Longitudinal Wing Bending
2	8.74	1st Fuse Bend	3	8.6	1st Fuse Bend
3	15.08	H. Tail Bend	4	13.6	H. Tail Bend
4	16.12	2nd Wing Bend	5	16.9	2nd Wing Bend
5	20.98	2nd Fuse Bend			
6	25.48	Wing Torsion	6	25.2	Wing Torsion
7	28.45				
8	31.48				
9	33.37	H. Tail Torsion	7	34.4	H. Tail Torsion
10	35.64				

TABLE 2.- BY7 ANALYSIS/TEST COMPARISON OF F-111A ANTISYMMETRIC VIBRATION FREQUENCIES, $\Lambda = 26.0^{o}$

GW=201,000 N =45,180 lb			GW=211,500 N =47,500 lb		
Analysis Results			Test Results (A/P #12)		
Order #	Freq.	Mode	Order #	Freq.	Mode
1	7.56	1st Wing Bend	1	7.6	1st Wing Bend
			2	9.3	Longitudinal Wing Bending
2	9.93	Lat Fuse Bend	3	9.9	Lat Fuse Bend
3	11.54	V. Fin Bend		11.7	This mode omitted (Freq given is for different GW)
4	12.52	H. Tail Bend (with V. Fin Interaction)	4	13.3	H. Tail Bend
			5	16.2	
5	18.61	2nd Wing Bend	6	17.5	2nd Wing Bend
6	20.79	2nd Lat Fuse Bend			
7	23.25				
8	24.68	Wing Torsion	8	25.4	Wing Torsion
9	25.41	Rudder	7	23.6	Rudder
10	25.92	V. Fin Torsion	9	28.0	V. Fin Torsion
11	28.26	Tail Interaction plus 2nd Wing Bend	10	29.2	V. Fin Torsion plus 2nd Wing Bend
12	31.68	H. Tail Torsion plus V. Fin Torsion	11	31.0	H. Tail Torsion plus V. Fin Torsion
			12	32.7	

TABLE 2.- Continued

GW=201,000 N =45,180 lb			GW=211,500 N =47,500 lb		
Analysis Results			Test Results (A/P #12)		
Order #	Freq.	Mode	Order #	Freq.	Mode
13	32.79	3rd Lat Fuse Bend			
14	37.09	H. Tail Torsion	13	37.3	H. Tail Torsion
15	39.02	Higher H. Tail Mode			
			14	43.8	Rudder Bending and Torsion
			15	45.0	Rudder Bending and Torsion

TABLE 3.- CROSS REFERENCE FOR CASE NUMBERS AND TABLES AND FIGURES

CASE	DESCRIPTIVE TABLE	NATURAL MODE FIGURES	RESPONSE FIGURE
1	4	17(sym), 18(anti)	19
2	5	17(sym), 18(anti)	20
3	6	21(sym), 22(anti)	23
4	7	24(sym), 25(anti)	26
5	8	27(sym), 28(anti)	29
6	9	30(sym), 31(anti)	32
7	10	27(sym), 28(anti)	33

TABLE 4.- CASE 1, WING ALONE, $\Lambda = 26^{\circ}$, M = 0.80, ALT = 6035m (19,800 ft)

CASE 1 **FLIGHT 77** **RUN SC-R**

	FLIGHT TEST CONDITIONS	PREDICTION CONDITIONS
Wing Sweep	25.6°	26°
Mach	0.80 - 0.78	0.80
Altitude	6035m (19,800 ft)	6035m (19,800 ft)
Gross Weight	266,004N (59,800 lb)	266,004N (59,800 lb)

POINTS ANALYSED						
ΔT	α_1	α_2	α_{MAX}	α_{NOM}	α^{*}_{FLEX}	α_{RIG}
2	4.22°	5.98°	-	5.1°	-	-
2	6.80°	7.12°	-	6.9°	6.6°	6.1°
2	8.15°	9.35°	-	8.9°	-	-
2	10.35°	12.90°	-	11.7°	11.1°	10.18°
2	12.70°	14.65°	14.95°	14.1°	14.4°	13.26°
3	11.05°	14.95°	14.95°	13.0°	-	-

$^{*}\frac{C_{L\alpha_{FLEX}}}{C_{L\alpha_{RIG}}} = \frac{\alpha_{RIG}}{\alpha_{FLEX}} = 0.920$ as obtained from Figure 4

TABLE 5.- CASE 2, TOTAL AIRPLANE (HALF HORIZONTAL TAIL), $\Lambda = 26^{o}$, M = 0.80, ALT = 6035m (19,800 ft)

CASE 2 **FLIGHT 77** **RUN SC-R**

	FLIGHT TEST CONDITIONS	PREDICTION CONDITIONS
Wing Sweep	25.6^{o}	26^{o}
Mach	0.80 - 0.78	0.80
Altitude	6035m (19,800 ft)	6035m (19,800 ft)
Gross Weight	266,004N (59,800 lb)	266,044N (59,800 lb)

POINTS ANALYSED

ΔT	α_1	α_2	α_{MAX}	α_{NOM}	α^{*}_{FLEX}	α_{RIG}
2	4.22^{o}	5.98^{o}	-	5.1^{o}	-	-
2	6.80^{o}	7.12^{o}	-	6.9^{o}	6.6^{o}	6.1^{o}
2	8.15^{o}	9.35^{o}	-	8.9^{o}	-	-
2	10.35^{o}	12.90^{o}	-	11.7^{o}	11.1^{o}	10.18^{o}
2	12.70^{o}	14.65^{o}	14.95^{o}	14.1^{o}	14.4^{o}	13.26^{o}
3	11.05^{o}	14.95^{o}	14.95^{o}	13.0^{o}	-	-

$^{*}\frac{C_{L\alpha_{FLEX}}}{C_{L\alpha_{RIG}}} = \frac{\alpha_{RIG}}{\alpha_{FLEX}} = 0.920$ as obtained from Figure 4

TABLE 6.- CASE 3, TOTAL AIRPLANE (FINAL METHOD), $\Lambda = 26^{o}$, M = 0.70, ALT = 7559m (24,800 ft)

CASE 3 **FLIGHT 48** **RUN 6**

	FLIGHT TEST CONDITIONS	PREDICTION CONDITIONS
Wing Sweep	26.6^{o}	26^{o}
Mach	0.70 - 0.68	0.70
Altitude	7559m (24,800 ft)	7559m (24,800 ft)
Gross Weight	294,472N (66,200 lb)	293,138N (65,900 lb)

POINTS ANALYSED

ΔT	α_1	α_2	α_{MAX}	α_{NOM}	α^{*}_{FLEX}	α_{RIG}
1	8.72^{o}	9.55^{o}	-	8.8^{o}	9.6^{o}	9.2^{o}
1	9.70^{o}	10.75^{o}	-	9.8^{o}	10.7^{o}	10.2^{o}
1	10.30^{o}	11.75^{o}	-	10.7^{o}	11.8^{o}	11.2^{o}
1	11.15^{o}	13.55^{o}	-	11.8^{o}	12.8^{o}	12.2^{o}
1	14.25^{o}	16.60^{o}	-	14.6^{o}	17.1^{o}	16.3^{o}

$^{*}\frac{C_{L\alpha_{FLEX}}}{C_{L\alpha_{RIG}}} = \frac{\alpha_{RIG}}{\alpha_{FLEX}} = 0.950$ as obtained from Figure 4

TABLE 7.- CASE 4, TOTAL AIRPLANE (FINAL METHOD), $\Lambda = 50^{\circ}$, M = 0.85, ALT = 8382m (27,500 ft)

CASE 4 FLIGHT 61 RUN R227

	FLIGHT TEST CONDITIONS	PREDICTION CONDITIONS
Wing Sweep	49.1°	50°
Mach	0.82 - 0.79	0.85
Altitude	8382m (27,500 ft)	8382m (27,500 ft)
Gross Weight	330,948N (74,400 lb)	331,392N (74,515 lb)

POINTS ANALYSED						
ΔT	α_1	α_2	α_{MAX}	α_{NOM}	α^{*}_{FLEX}	α_{RIG}
1	7.10°	9.25°	-	7.9°	-	-
1	8.05°	10.10°	-	8.9°	8.9°	8.1°
1	10.10°	10.80°	-	10.0°	-	-
1	10.60°	12.70°	-	11.1°	11.1°	10.2°
1	12.90°	14.60°	14.60°	13.1°	14.4°	13.2°

* $\frac{C_{L\alpha_{FLEX}}}{C_{L\alpha_{RIG}}} = \frac{\alpha_{RIG}}{\alpha_{FLEX}} = 0.920$ as obtained from Figure 4

TABLE 8.- CASE 5, TOTAL AIRPLANE (FINAL METHOD), $\Lambda = 72.5^{\circ}$, M = 0.85, ALT = 7285m (23,900 ft)

CASE 5 FLIGHT 48 RUN 7-R

	FLIGHT TEST CONDITIONS	PREDICTION CONDITIONS
Wing Sweep	72.2°	72.5°
Mach	0.89 - 0.84	0.85
Altitude	7559m (24,800 ft)	7285m (23,900 ft)
Gross Weight	265,559N (59,700 lb)	268,673N (60,500 lb)

POINTS ANALYSED						
ΔT	α_1	α_2	α_{MAX}	α_{NOM}	α^{*}_{FLEX}	α_{RIG}
1	7.15°	8.65°	-	7.8°	7.8°	7.1°
1	8.65°	10.00°	-	9.4°	-	-
1	10.75°	12.20°	-	11.1°	11.1°	10.2°
1	14.15°	16.15°	-	14.4°	14.4°	13.3°
1	17.90°	18.90°	19.35°	17.7°	-	-

* $\frac{C_{L\alpha_{FLEX}}}{C_{L\alpha_{RIG}}} = \frac{\alpha_{RIG}}{\alpha_{FLEX}} = 0.890$ as obtained from Figure 4

TABLE 9.- CASE 6, WING ALONE (FINAL METHOD), $\Lambda = 50^{\circ}$, M = 1.20, ALT = 9053m (29,700 ft)

CASE 6 FLIGHT 48 RUN 4

	FLIGHT TEST CONDITIONS	PREDICTION CONDITIONS
Wing Sweep	49.8°	50°
Mach	1.20 - 1.15	1.20
Altitude	9053m (29,700 ft)	9053m (29,700 ft)
Gross Weight	261,111N (58,700 lb)	261,778N (58,900 lb)

POINTS ANALYSED						
ΔT	α_1	α_2	α_{MAX}	α_{NOM}	α^{*}_{FLEX}	α_{RIG}
1	4.70°	5.50°	-	4.9°	-	-
1	8.20°	9.80°	-	8.6°	-	-
1	12.10°	13.70°	-	12.4°	12.4°	10.2°
1	13.70°	13.90°	15.0°	13.7	16.1°	13.2°

* $\frac{C_{L\alpha_{FLEX}}}{C_{L\alpha_{RIG}}} = \frac{\alpha_{RIG}}{\alpha_{FLEX}} = 0.823$ as obtained from Figure 4

TABLE 10.- CASE 7, WING ALONE (FINAL METHOD), $\Lambda = 72.5^{\circ}$, M = 1.20, ALT = 9083m (29,800 ft)

CASE 7 FLIGHT 48 RUN 5

	FLIGHT TEST CONDITIONS	PREDICTION CONDITIONS
Wing Sweep	72.2°	72.5°
Mach	1.20 - 1.16	1.20
Altitude	9083m (29,800 ft)	9083m (29,800 ft)
Gross Weight	274,455N (61,700 lb)	268,673N (60,500 lb)

POINTS ANALYSED						
ΔT	α_1	α_2	α_{MAX}	α_{NOM}	α^{*}_{FLEX}	α_{RIG}
1	4.80°	4.80°	-	4.8°	-	-
1	8.00°	8.80°	-	8.1°	8.1°	7.1°
1	11.30°	12.70°	-	11.6°	11.6°	10.2°
1	14.95°	16.75°	-	15.1°	15.1°	13.4°

* $\frac{C_{L\alpha_{FLEX}}}{C_{L\alpha_{RIG}}} = \frac{\alpha_{RIG}}{\alpha_{FLEX}} = 0.837$ as obtained from Figure 4

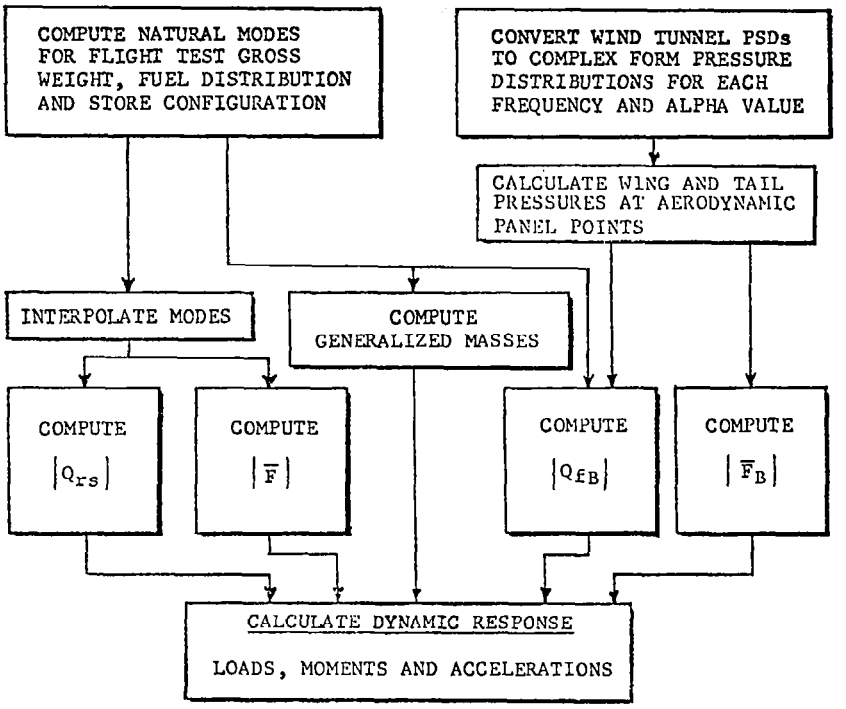

Figure 1.- Buffet prediction method flow diagram

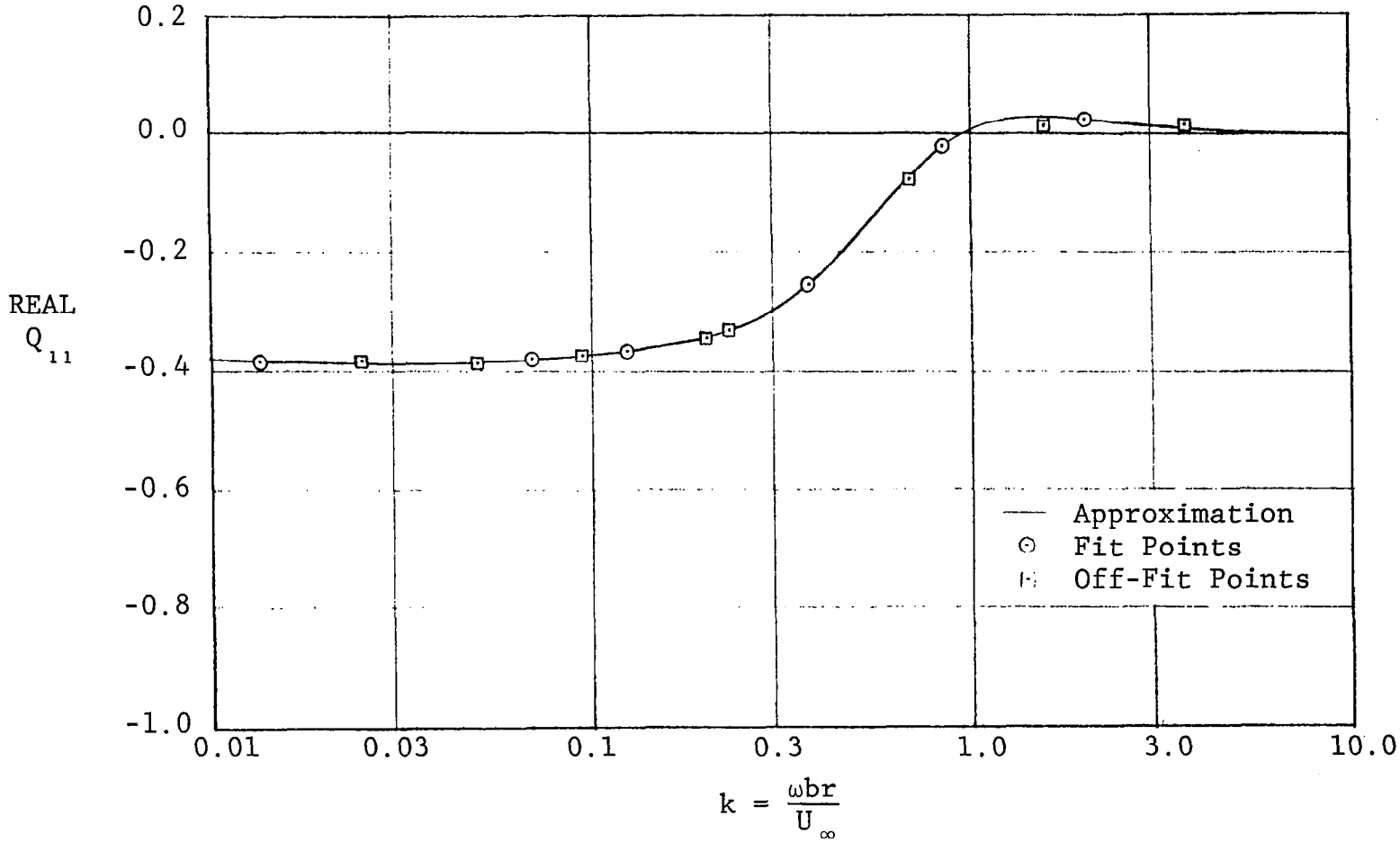

Figure 2.- Approximation for real part of Q_{11} term for wing translation - comparison with calculated values

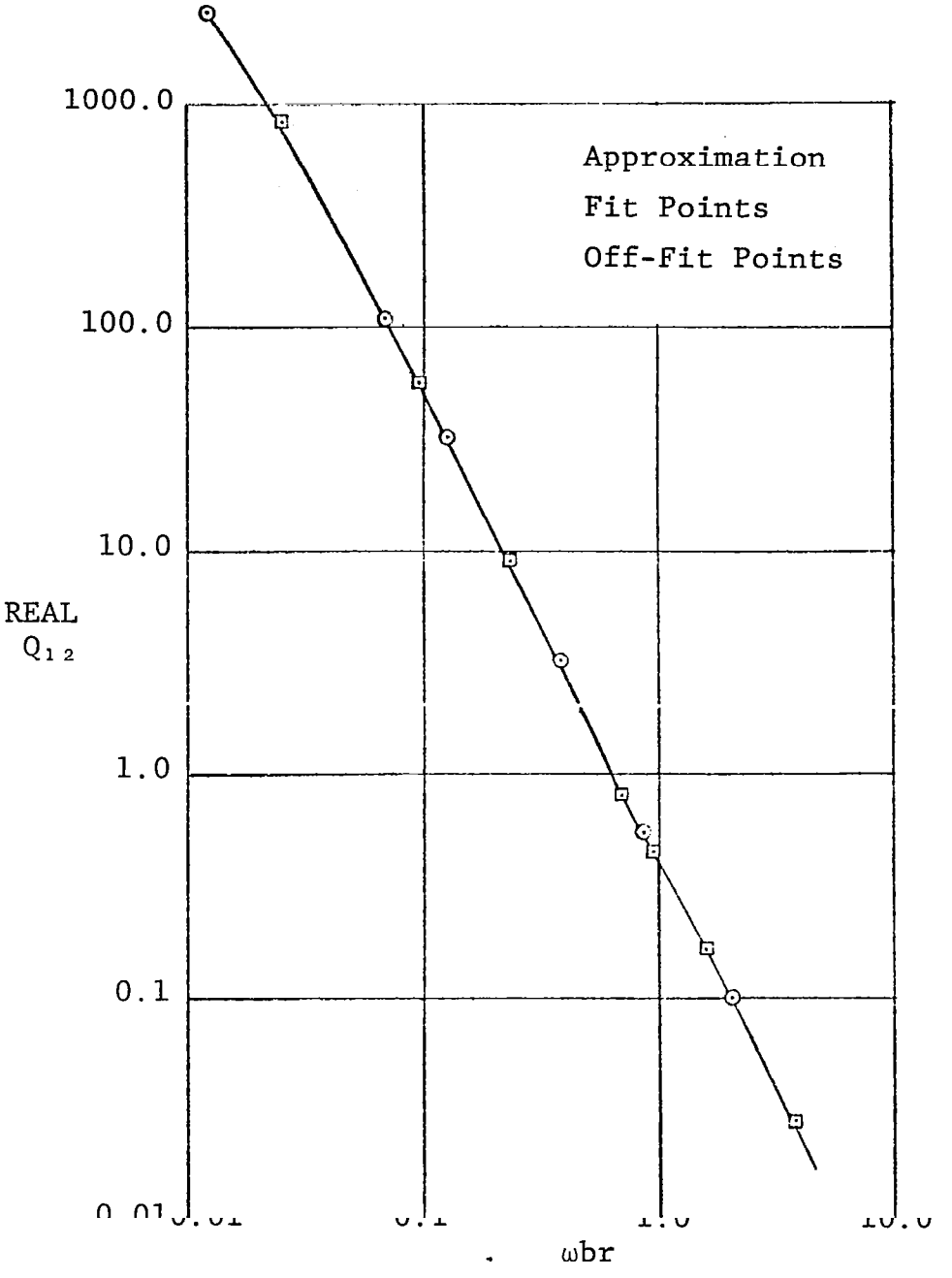
1000.0
100.0
10.0
1.0
0.1
REAL
Q_{12}
Approximation
Fit Points
Off-Fit Points
ωbr

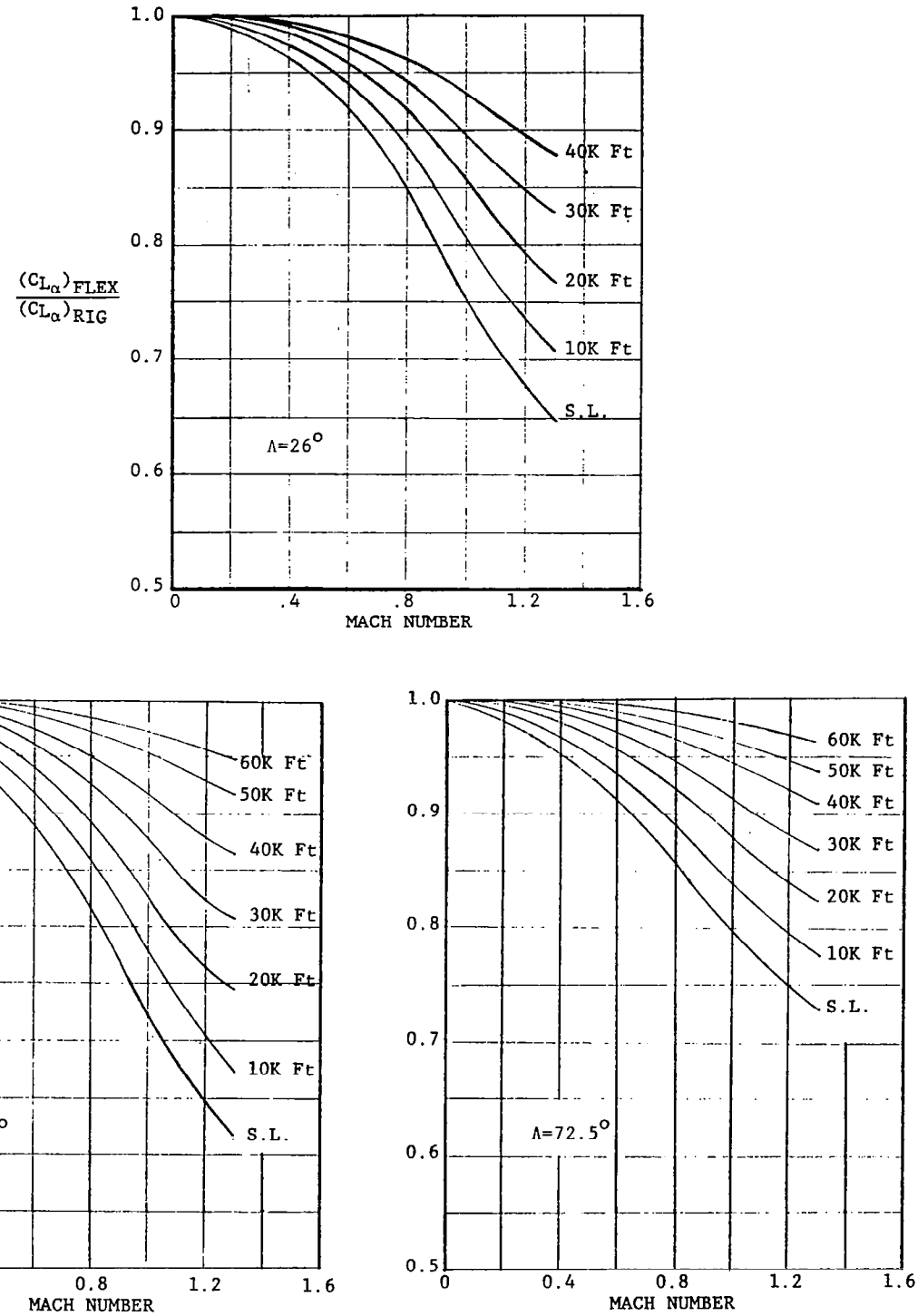

Figure 4.- Effect of wing flexibility on the lift curve slope for the F-111A

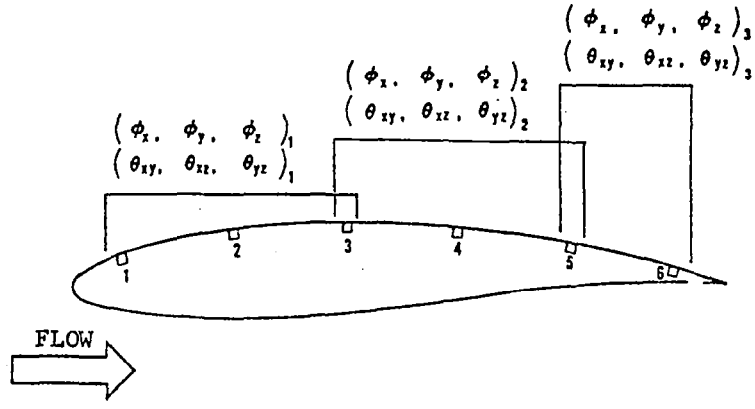

(a) Relationship between the NASA ARC spectral density analysis and the pressure transducer locations

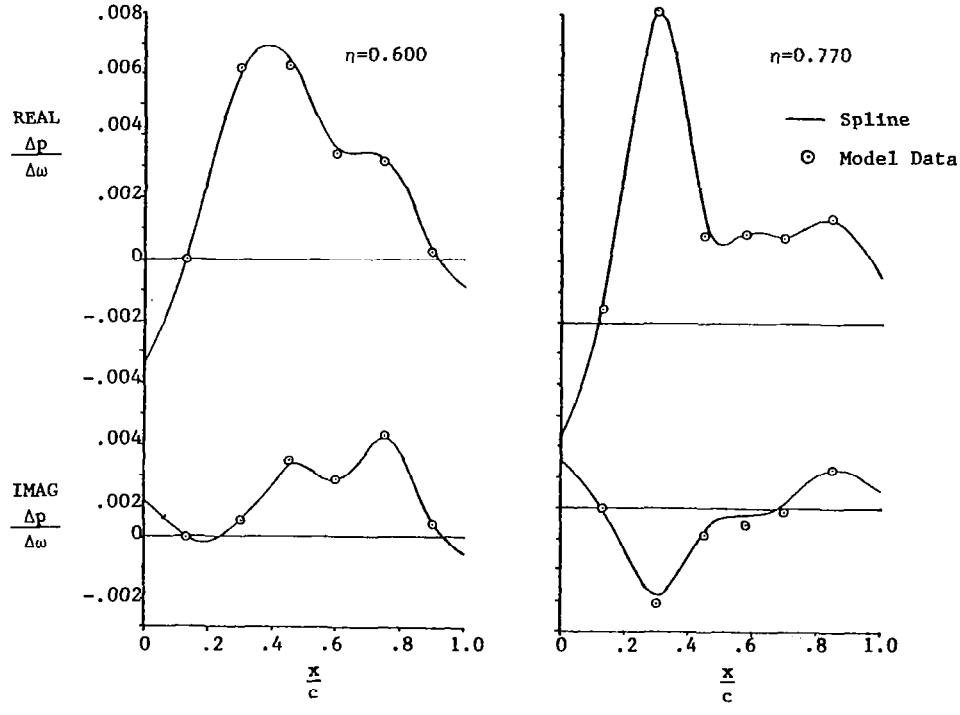

(b) Spline fit of model pressures for M=0.80, α=10.18° and f_{model}=48.0 Hz

Figure 5.- Conversion of wind tunnel PSD's into complex pressure distributions

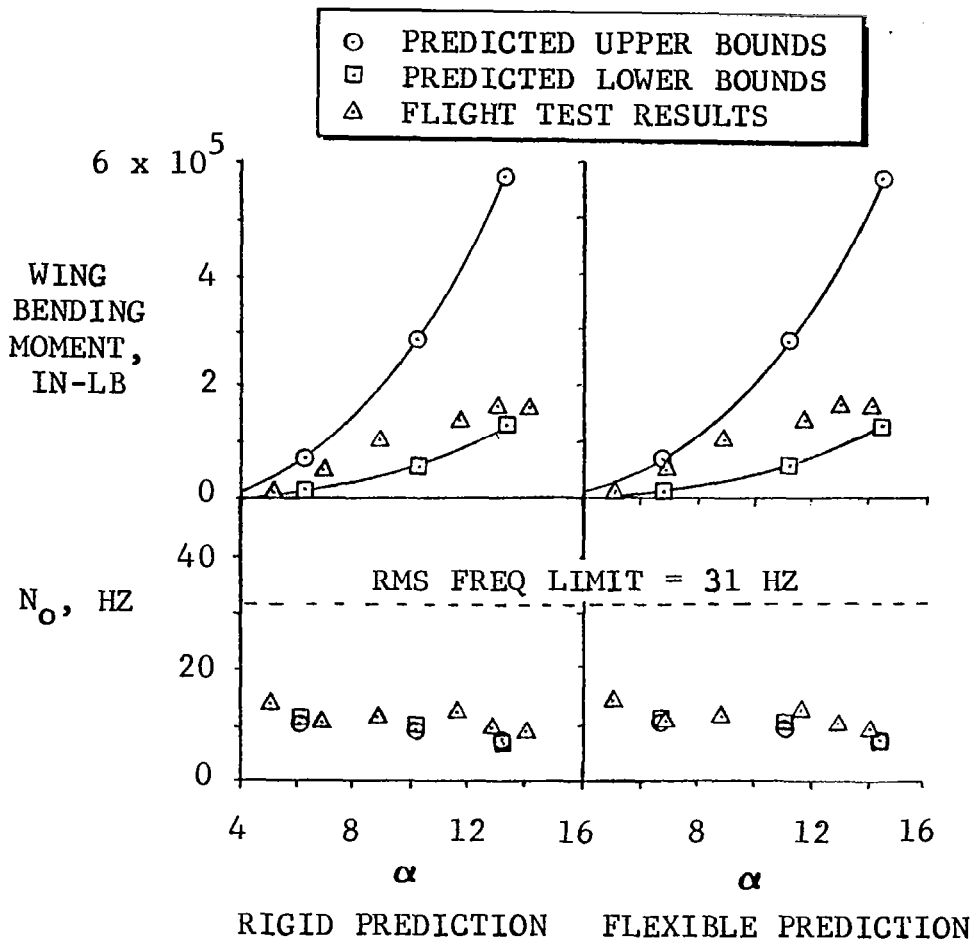

Figure 6.- Rigid and flexible wing bending for $\Lambda = 26^{o}$, M = 0.8, alt = 6035m

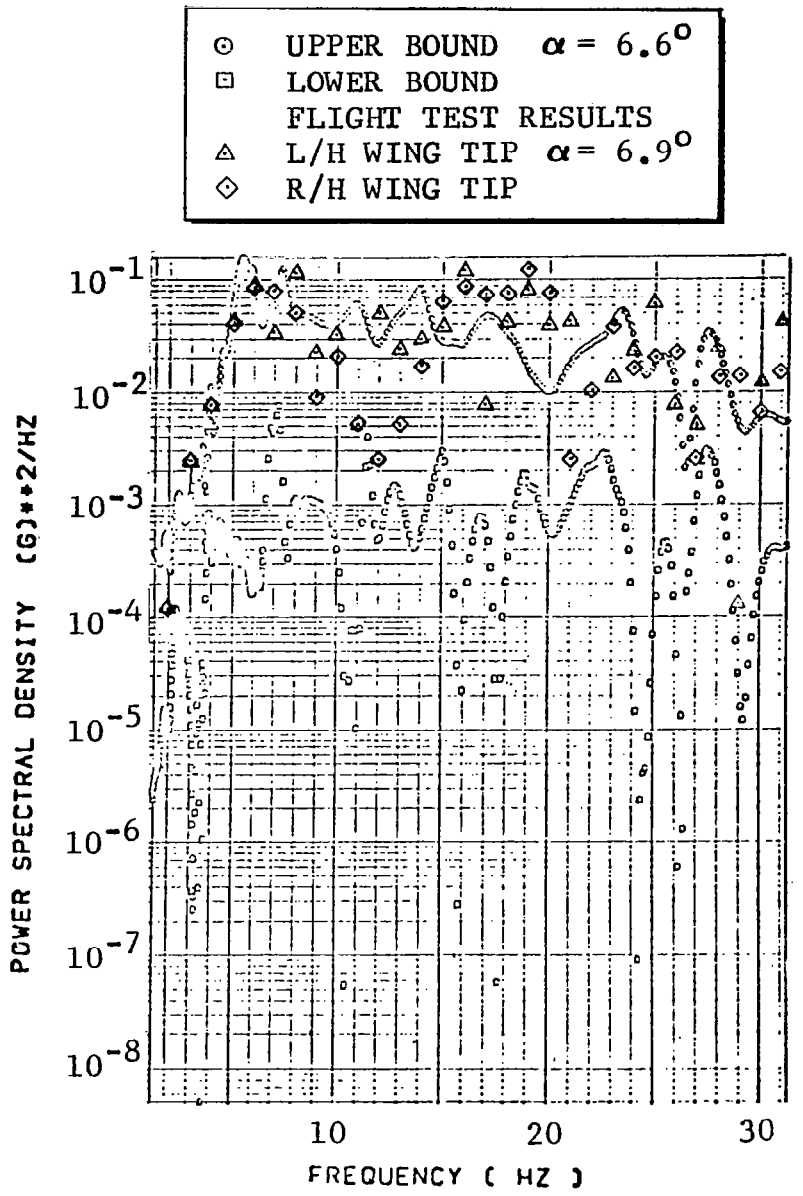

Figure 7.- Predicted bounds on wing tip accelerometer PSD for $\Lambda = 26^{\circ}$, M = 0.8, alt = 6035m

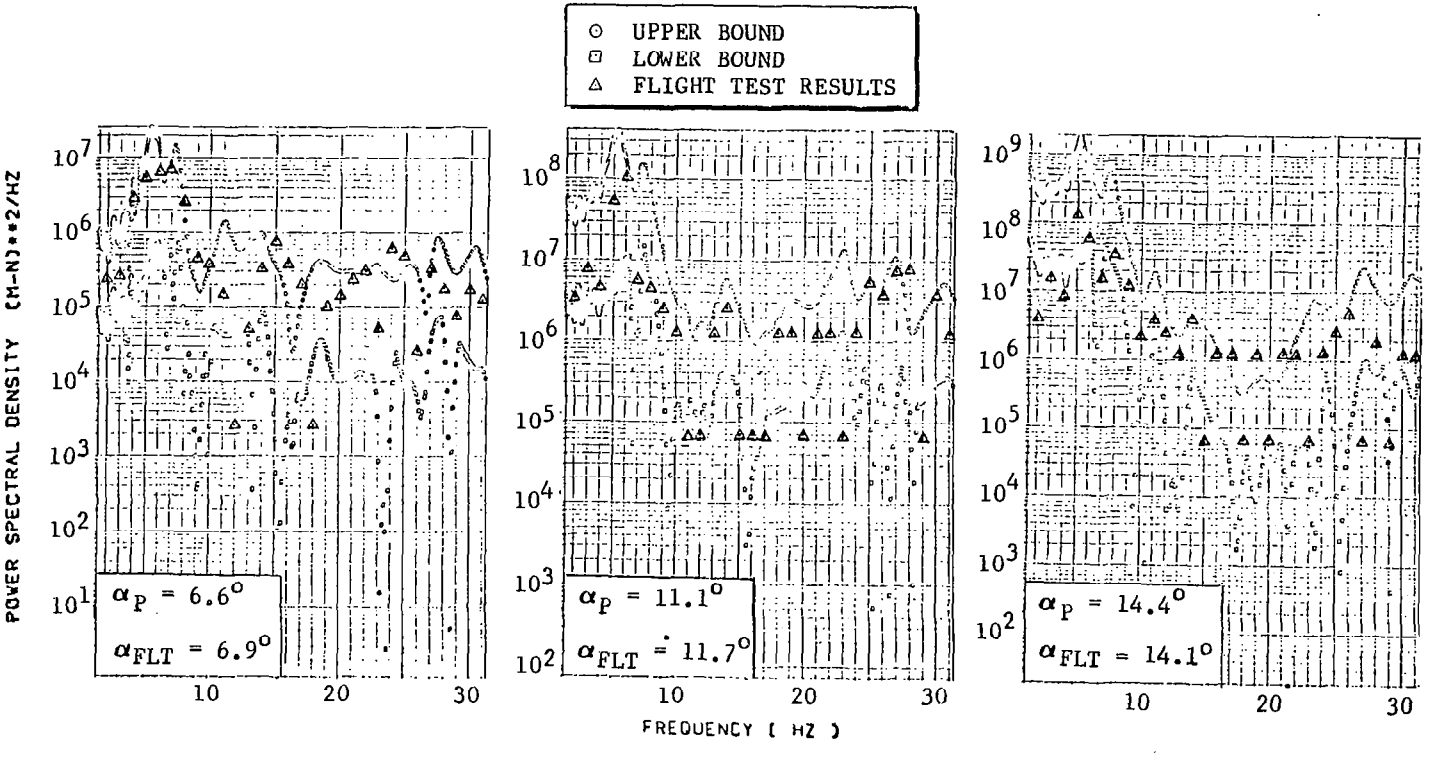

Figure 8.- Predicted bounds on wing bending PSD for $\Lambda = 26^{o}$, M = 0.8, alt = 6035m

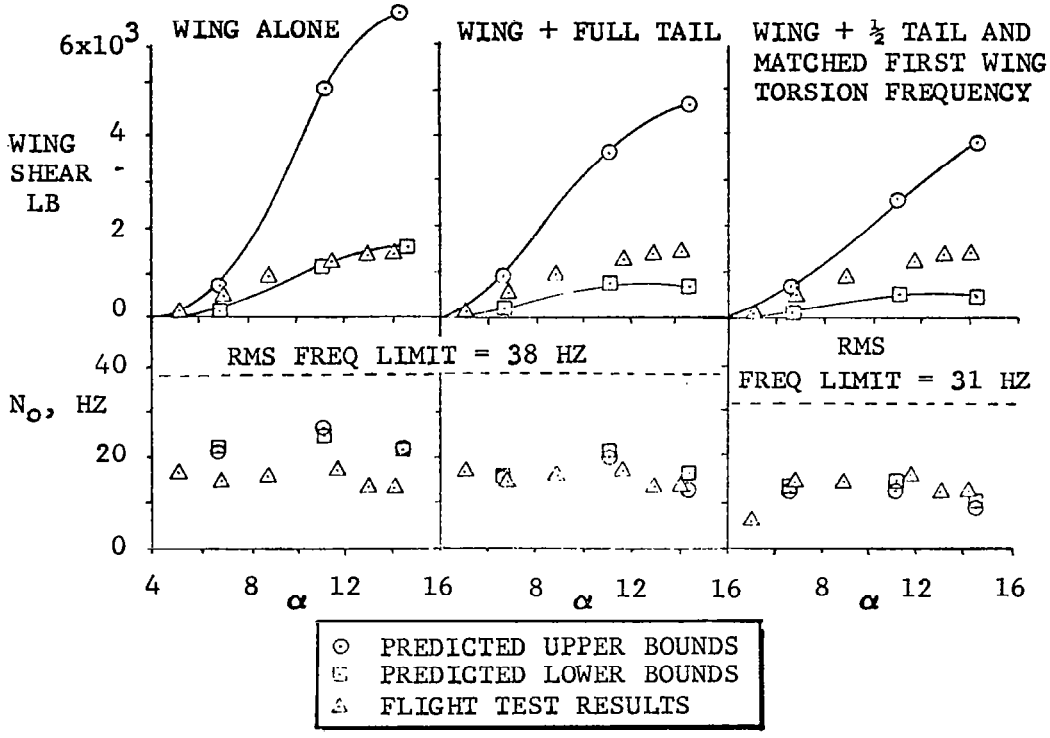

Figure 9.- Effect of horizontal tail loads on wing shear for $\Lambda = 26^{o}$, M = 0.8, alt = 6035m

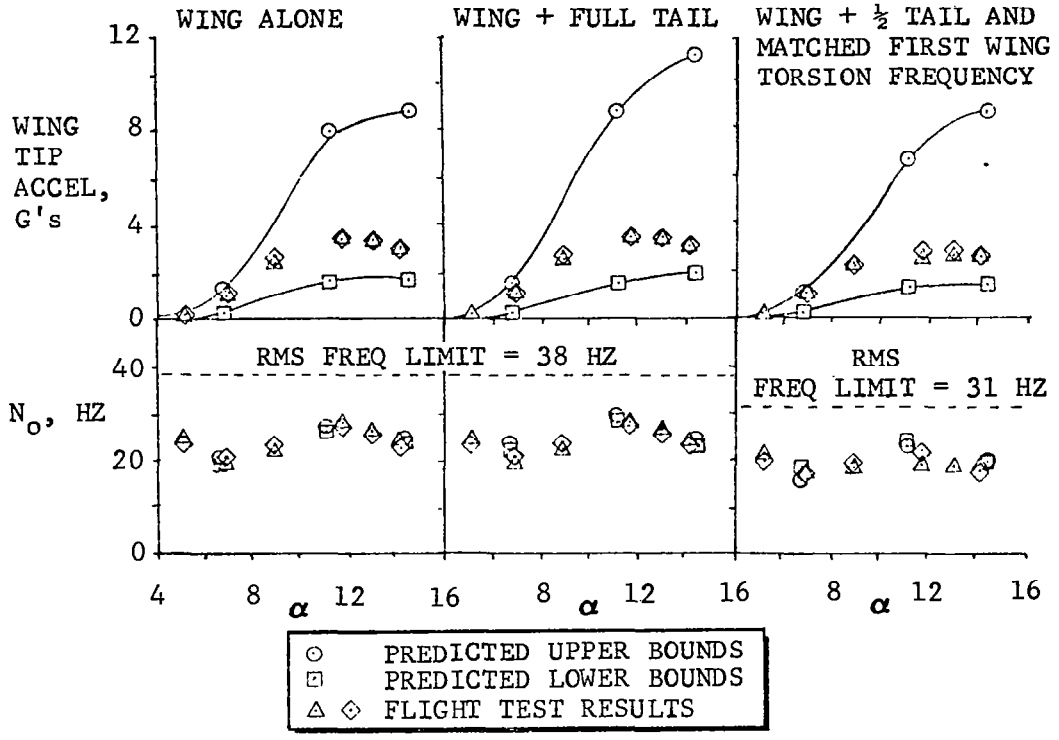

Figure 10.- Effect of horizontal tail loads on wing tip accelerometer for $\Lambda = 26^{o}$, M = 0.8, alt = 6035m

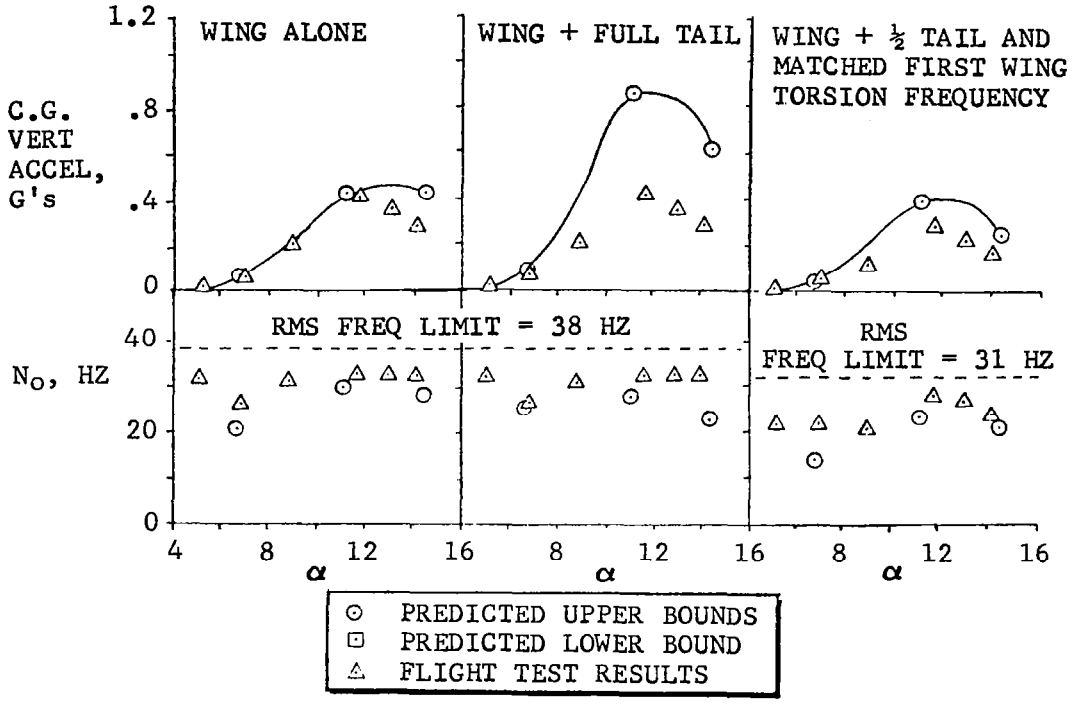

Figure 11.- Effect of horizontal tail loads on c.g. accelerometer for $\Lambda = 26^{\circ}$, M = 0.8, alt = 6035m

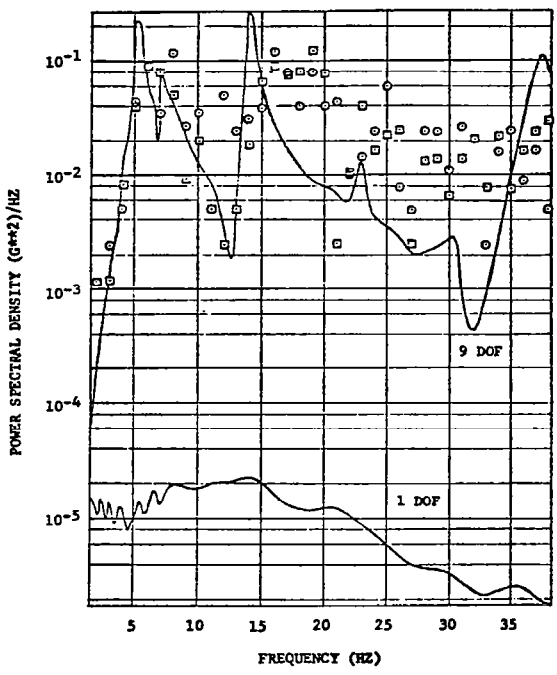

NO PHASING

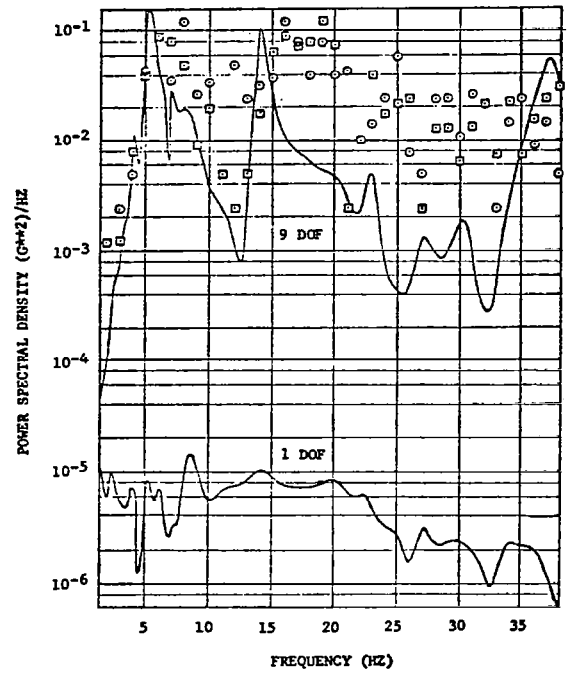

SPANWISE PHASING

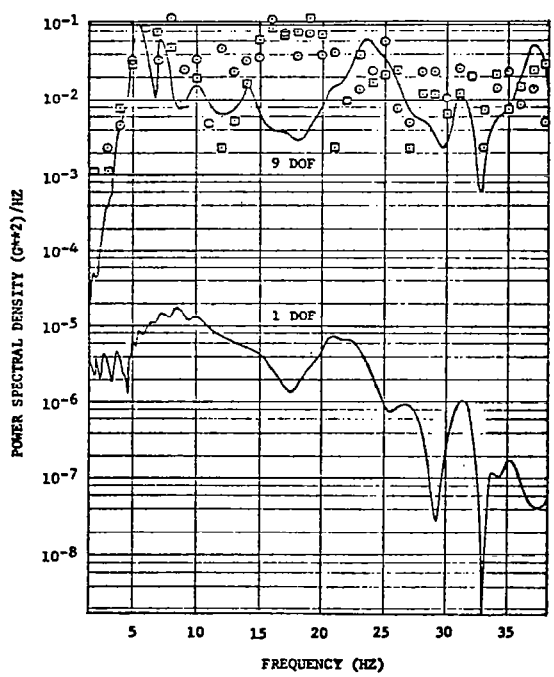

CHORDWISE PHASING

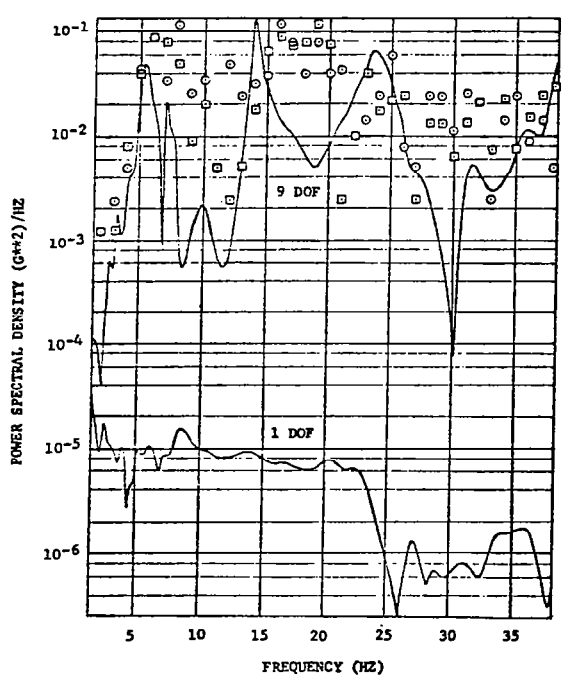

SPANWISE AND CHORDWISE PHASING

Figure 12.- Effect of buffet pressure spanwise and chordwise phasing on wing alone response PSDs for $\Lambda = 26^{o}$, M = 0.8, alt = 6035m
(a) $\alpha = 6.6^{o}$

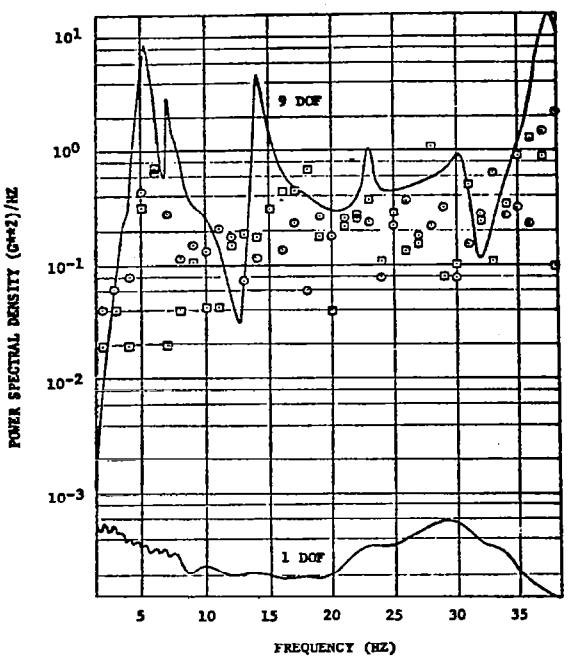

NO PHASING

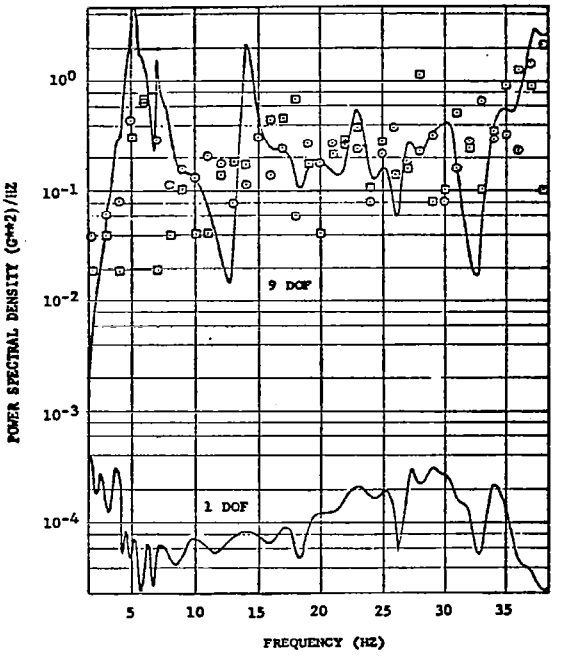

SPANWISE PHASING

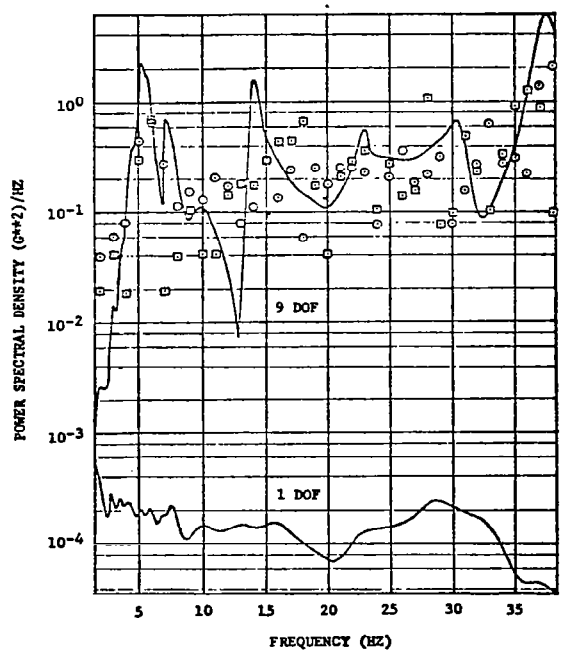

CHORDWISE PHASING

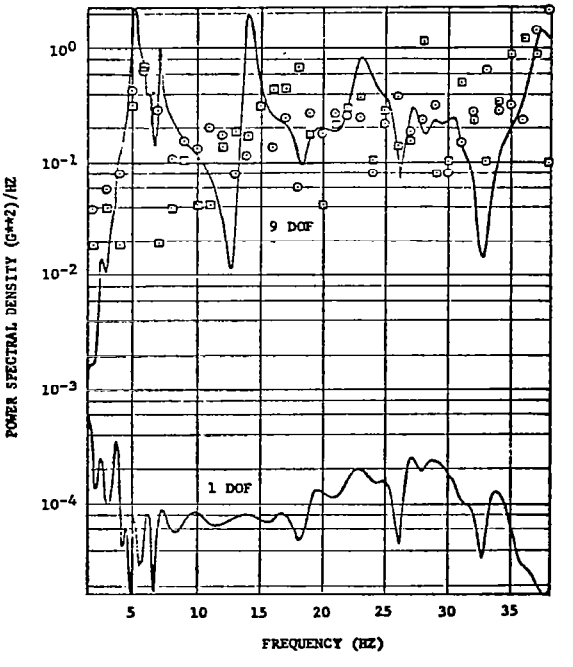

SPANWISE AND CHORDWISE PHASING

Figure 12.- (b) $\alpha = 11.1^{o}$

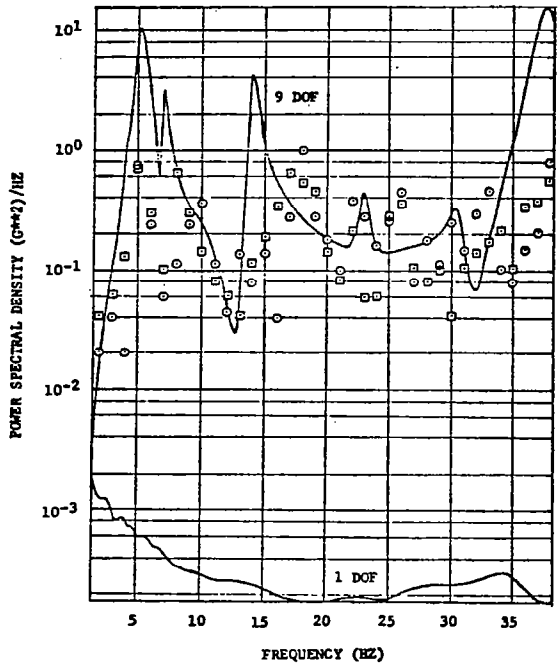

NO PHASING

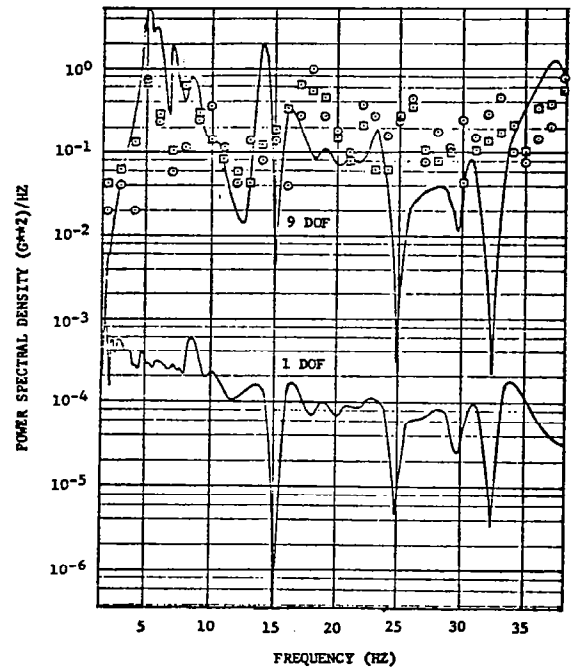

SPANWISE PHASING

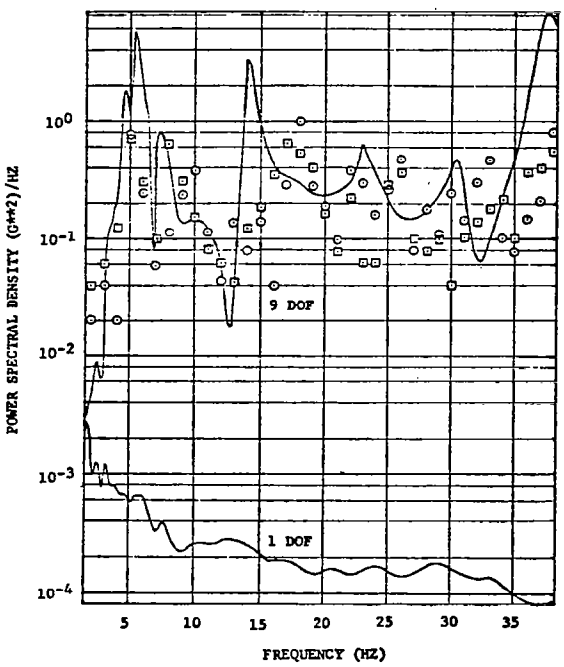

CHORDWISE PHASING

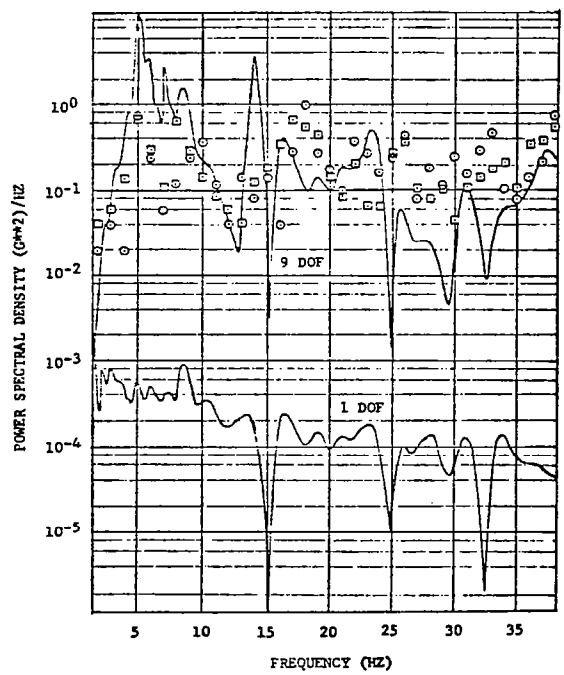

SPANWISE AND CHORDWISE PHASING

Figure 12.- (c) $\alpha = 14.4^{o}$

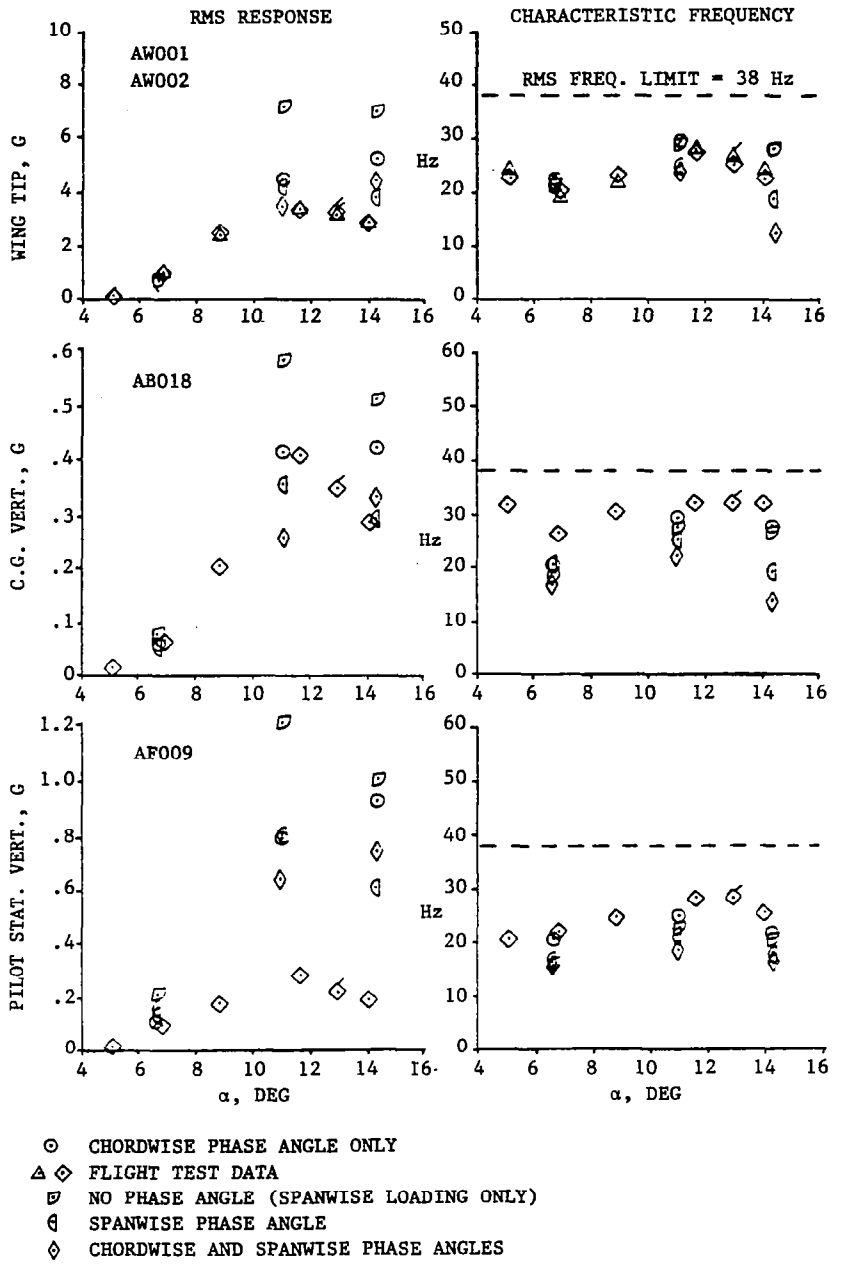

Figure 13.- Effect of buffet pressure spanwise and chordwise phasing on wing alone response RMS and N_o results for $\Lambda = 26^o$, M = 0.80, alt = 6035m
(a) accelerometer response

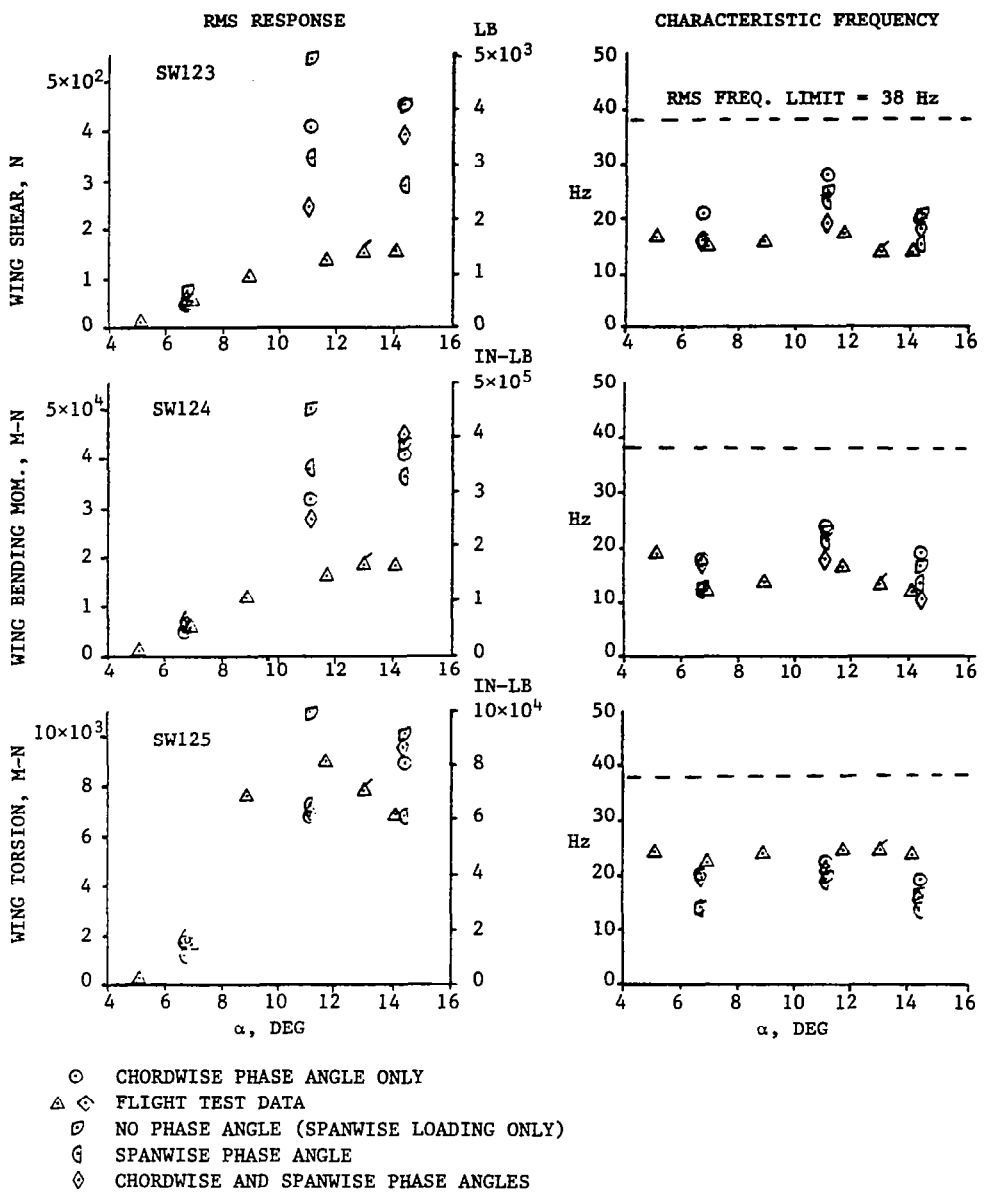

Figure 13.- (b) wing loading response

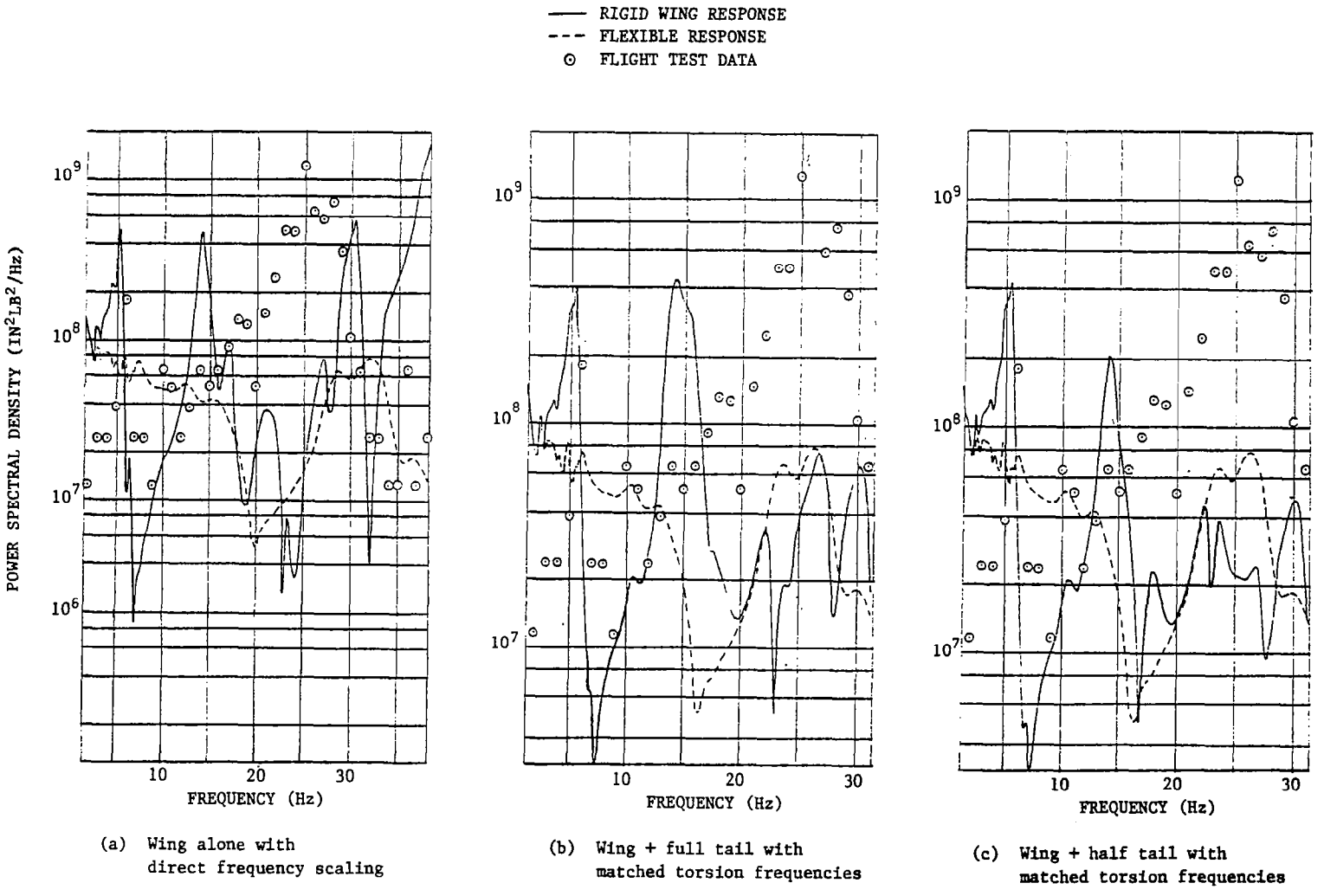

Figure 14.- Effect of matching torsion mode frequencies and total airplane aerodynamics on wing torsion response

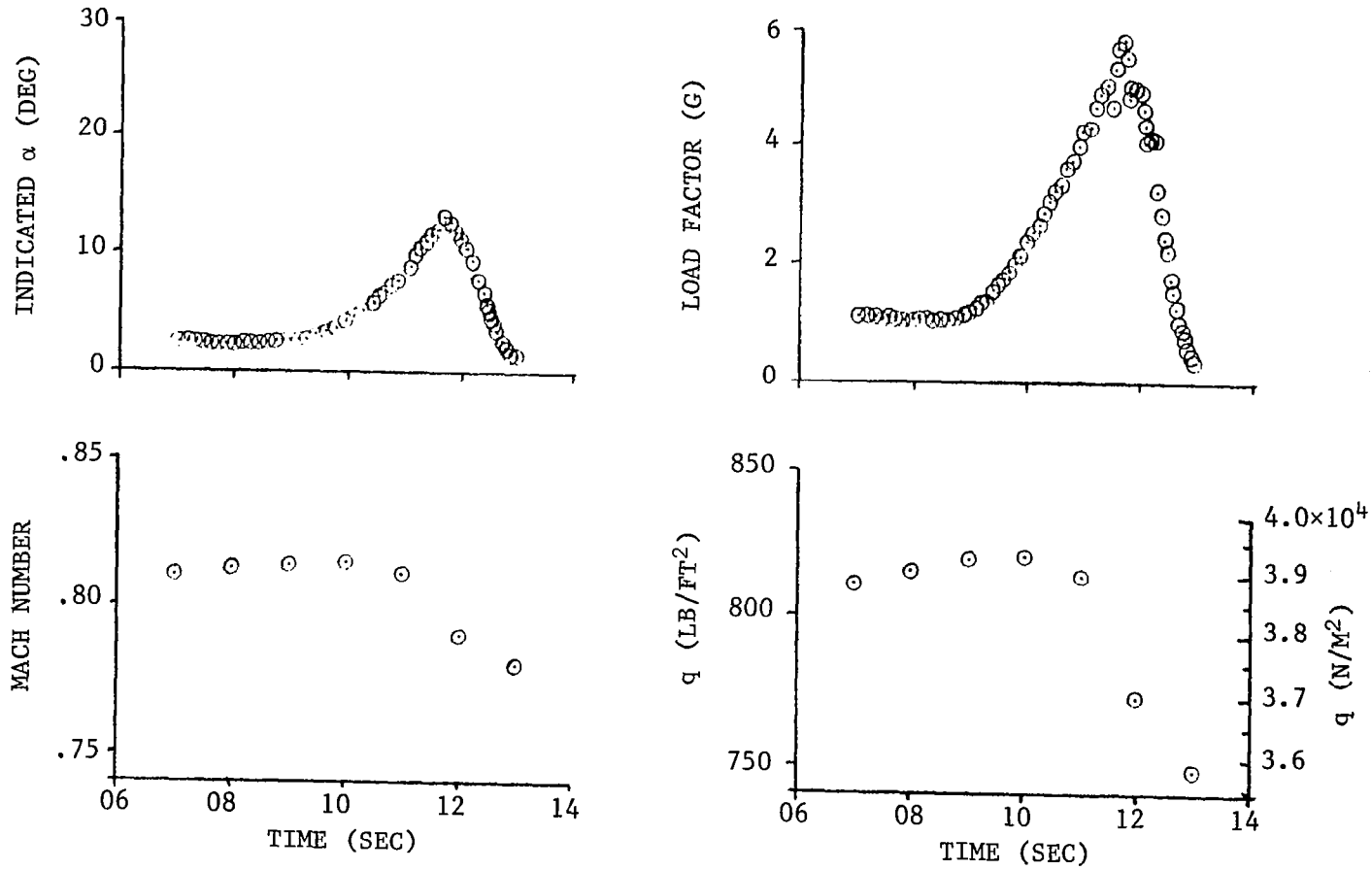

Figure 15.- Flight parameters for the flight 79 maneuver

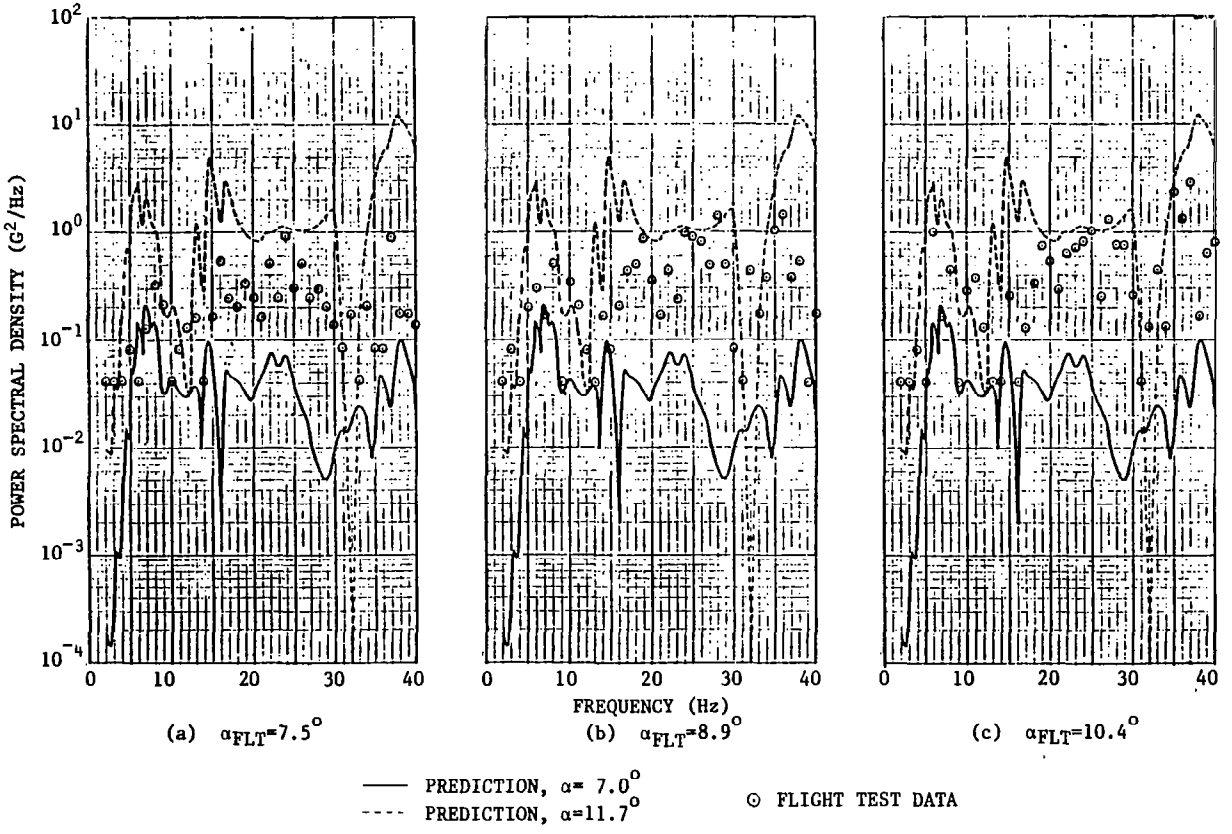

Figure 16.- Comparison of flight test and predicted response for wing tip accelerometer during the flight 79 maneuver

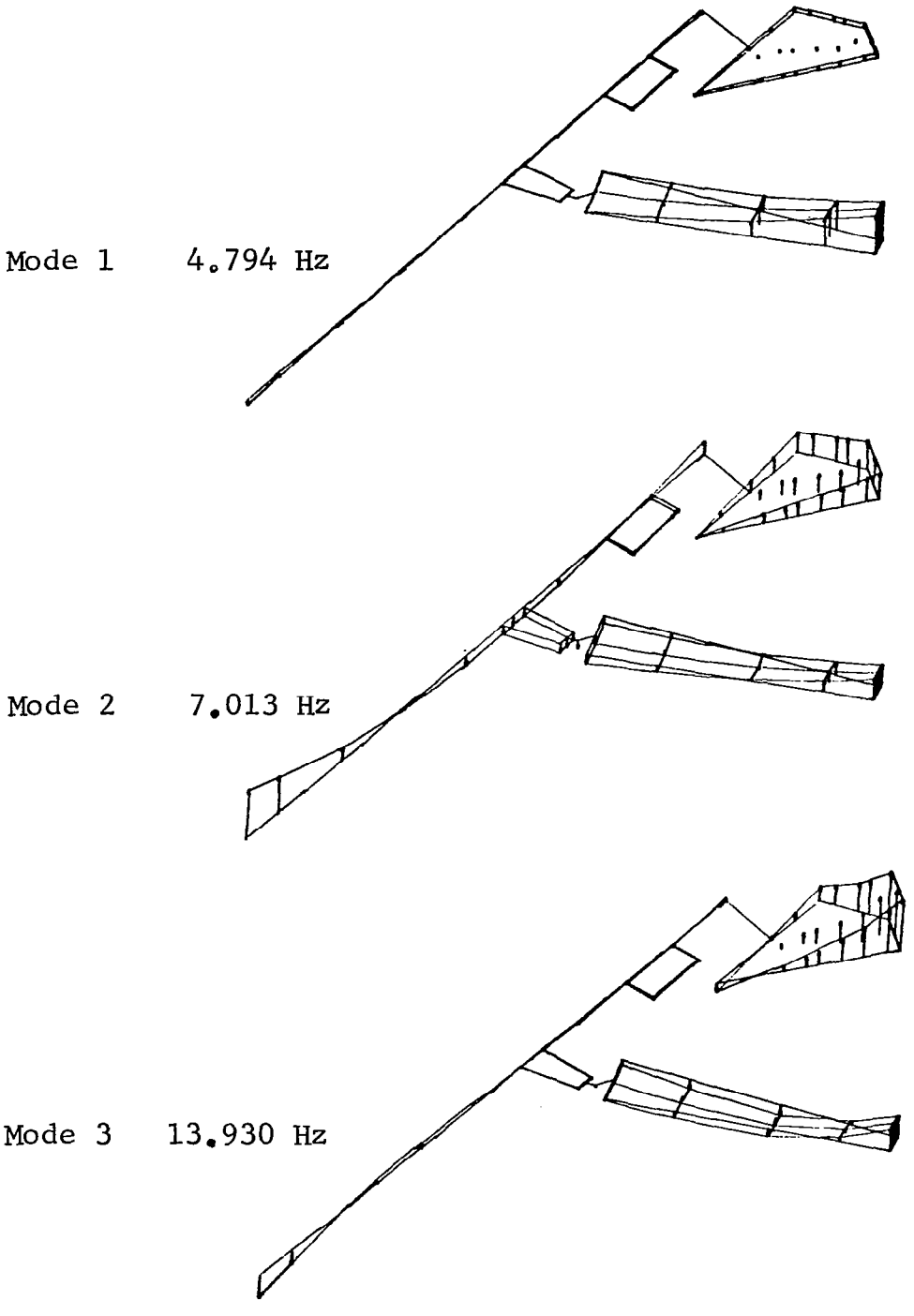

Figure 17.- Calculated symmetric natural modes for cases 1 and 2, Λ=26.0 and G.W.=266,044N

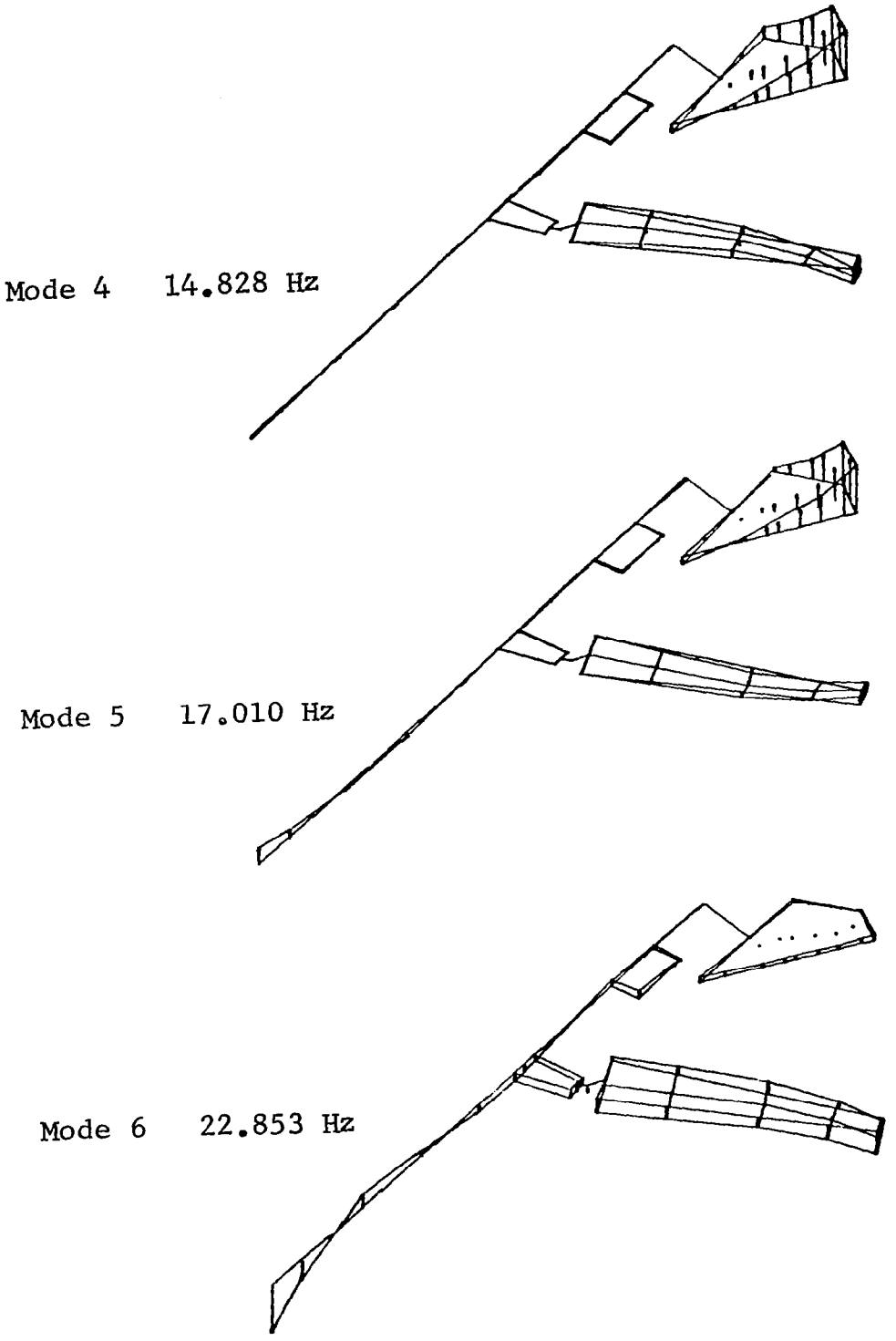

Figure 17.-(continued)

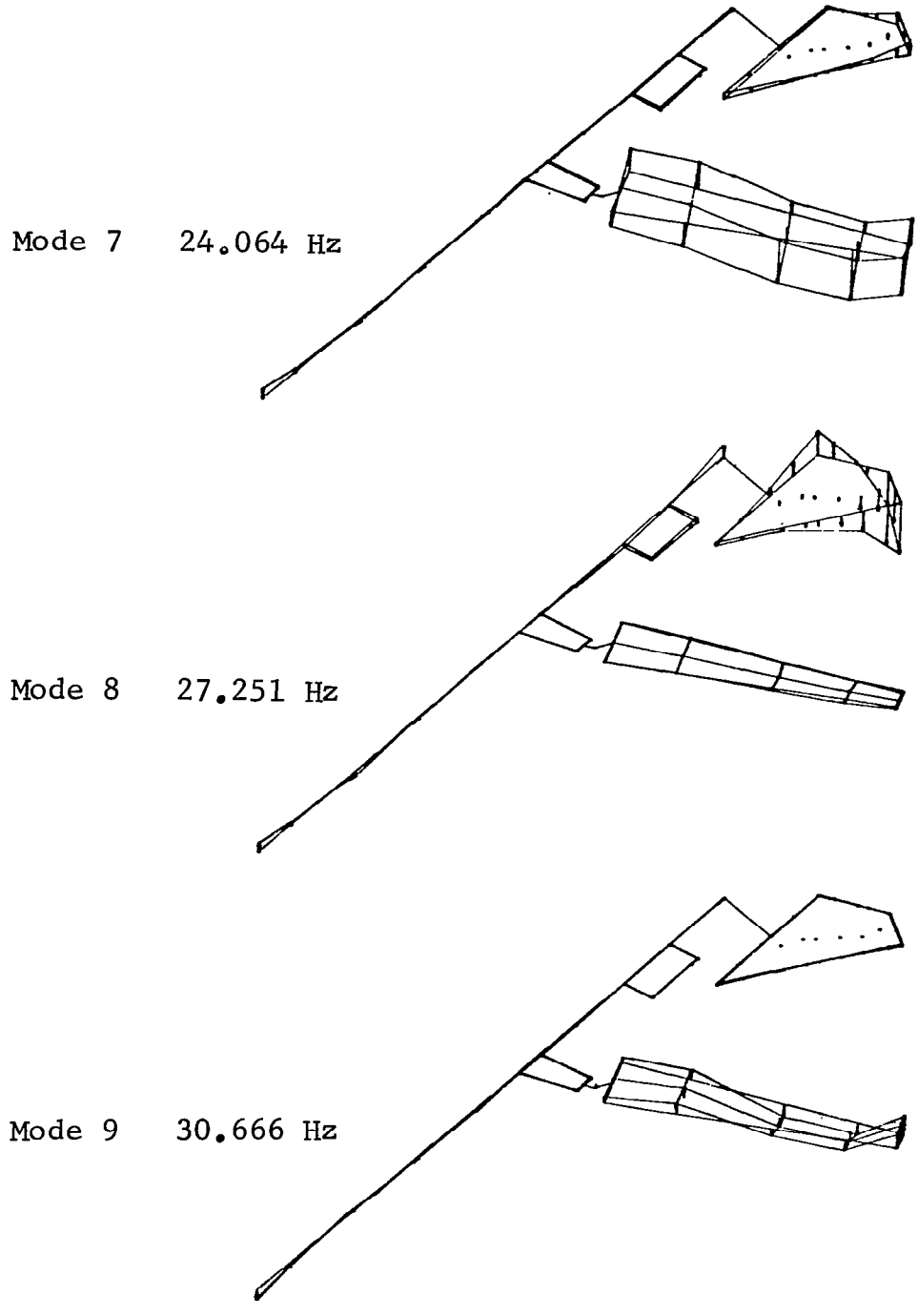

Figure 17.-(continued)

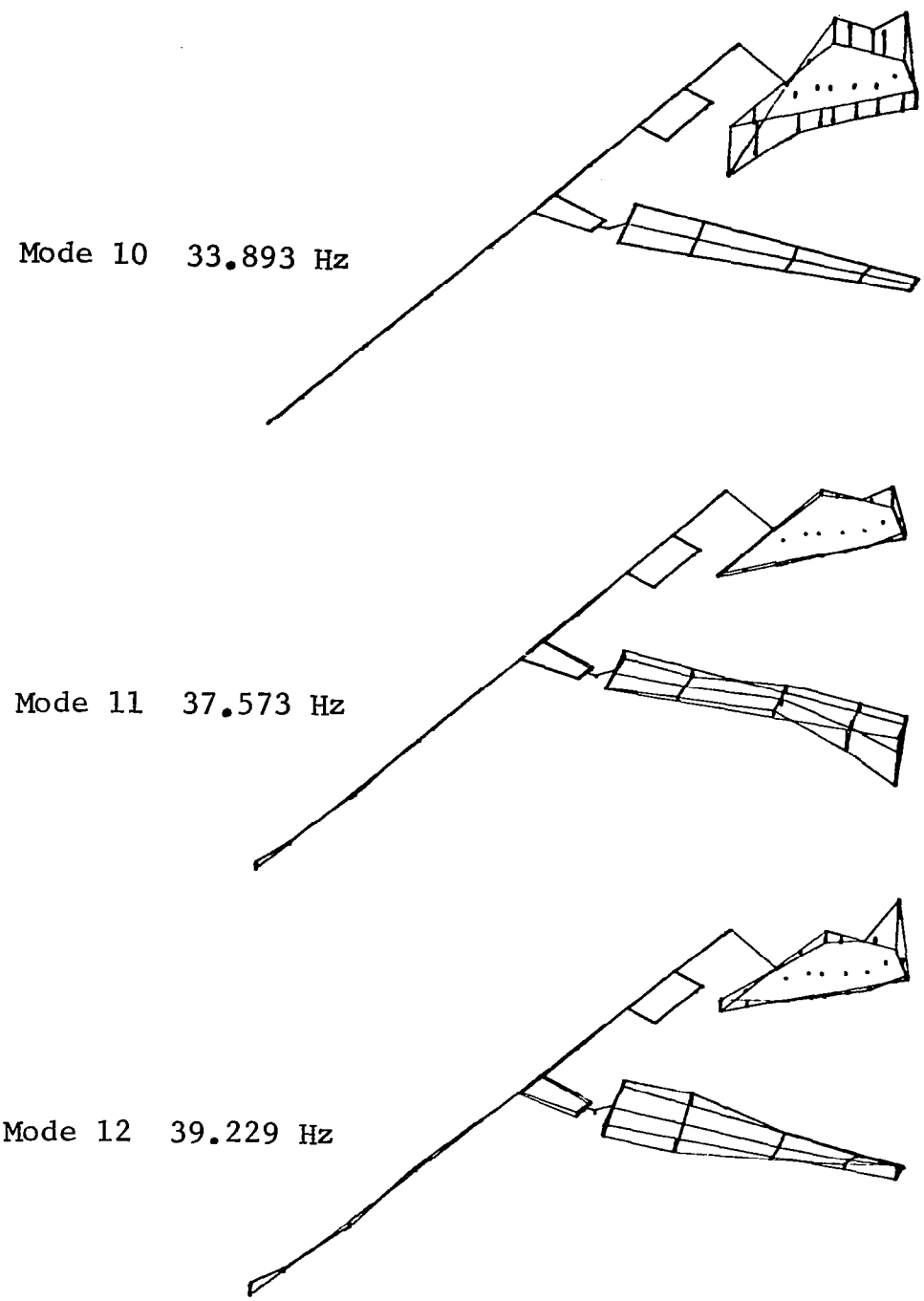

Figure 17.-(continued)

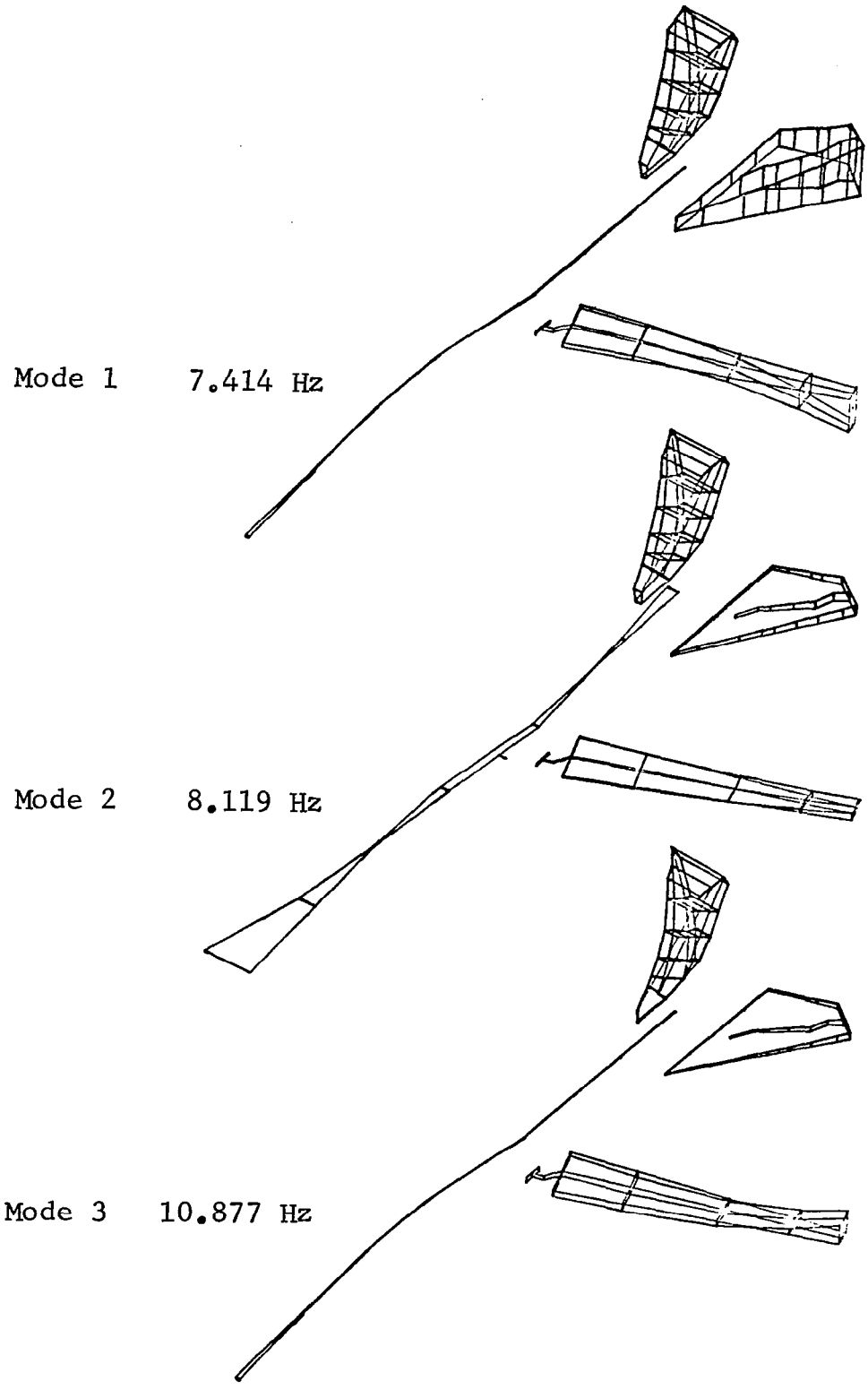

Figure 18.- Calculated antisymmetric natural modes for cases 1 and 2, $\Lambda=26.0^{\circ}$ and G.W.=266,044N

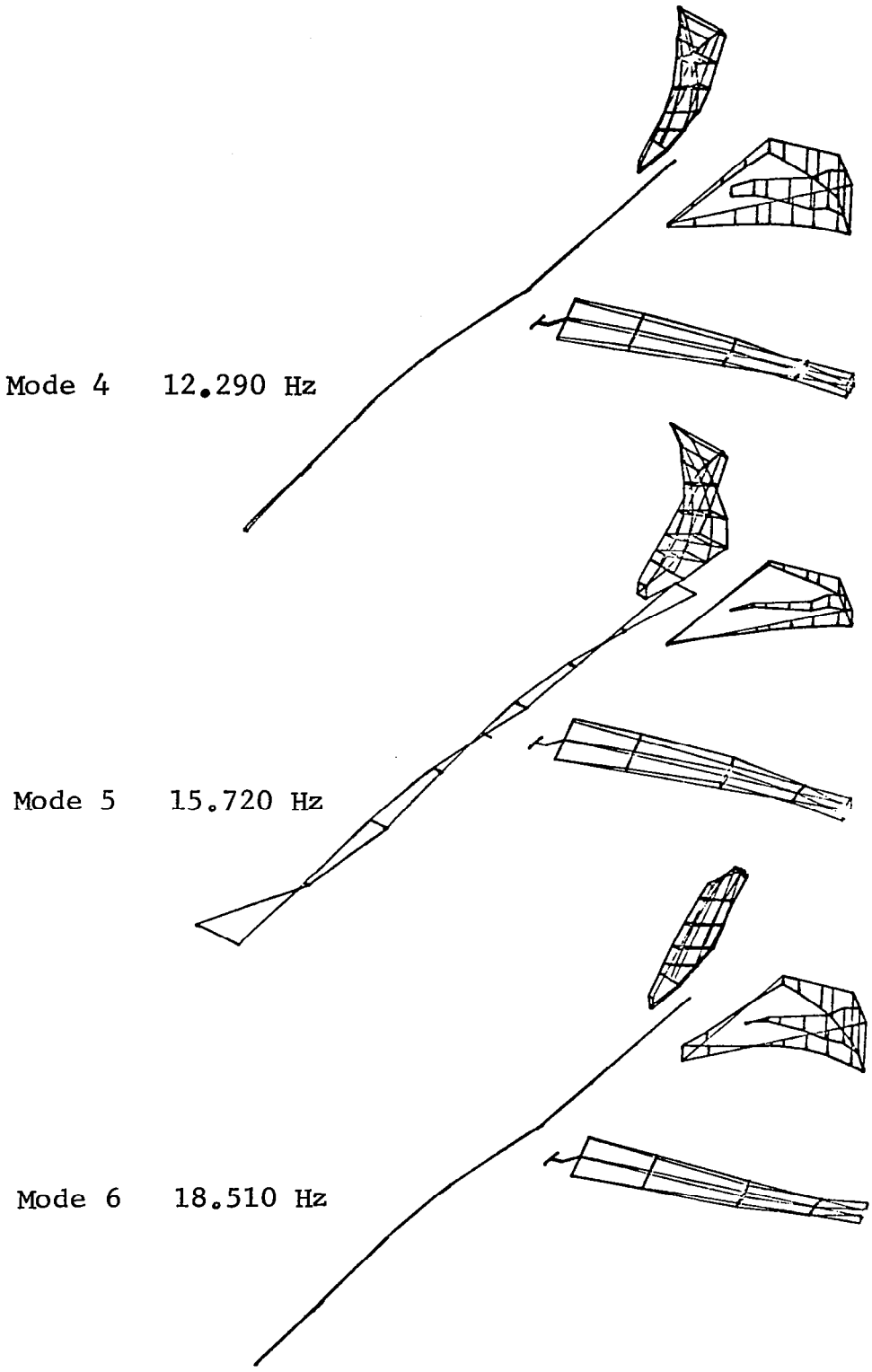

Figure 18.-(continued)

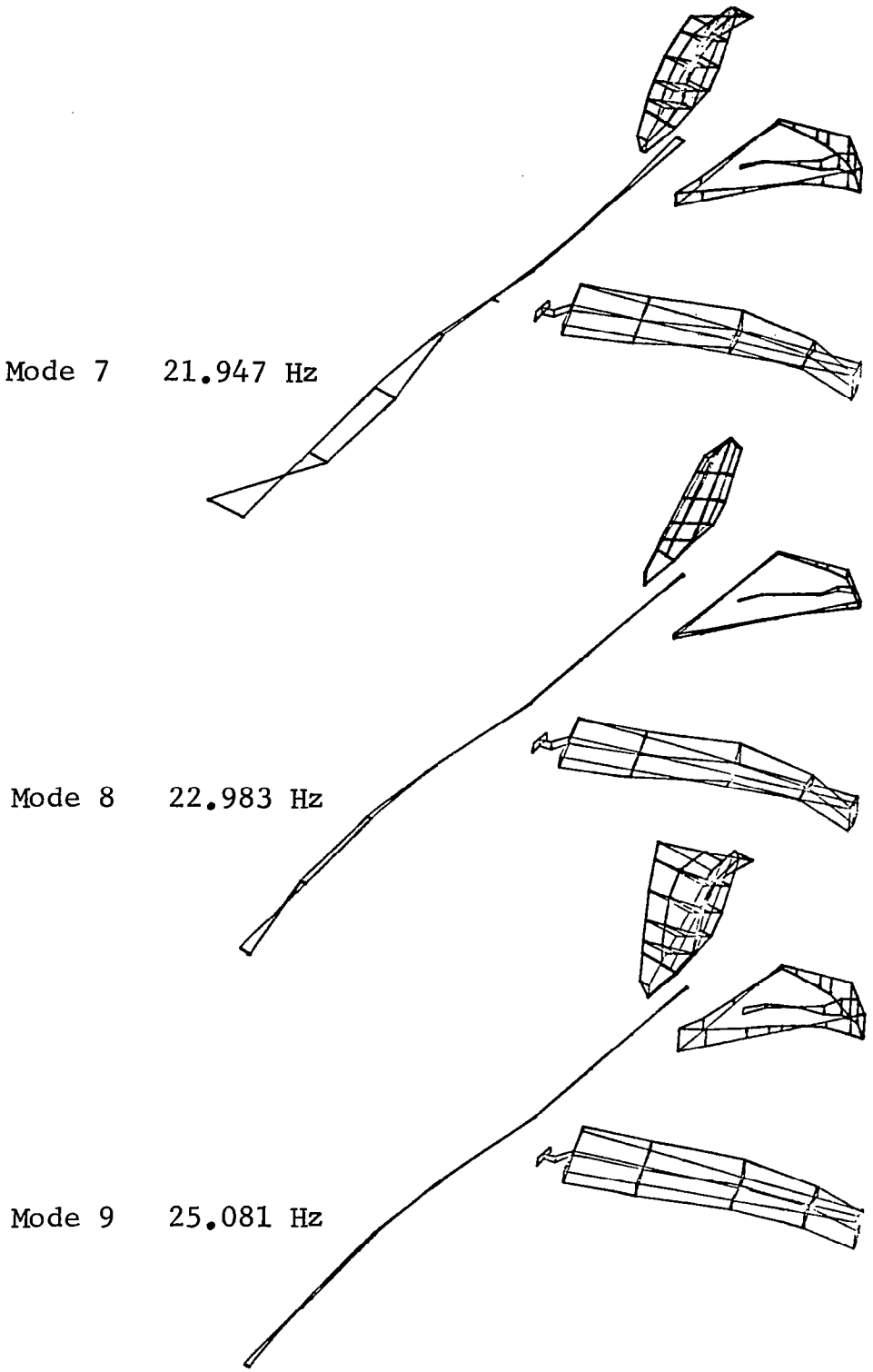

Figure 18.-(continued)

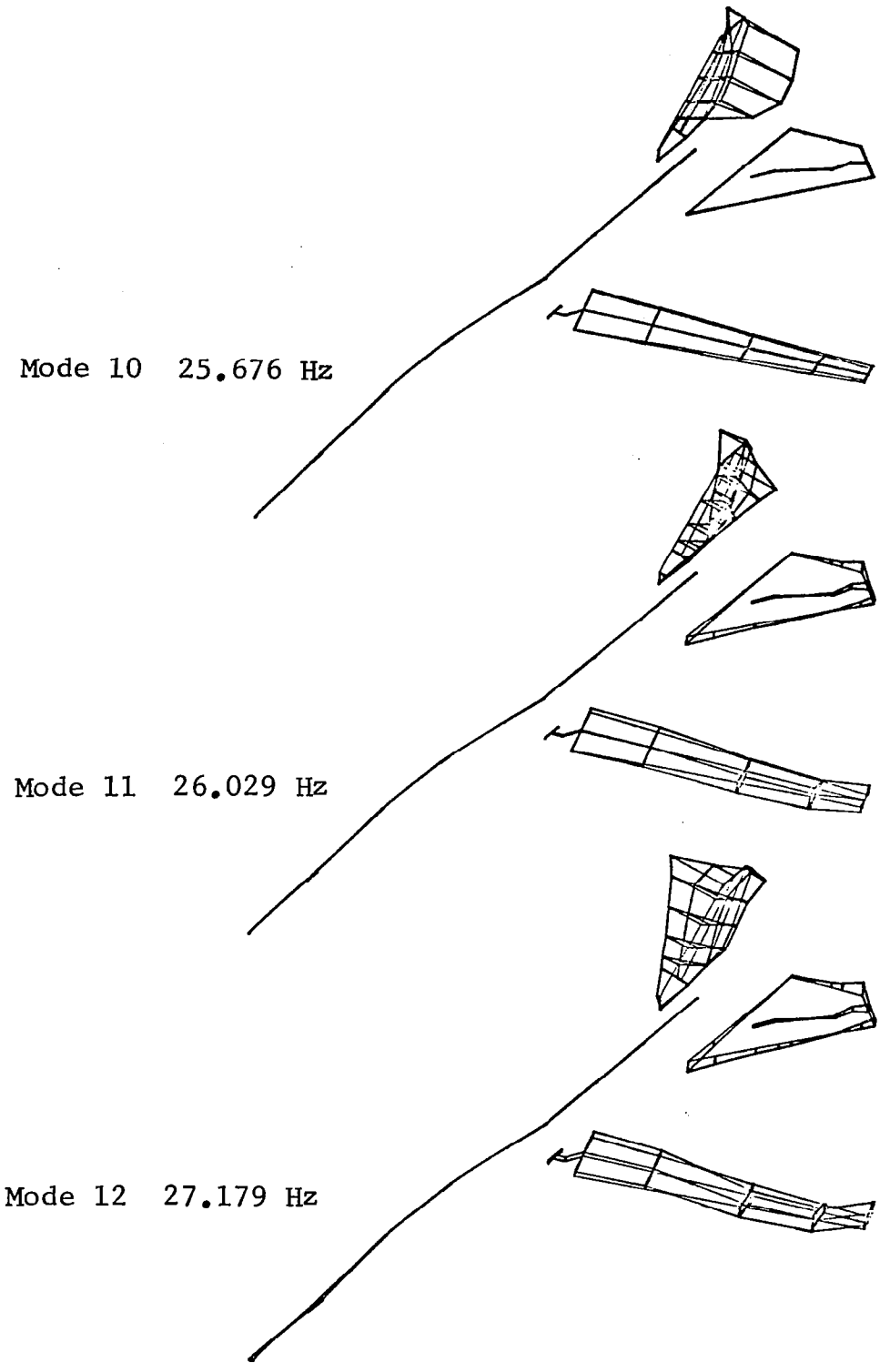

Figure 18.-(continued)

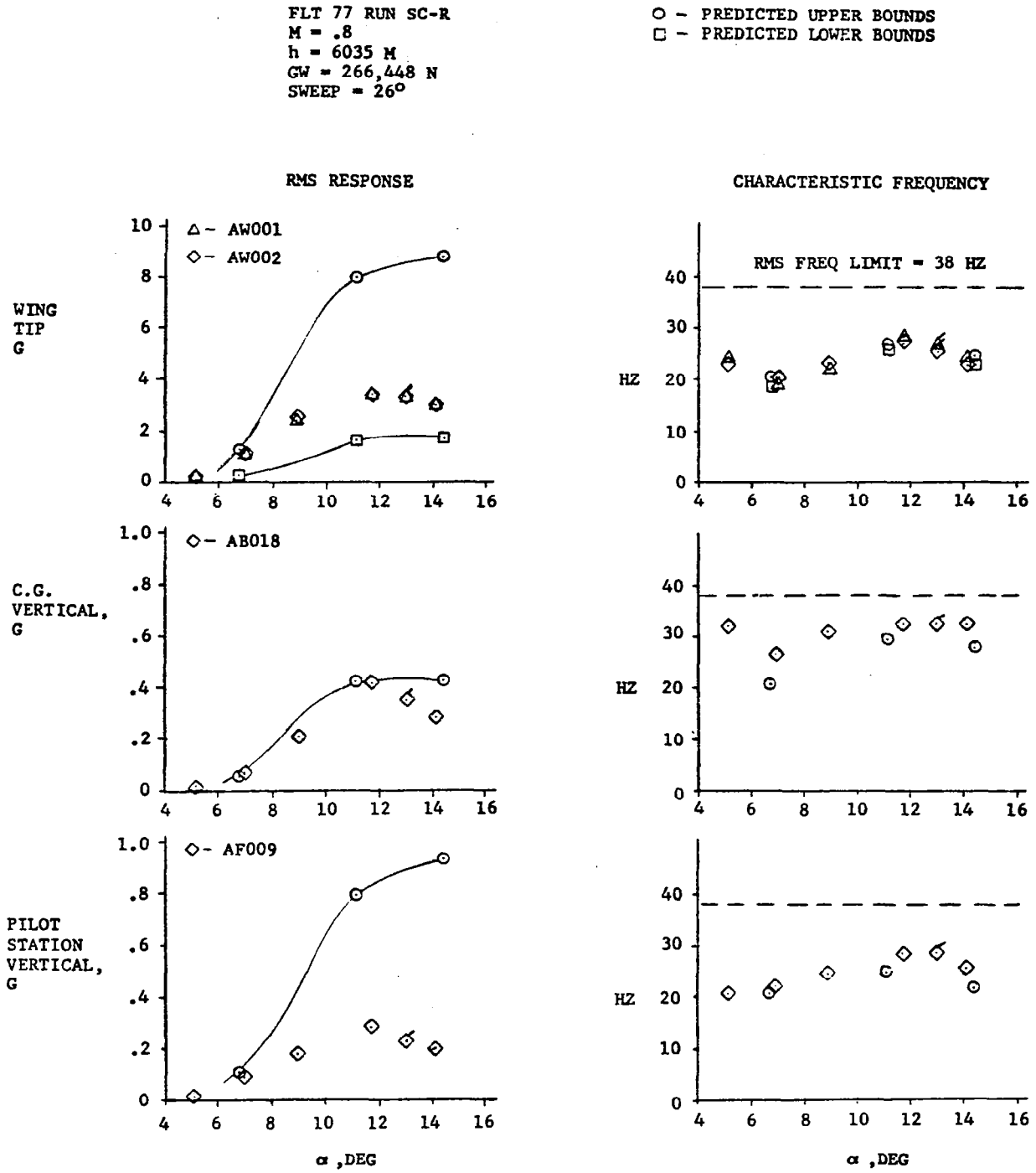

Figure 19.- Response predictions for case 1

FLT 77 RUN SC-R
M = .8
h = 6035 M
GW = 266,448 N
SWEEP = 26°

○ - PREDICTED UPPER BOUNDS
□ - PREDICTED LOWER BOUNDS

RMS RESPONSE

CHARACTERISTIC FREQUENCY

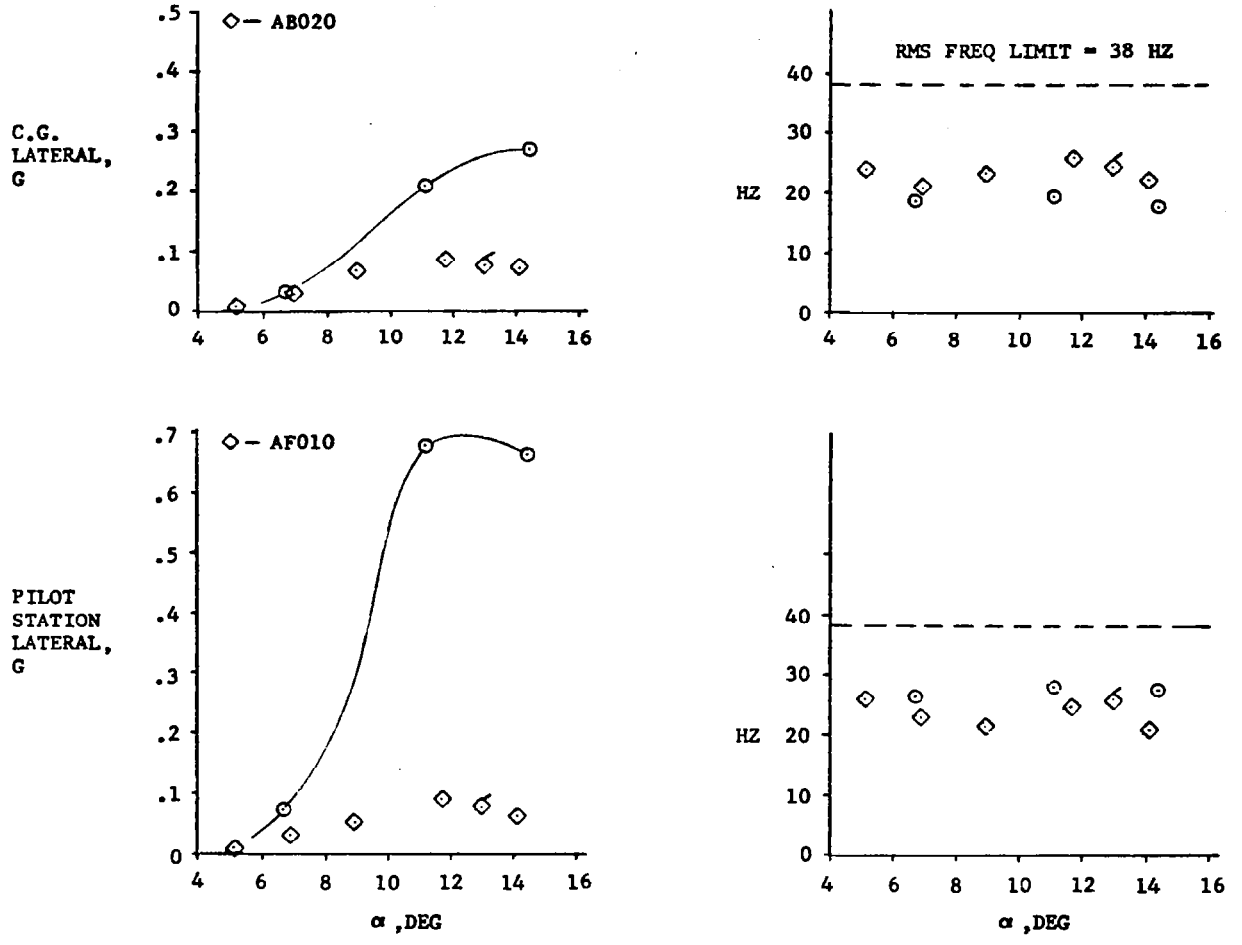

Figure 19.-(continued)

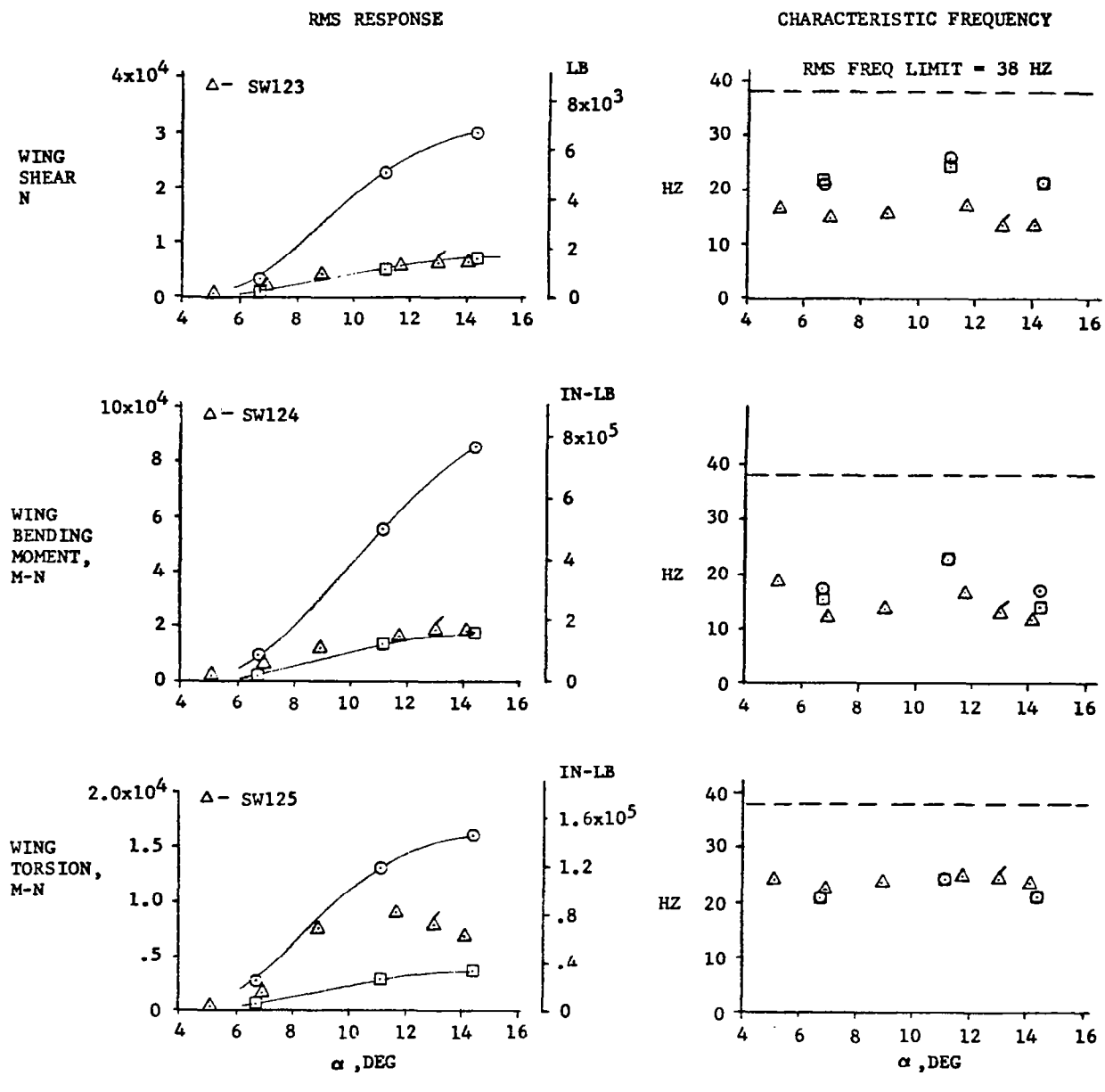

Figure 19.-(continued)

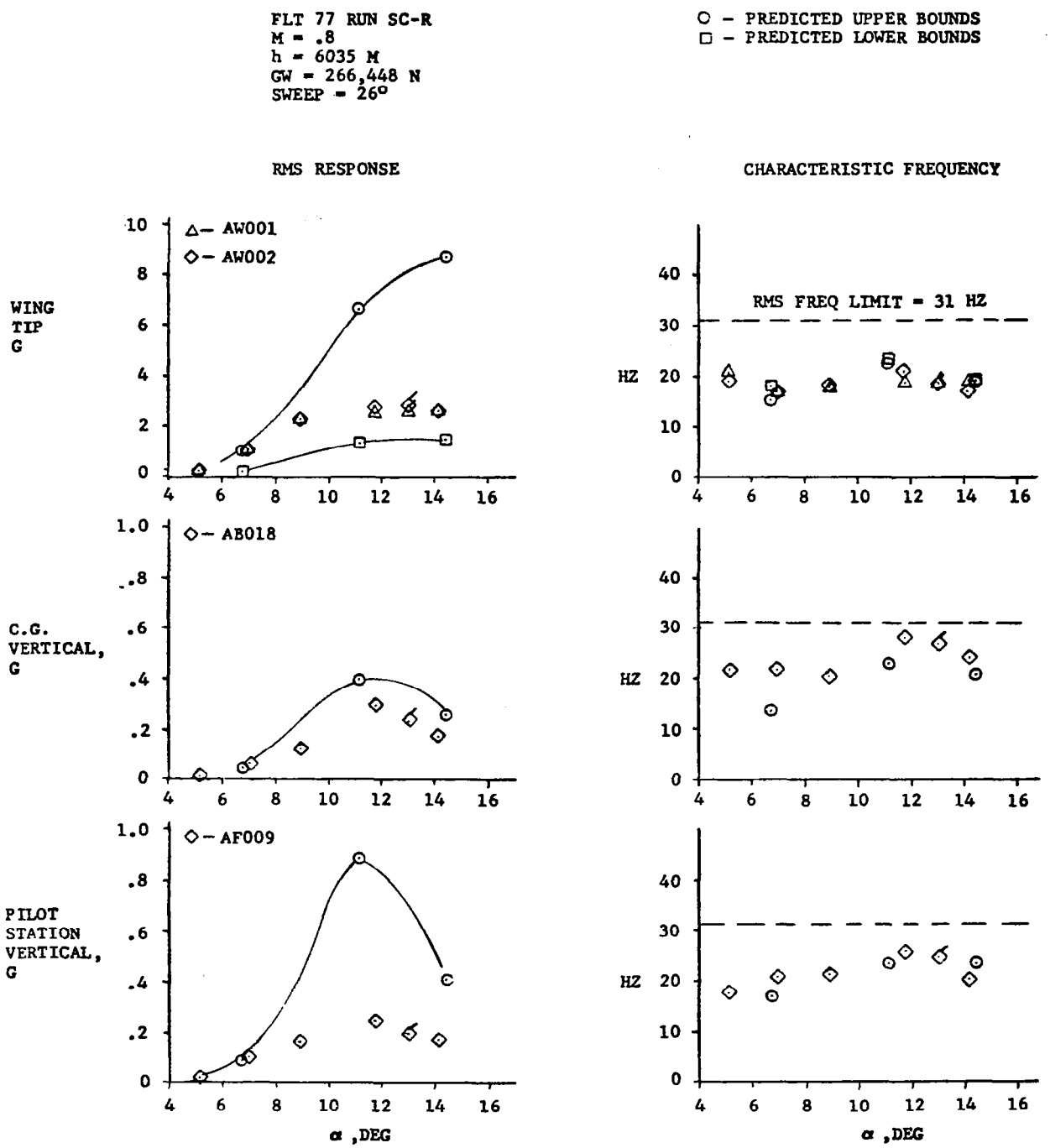

Figure 20.- Response predictions for case 2

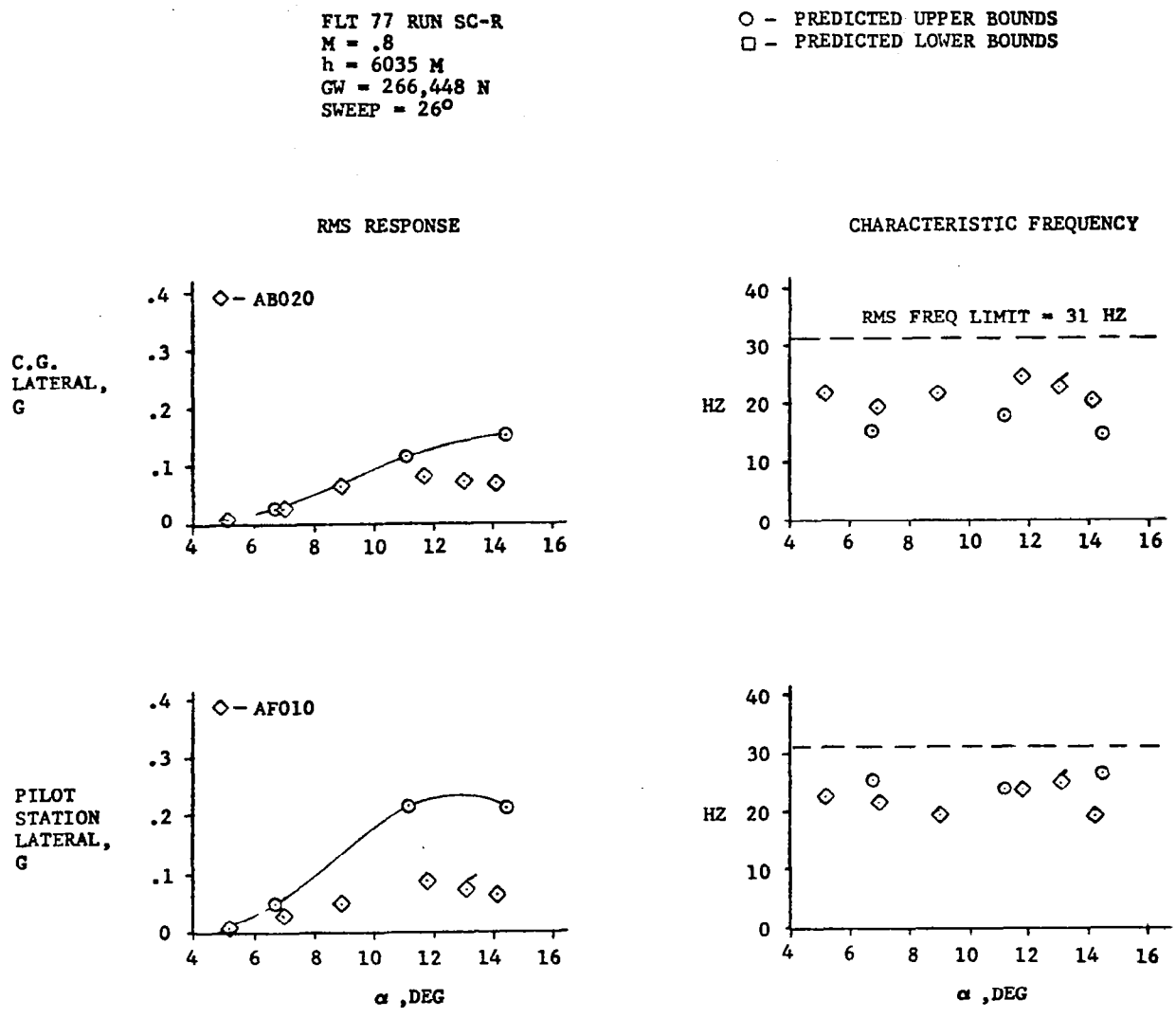

Figure 20.-(continued)

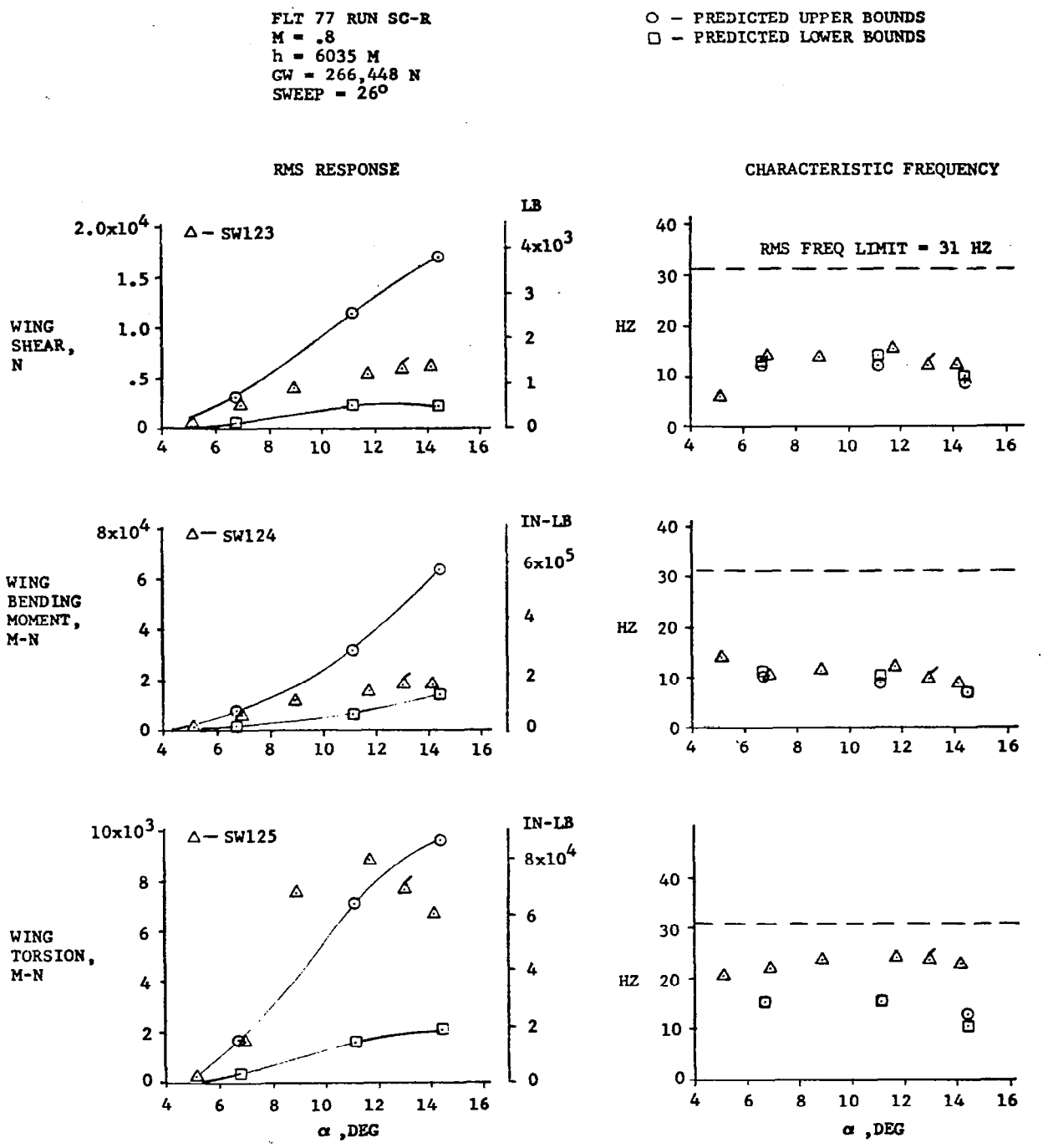

Figure 20.-(continued)

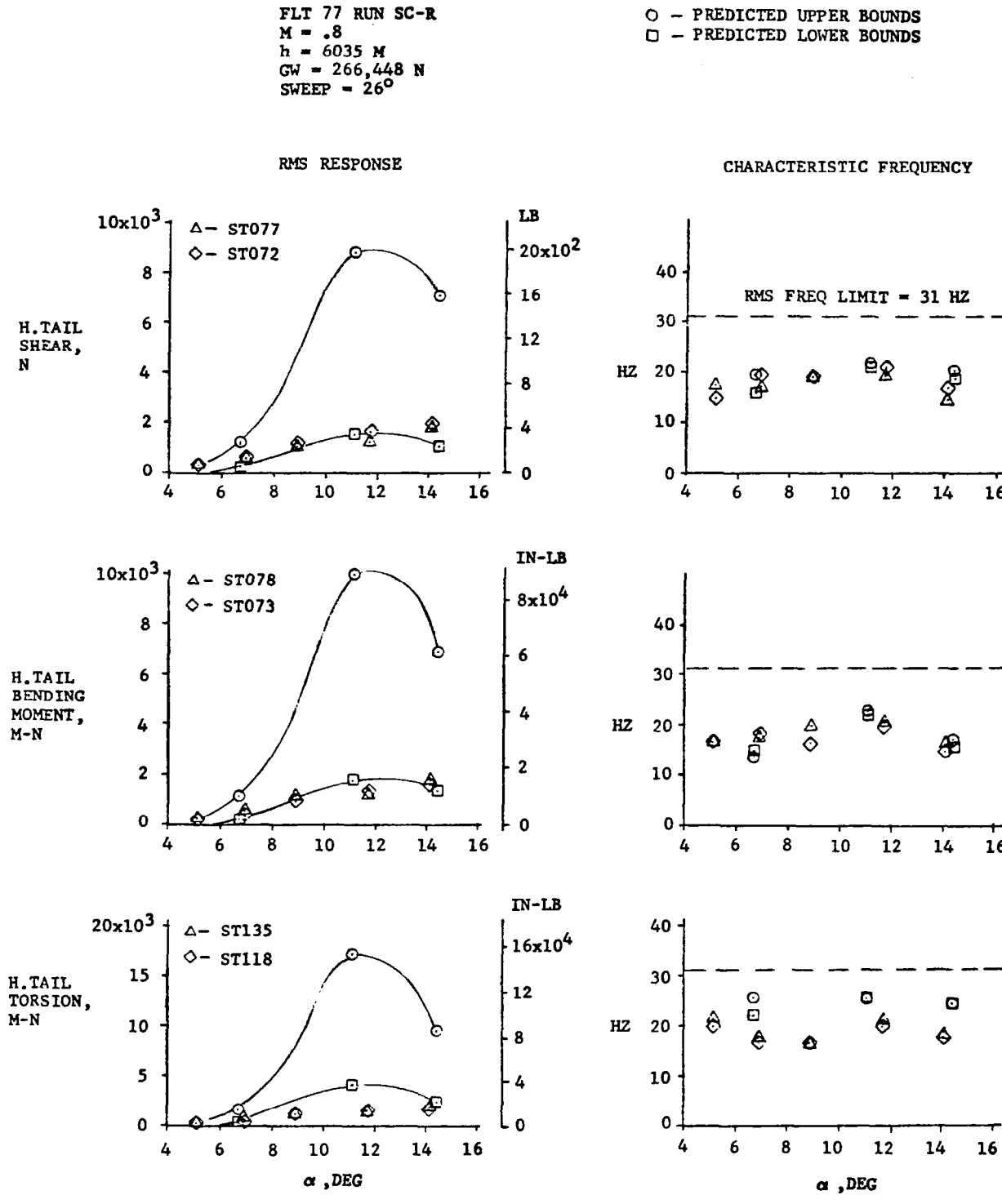

Figure 20.-(continued)

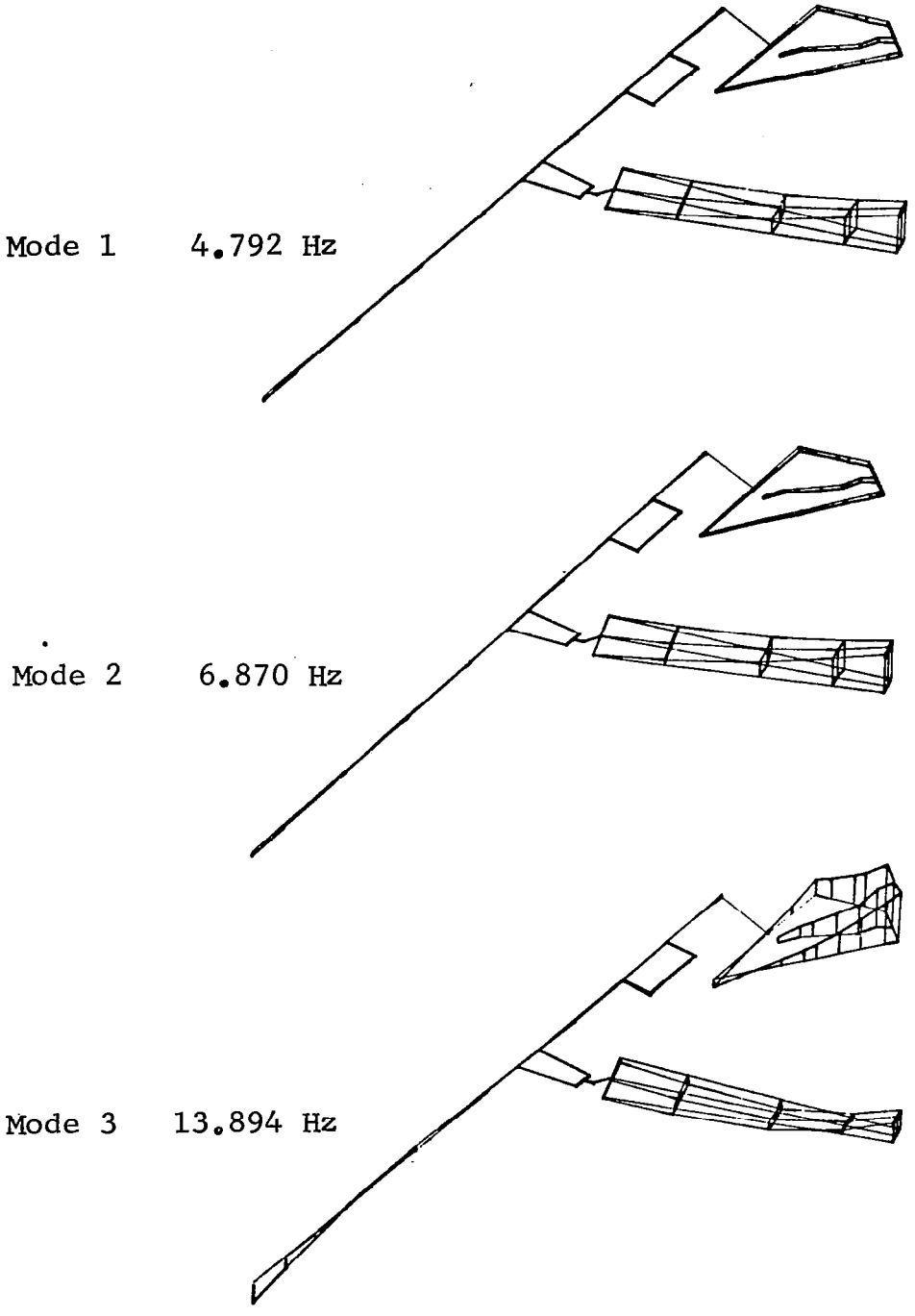

Figure 21.- Calculated symmetric natural modes for case 3, $\Lambda=26.0^{\circ}$ and G.W.=293,138N

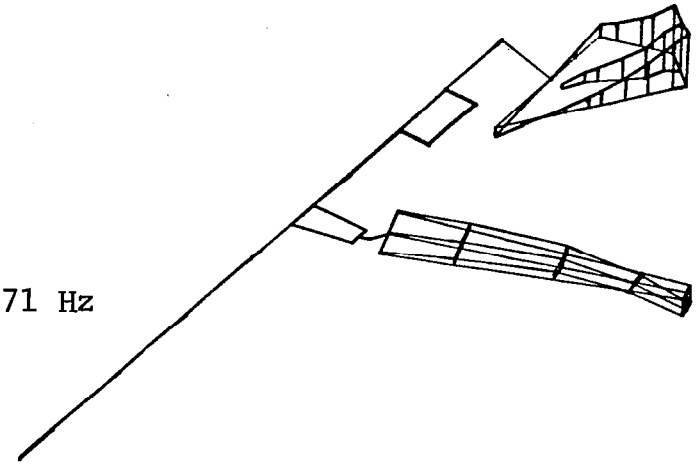

Mode 4 14.771 Hz

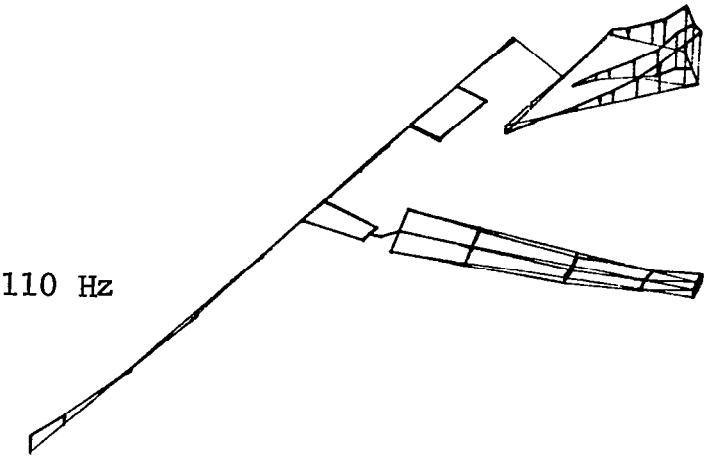

Mode 5 17.110 Hz

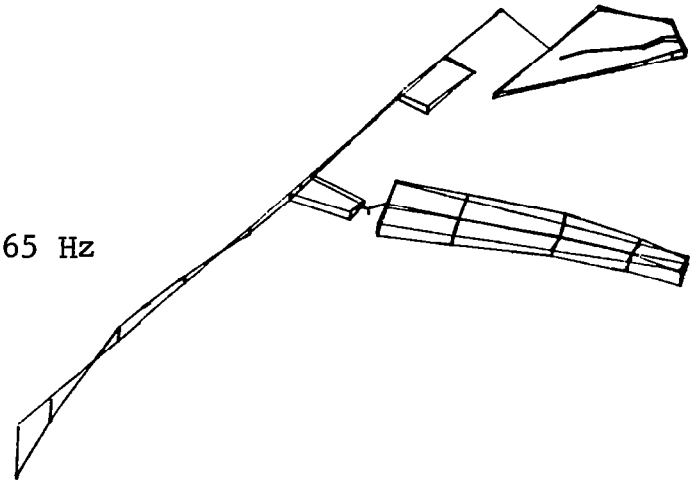

Mode 6 22.665 Hz

Figure 21.-(continued)

Mode 7 24.024 Hz

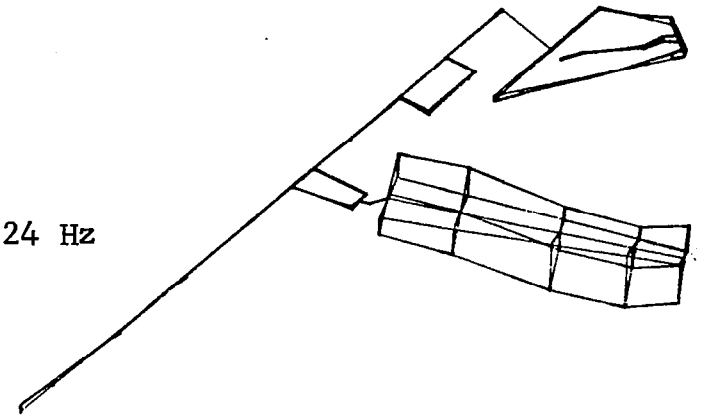

Mode 8 27.197 Hz

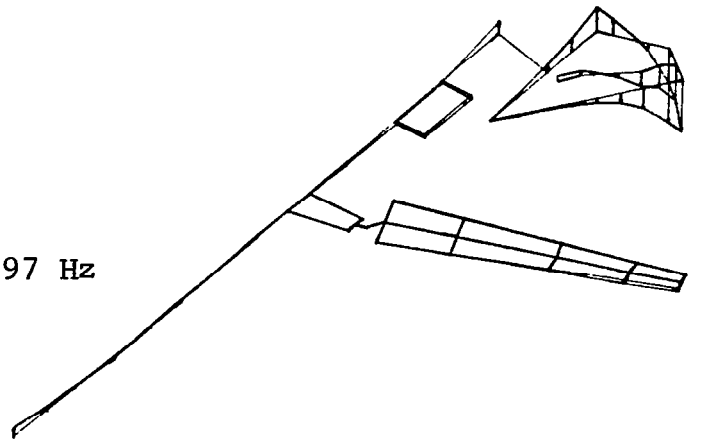

Mode 9 30.446 Hz

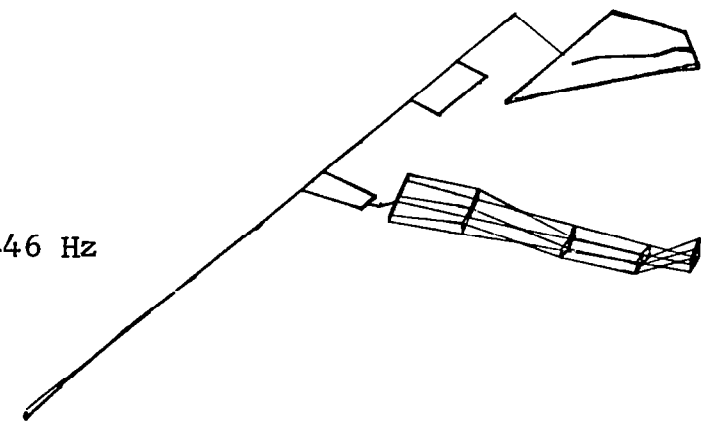

Figure 21.-(continued)

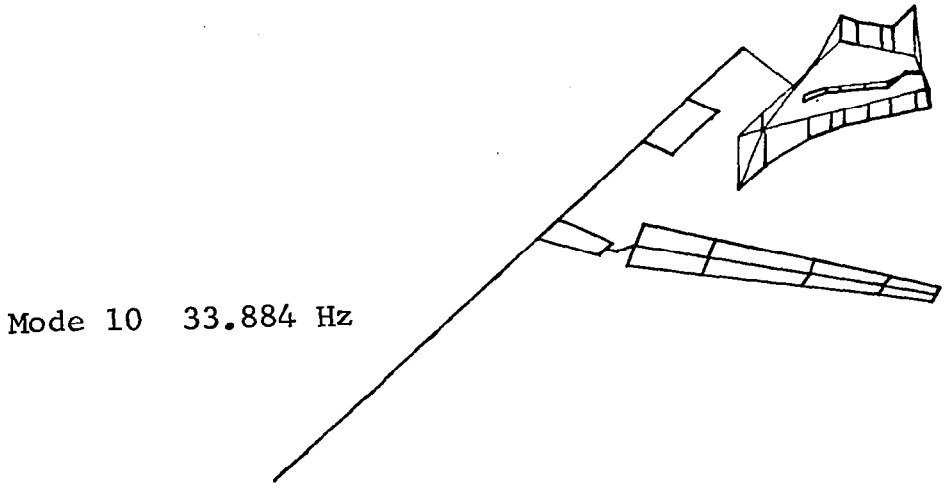

Mode 10 33.884 Hz

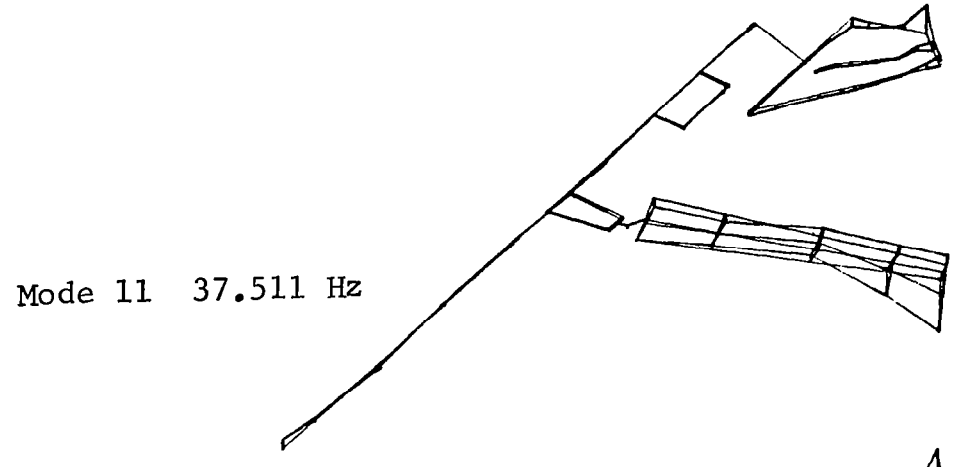

Mode 11 37.511 Hz

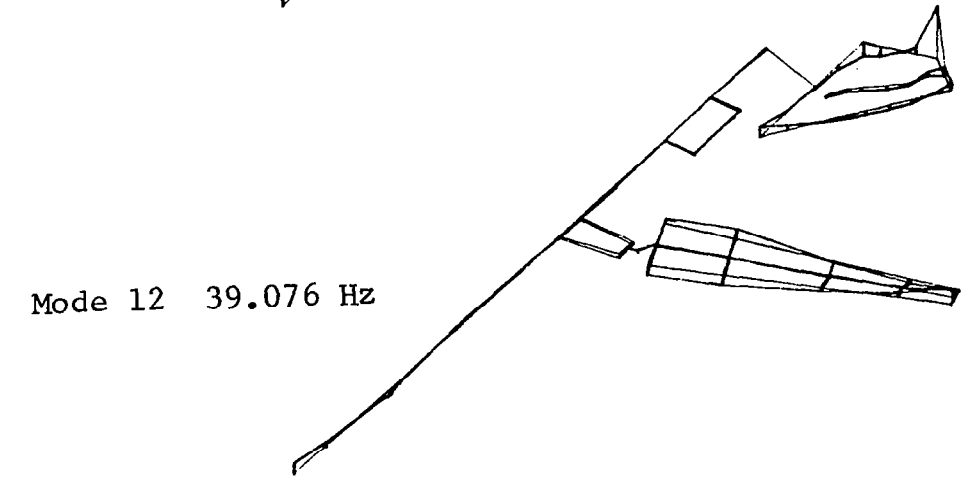

Mode 12 39.076 Hz

Figure 21.-(continued)

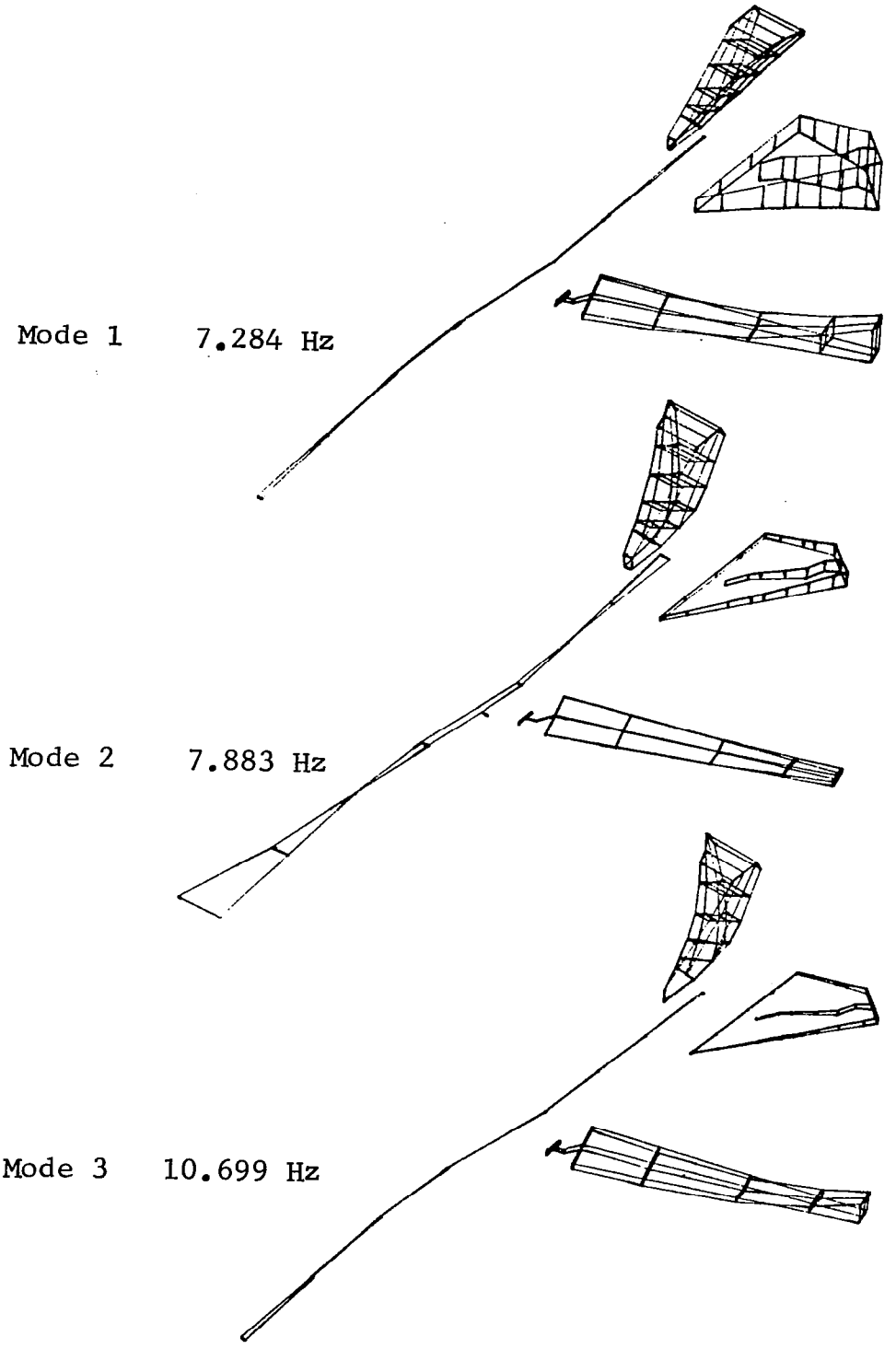

Figure 22.- Calculated antisymmetric natural modes for case 3, $\Lambda=26.0^{\circ}$ and G.W.=293,138N

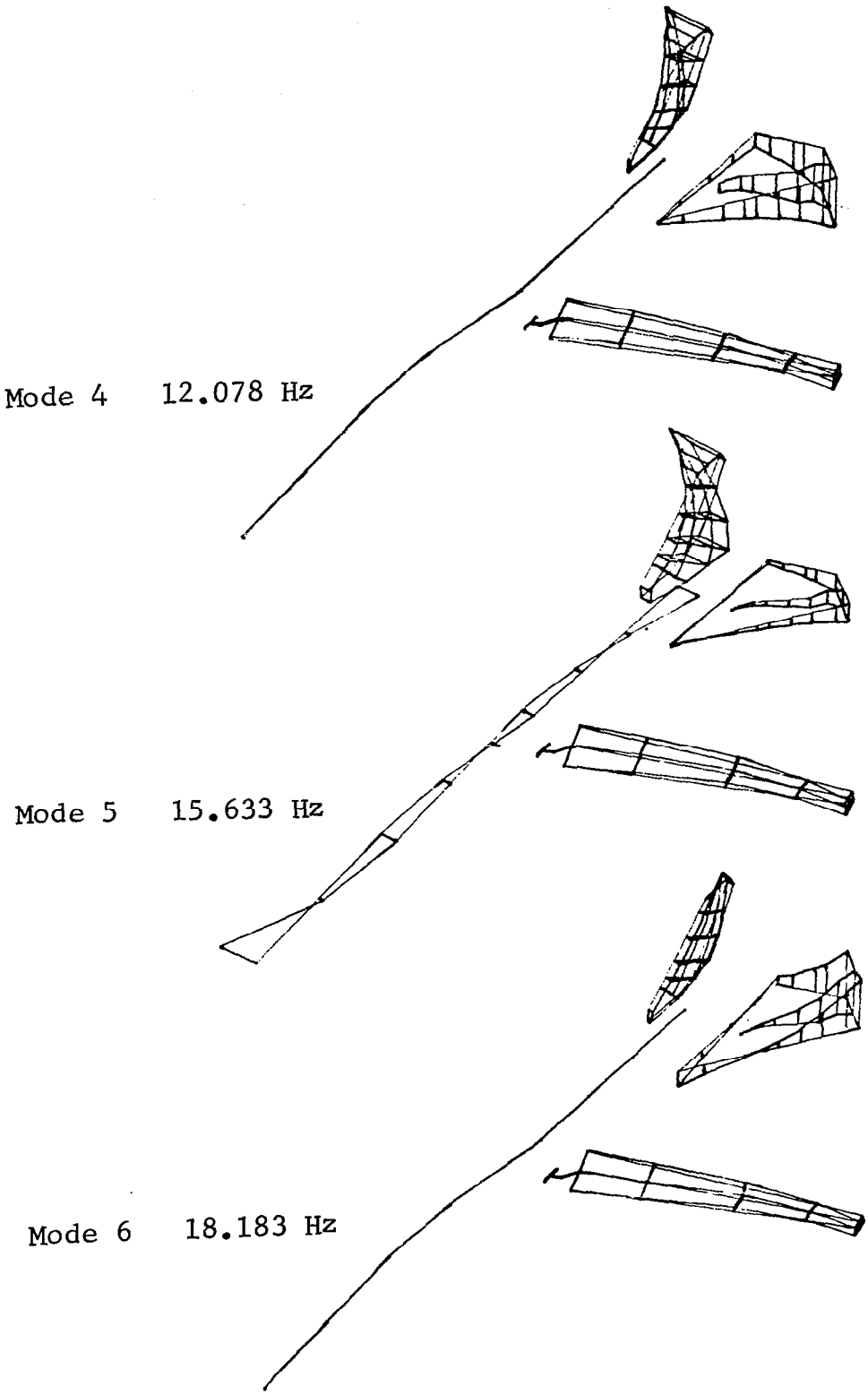

Figure 22.-(continued)

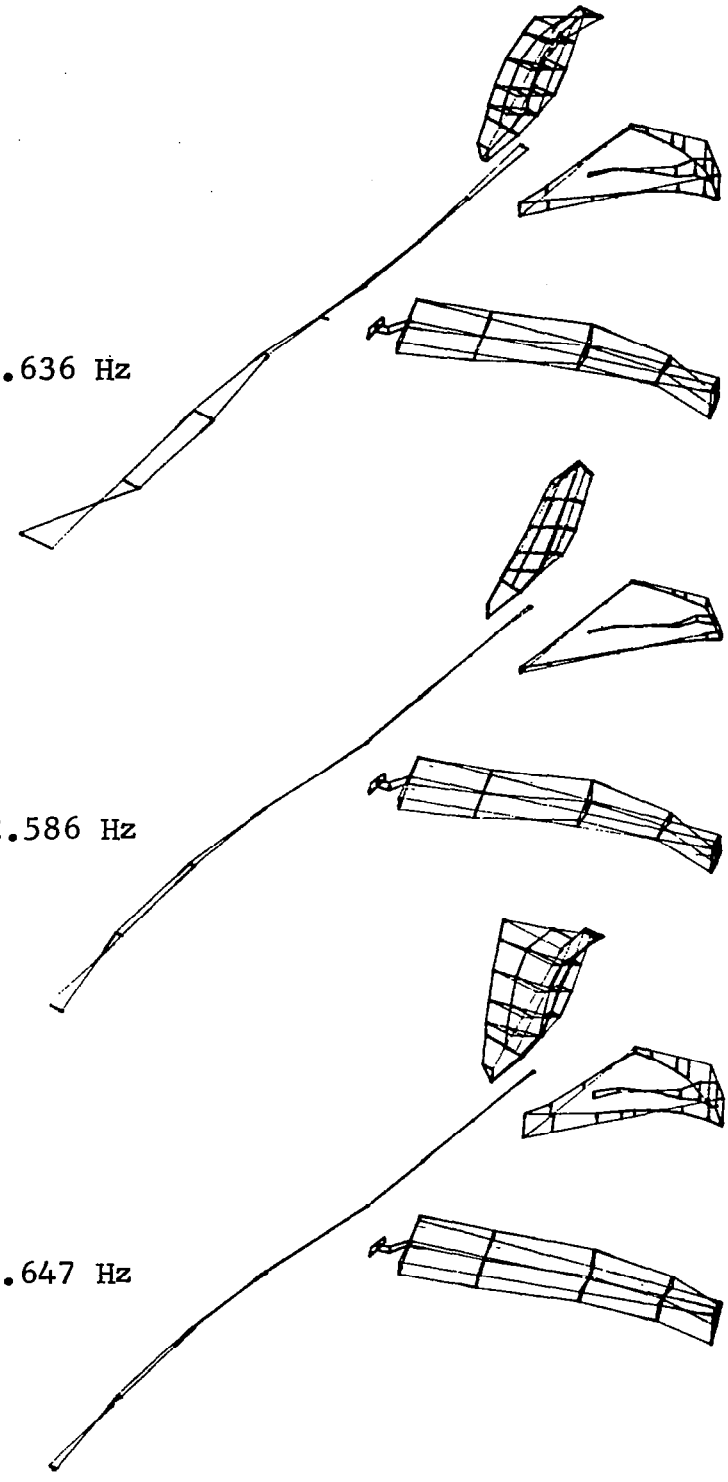

Figure 22.-(continued)

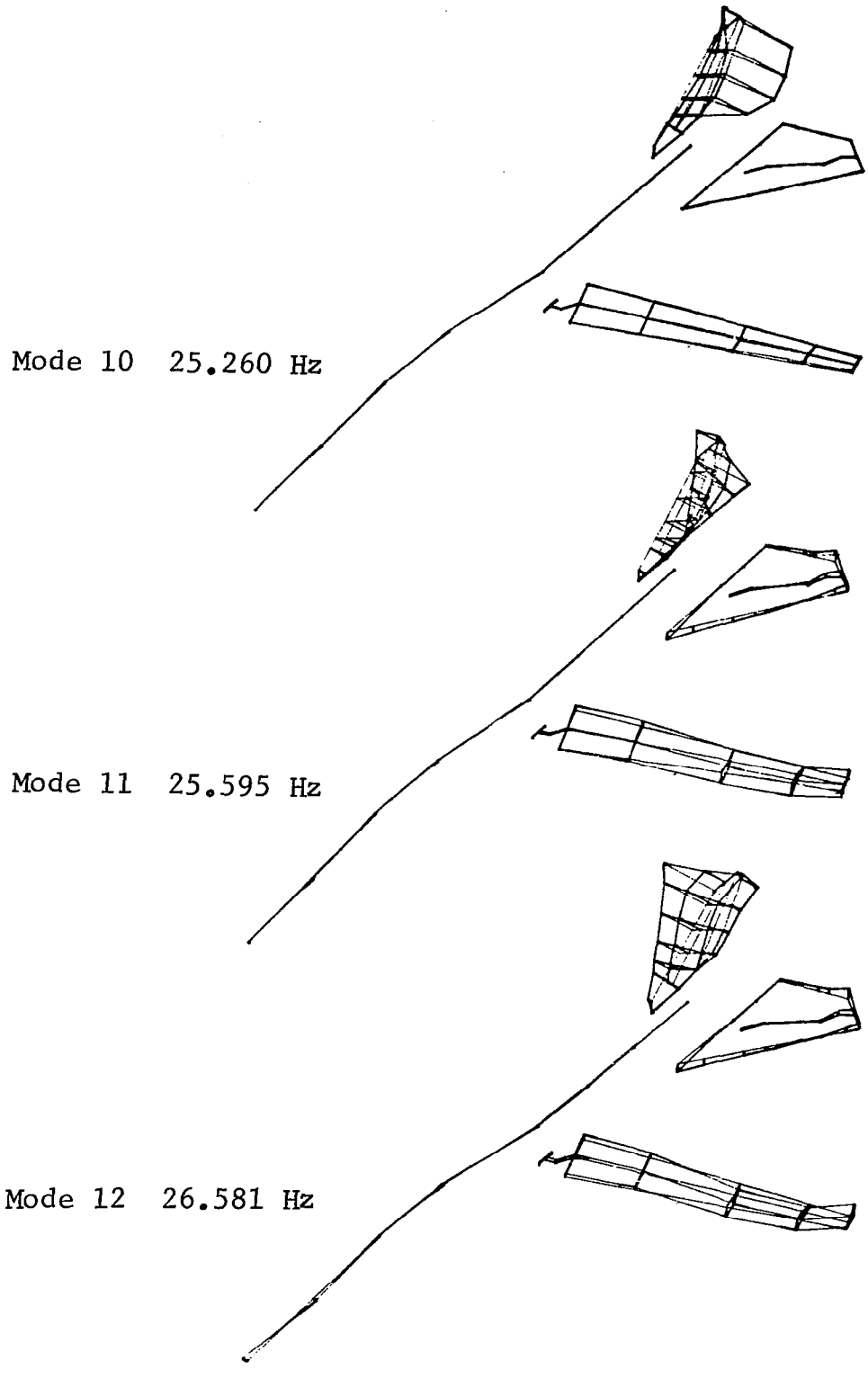

Figure 22.-(continued)

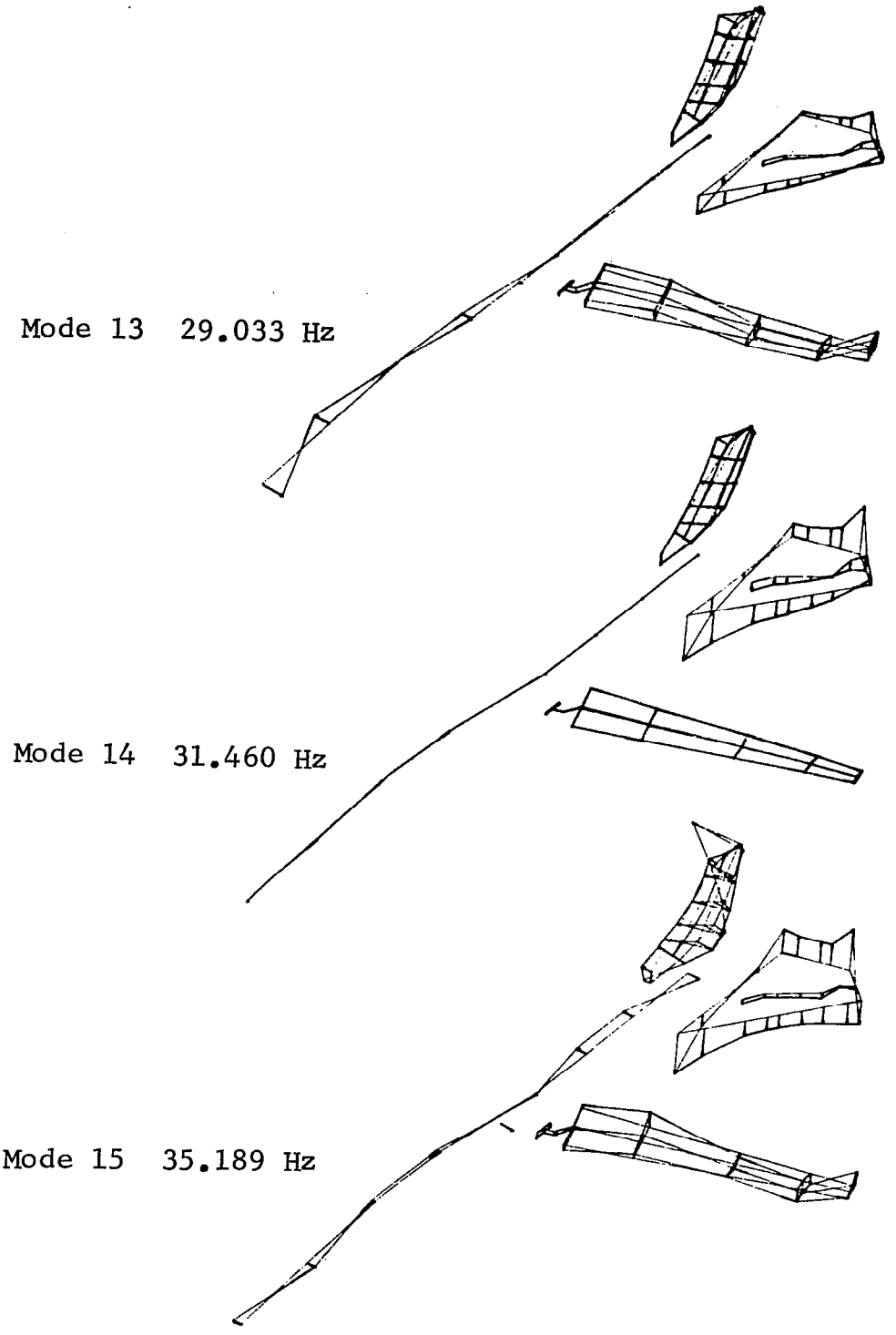

Figure 22.-(continued)

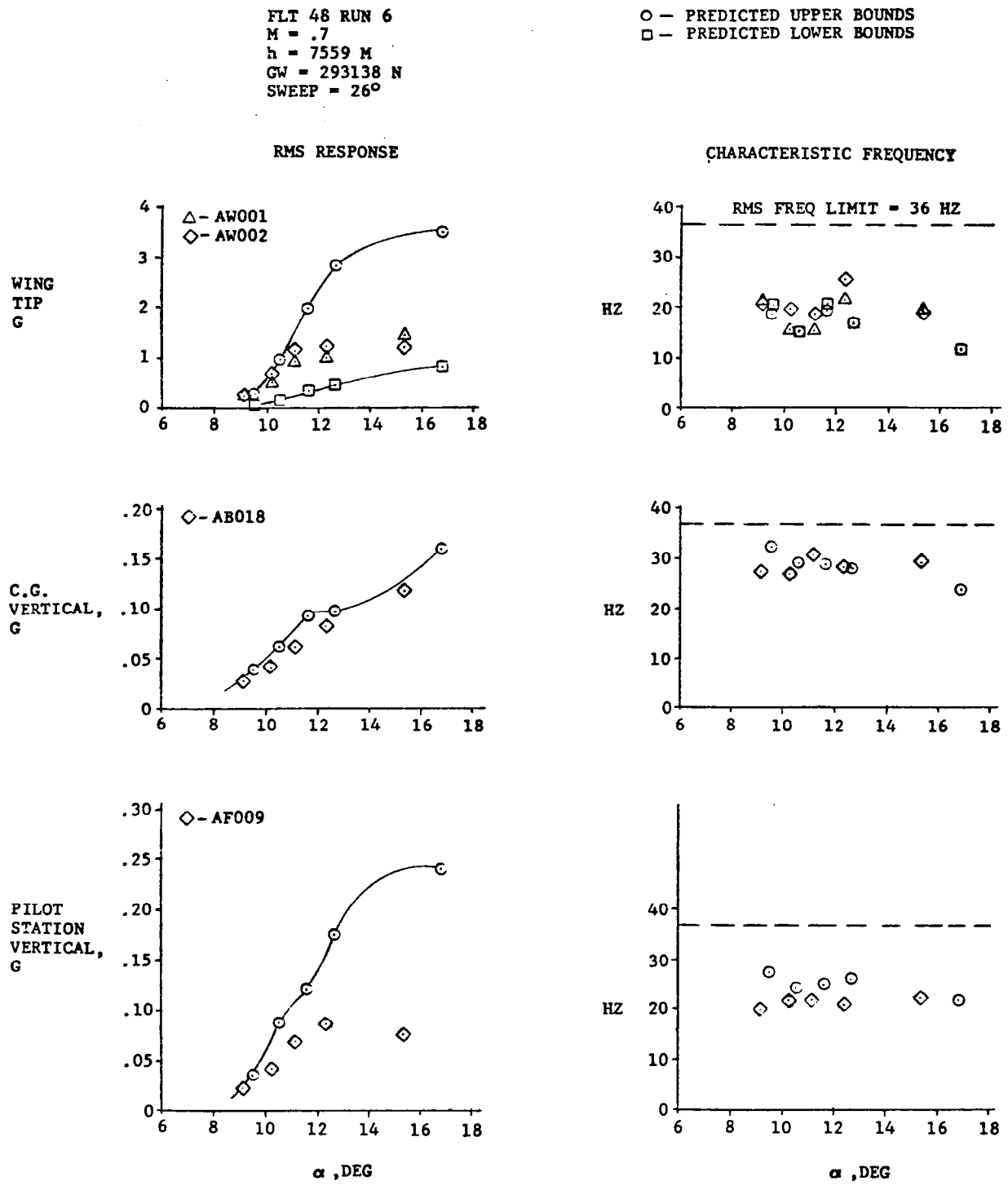

Figure 23.- Response predictions for case 3

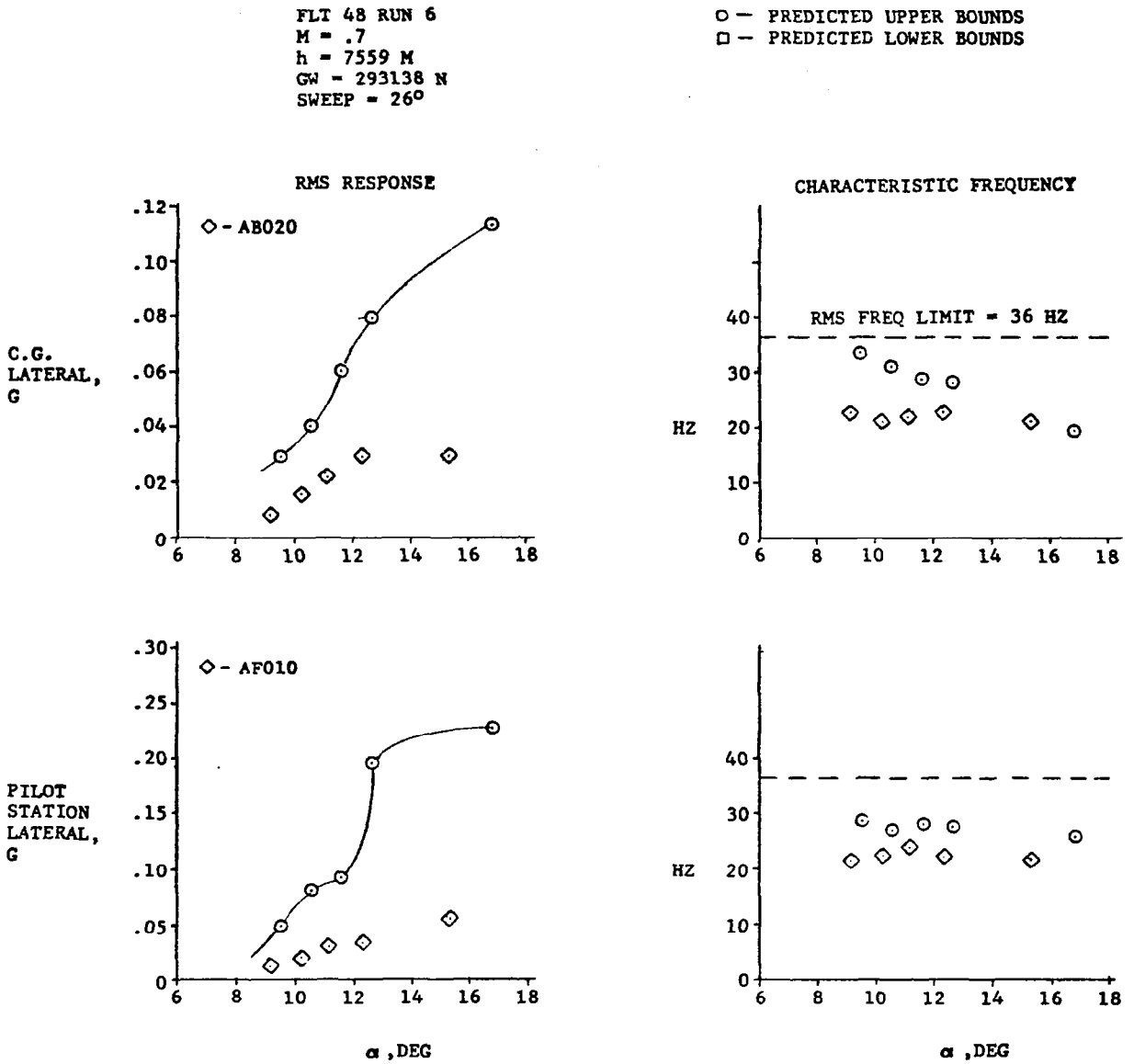

Figure 23.-(continued)

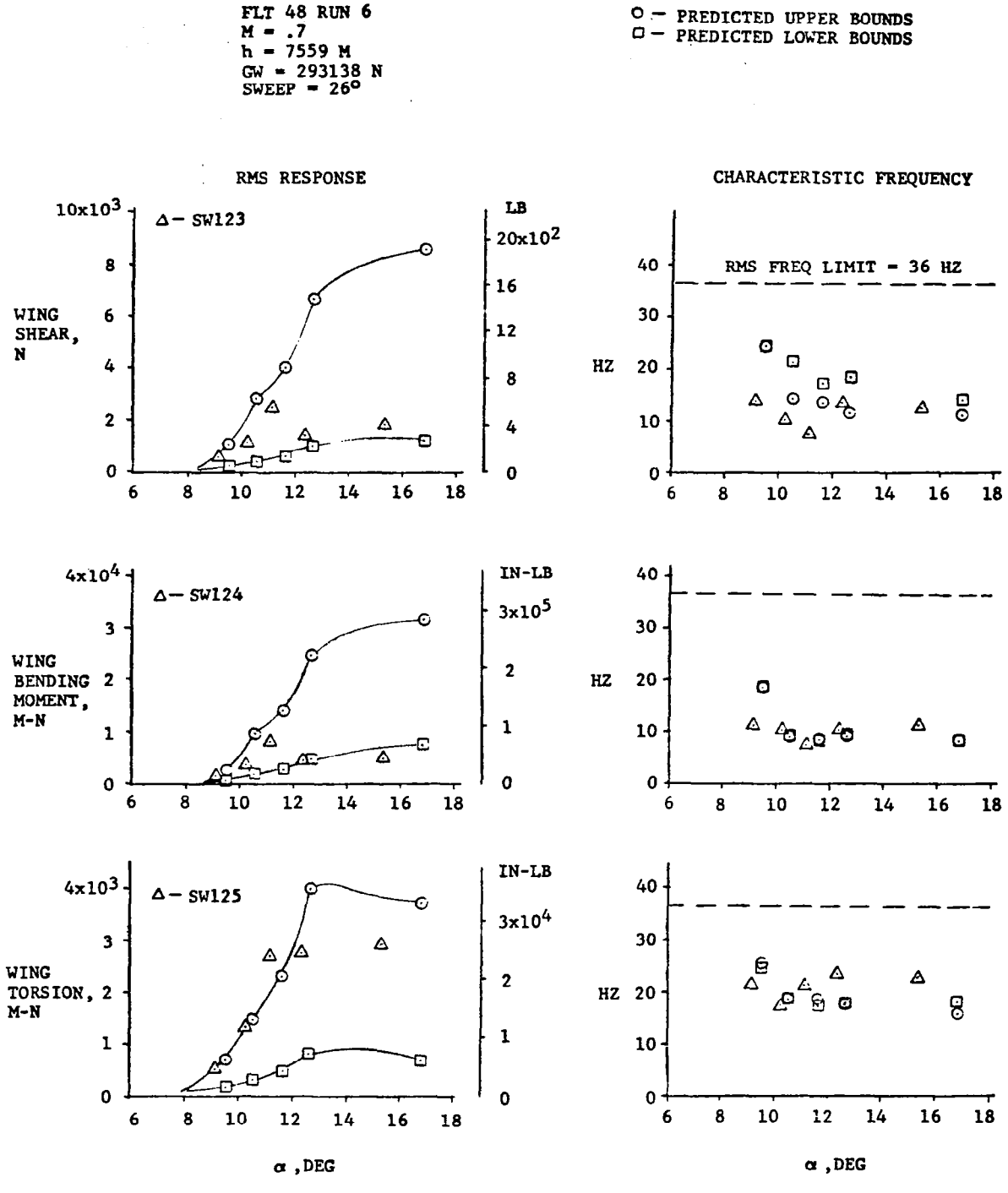

Figure 23.-(continued)

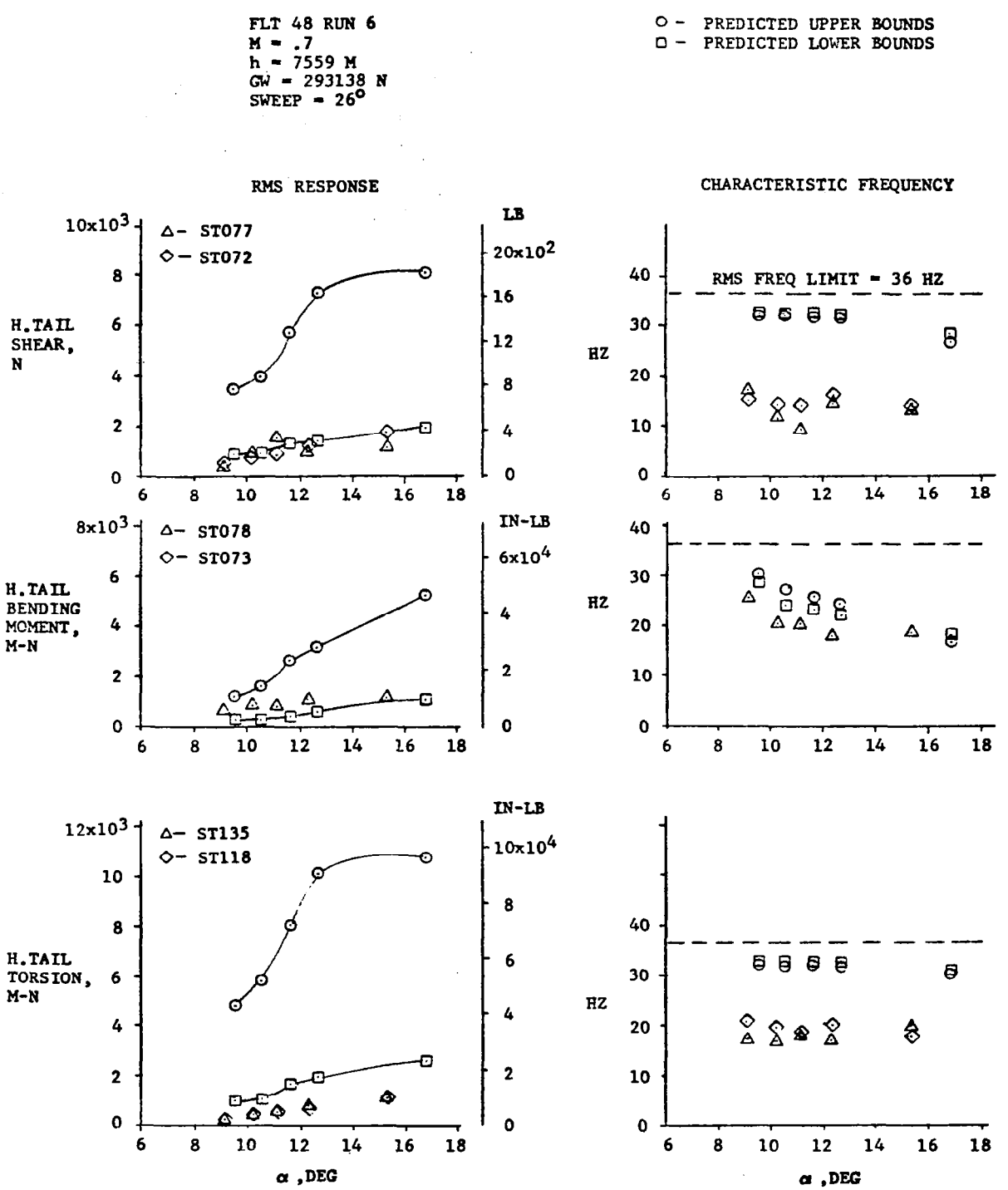

Figure 23.-(continued)

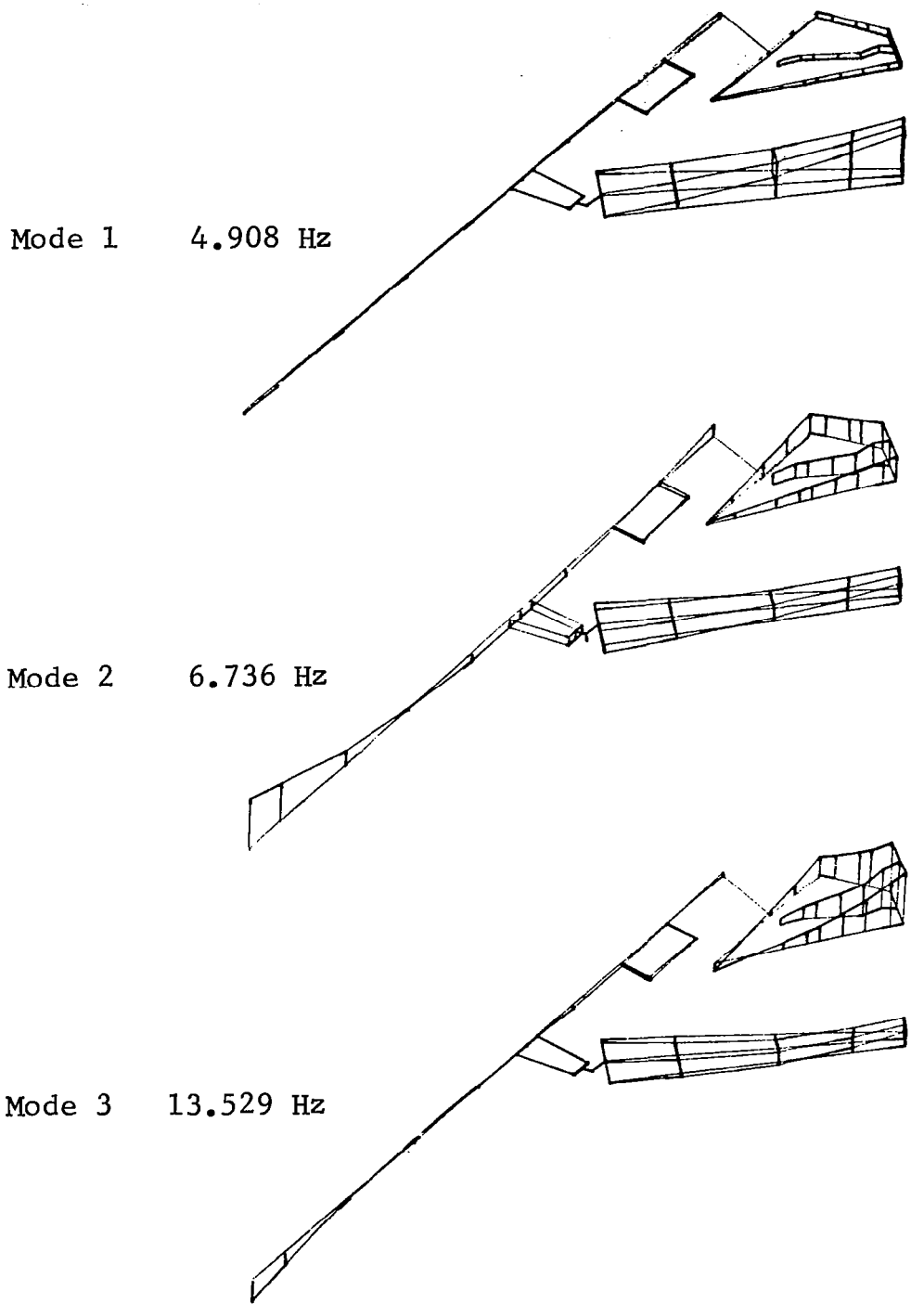

Figure 24.- Calculated symmetric natural modes for case 4, $\Lambda=50.0^{\circ}$ and G.W.=331,392N

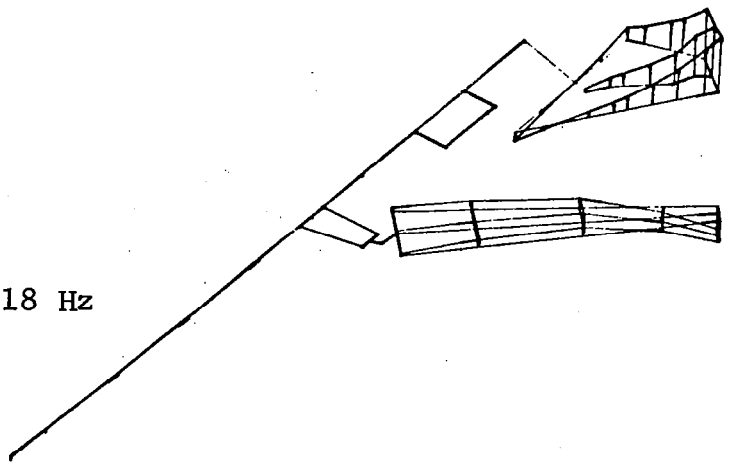

Mode 4 15.218 Hz

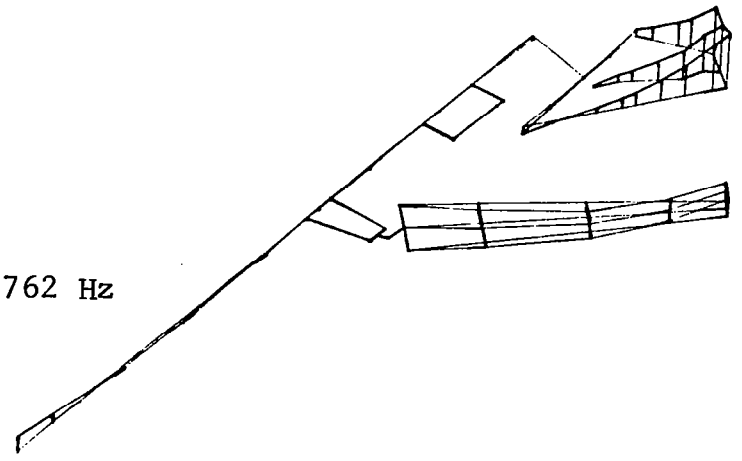

Mode 5 16.762 Hz

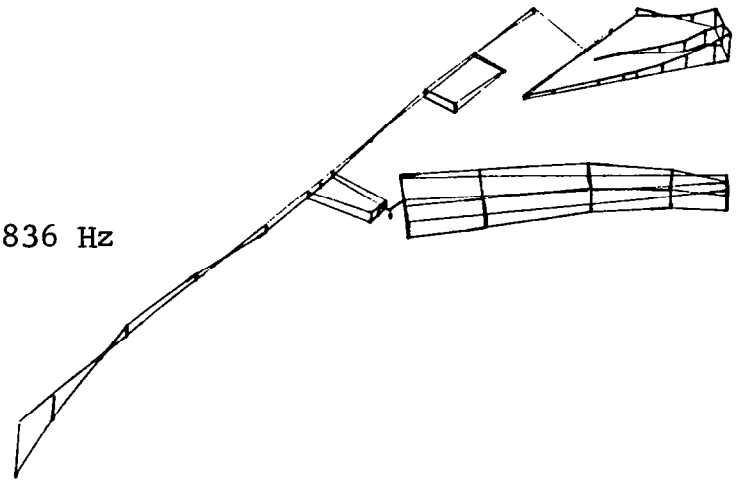

Mode 6 21.836 Hz

Figure 24.-(continued)

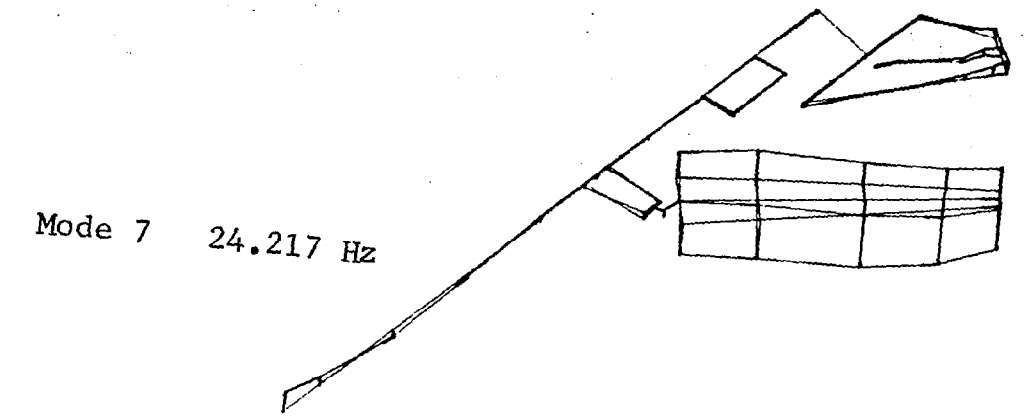

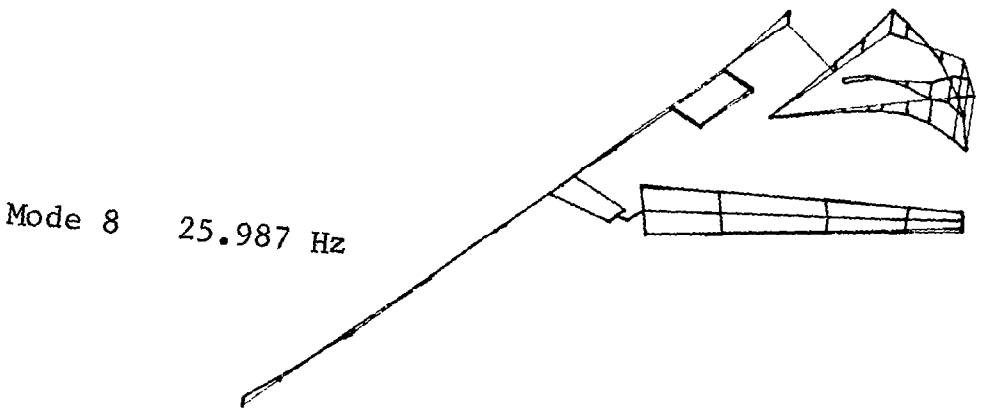

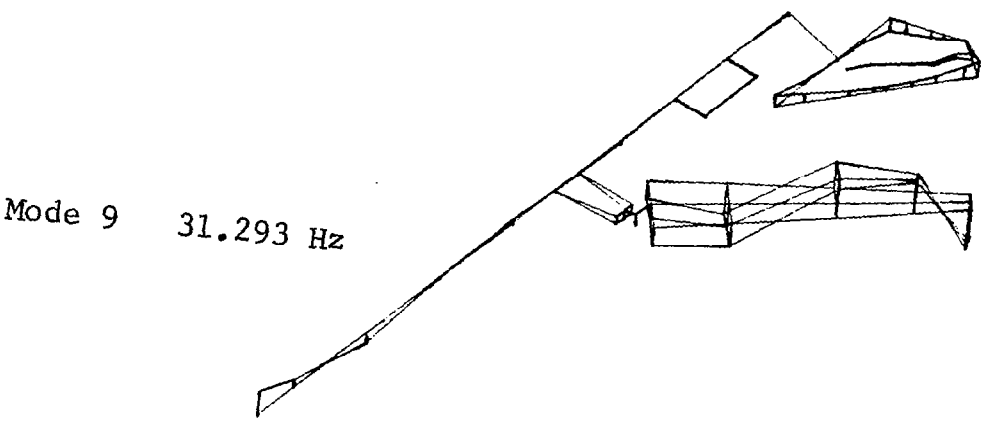

Figure 24.-(continued)

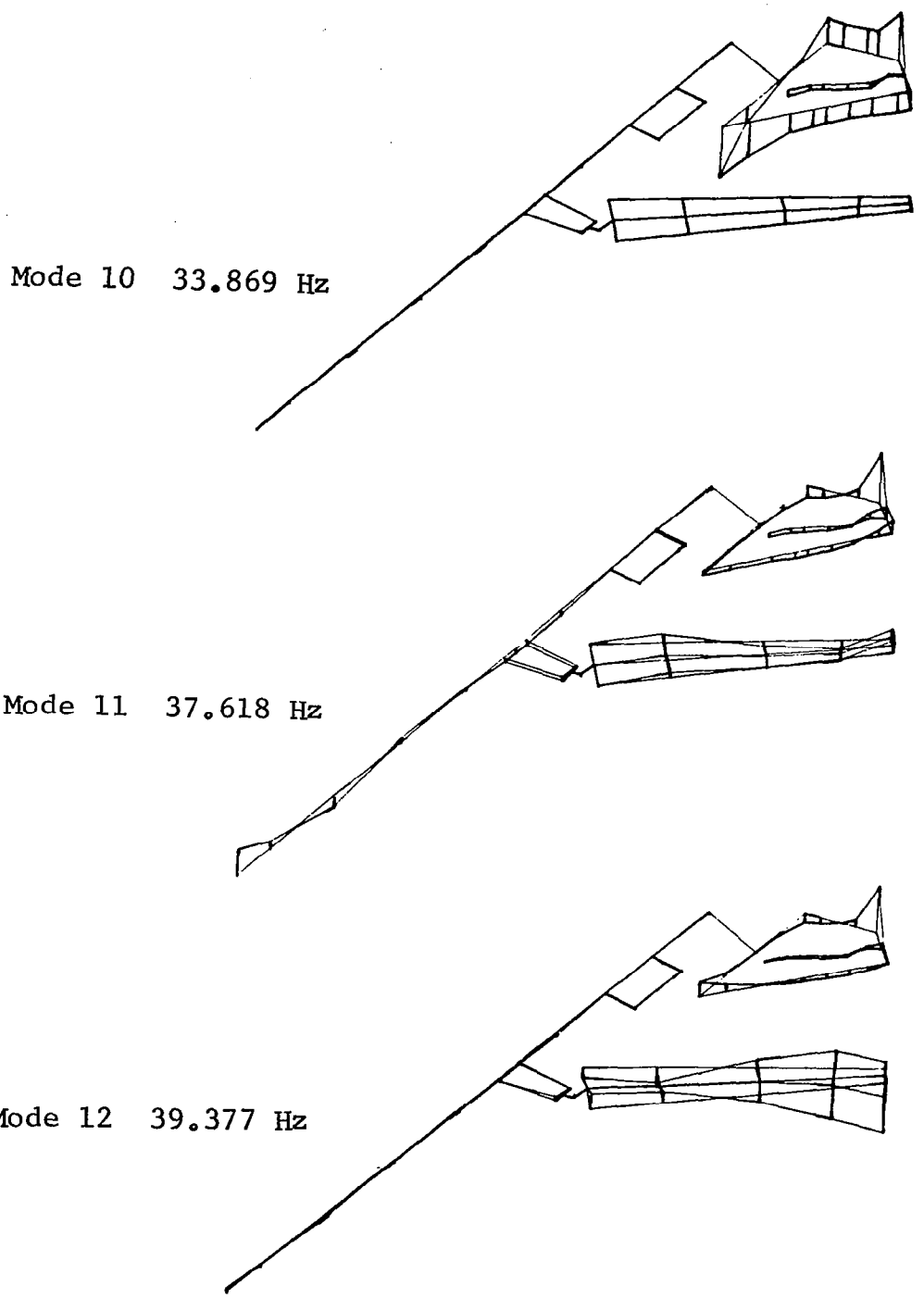

Figure 24.-(continued)

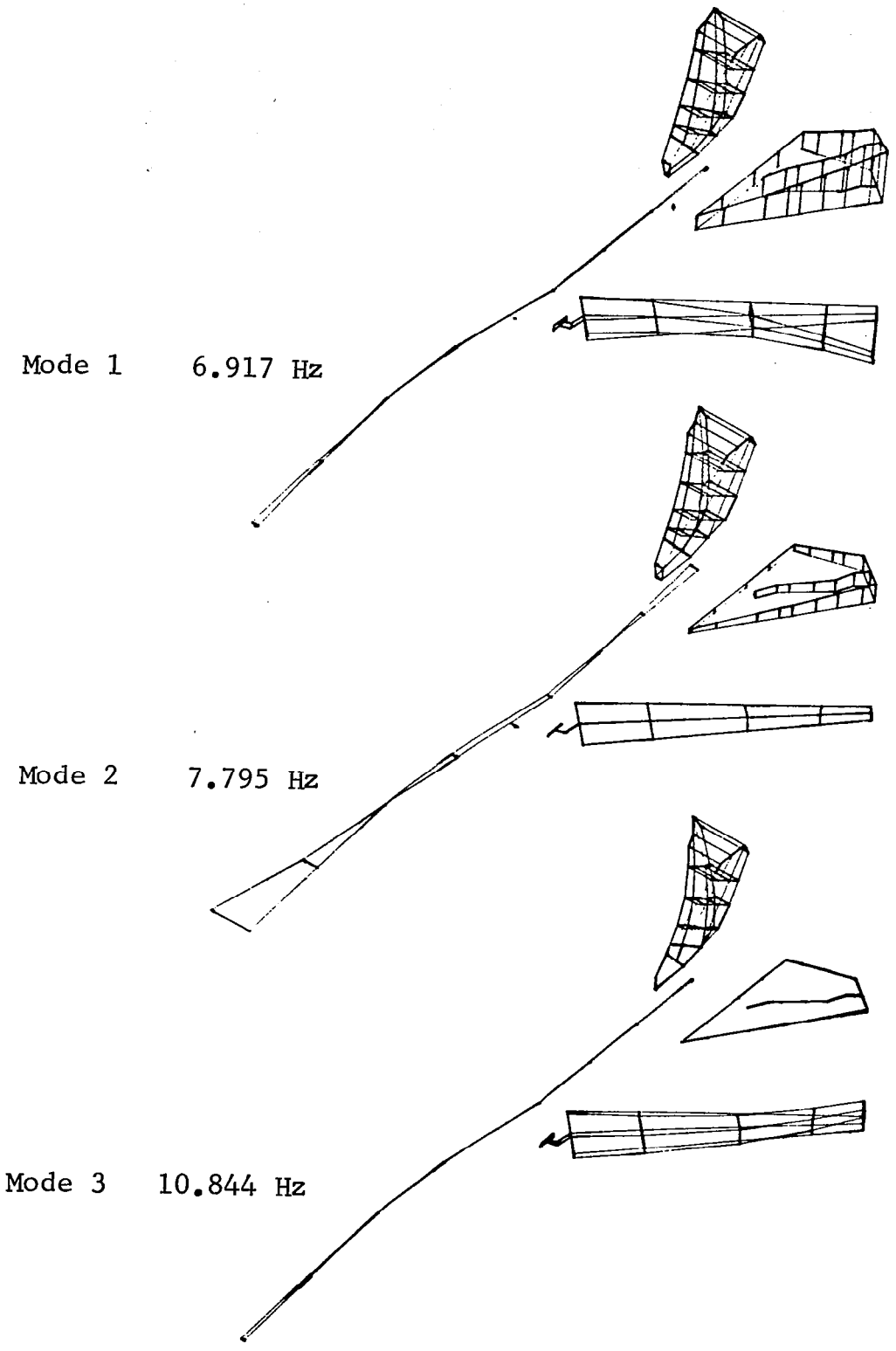

Figure 25.- Calculated antisymmetric natural modes for case 4, $\Lambda=50.0^{\circ}$ and G.W.=331,392N

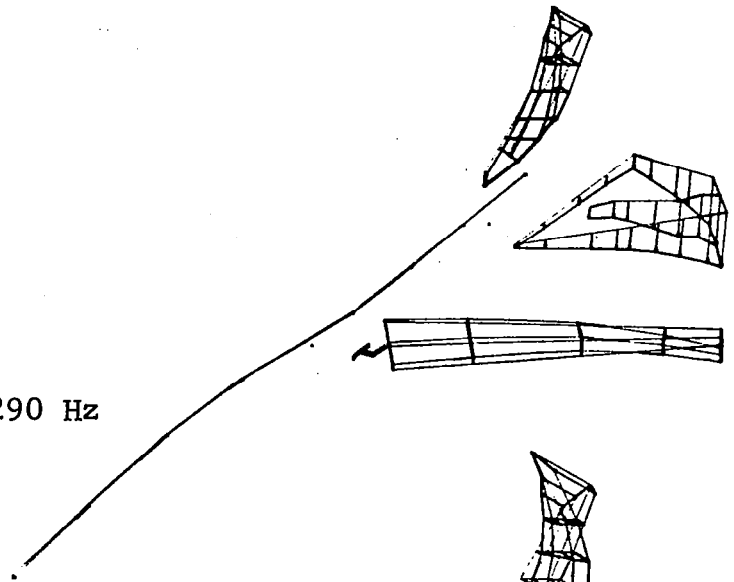

Mode 4 12.290 Hz

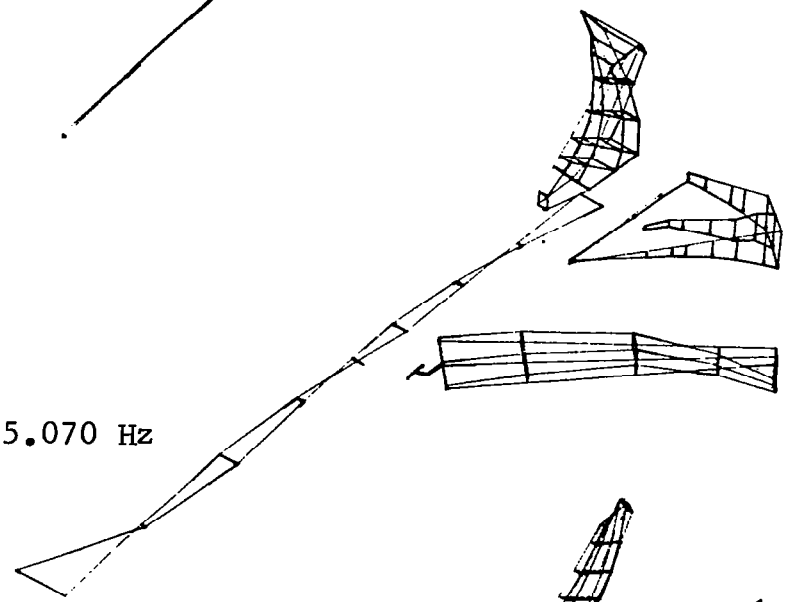

Mode 5 15.070 Hz

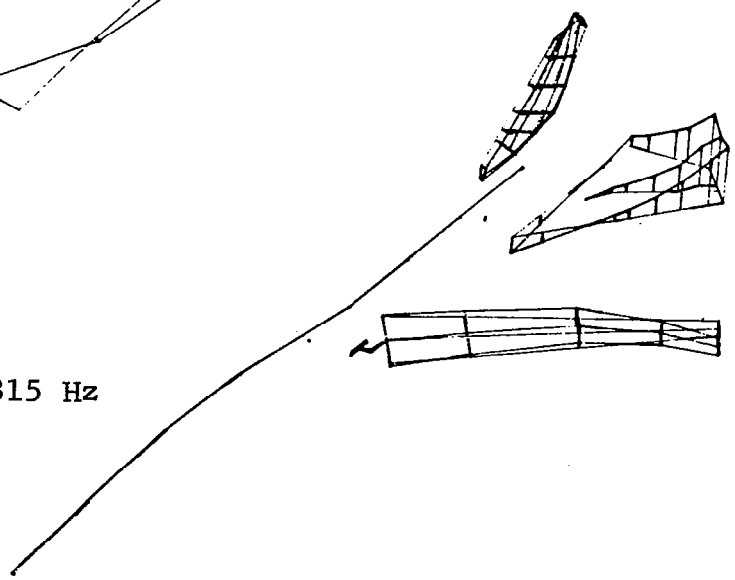

Mode 6 17.815 Hz

Figure 25.-(continued)

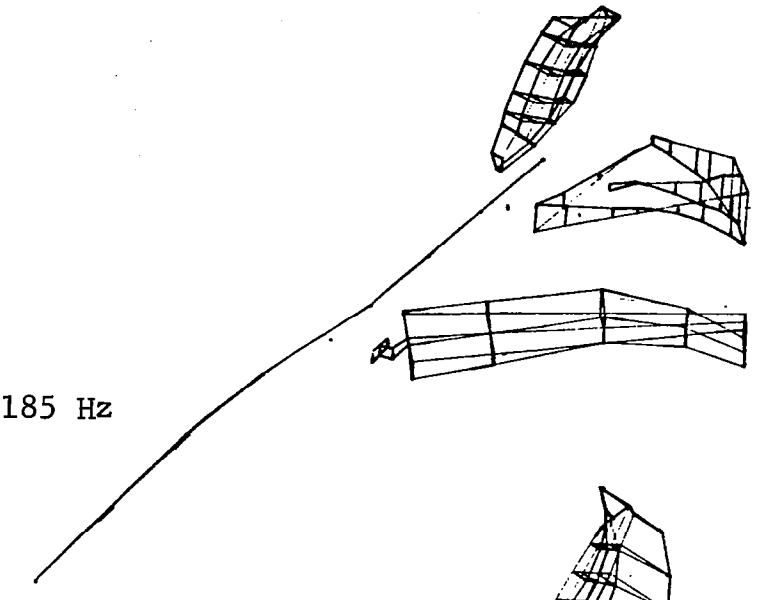

Mode 7 21.185 Hz

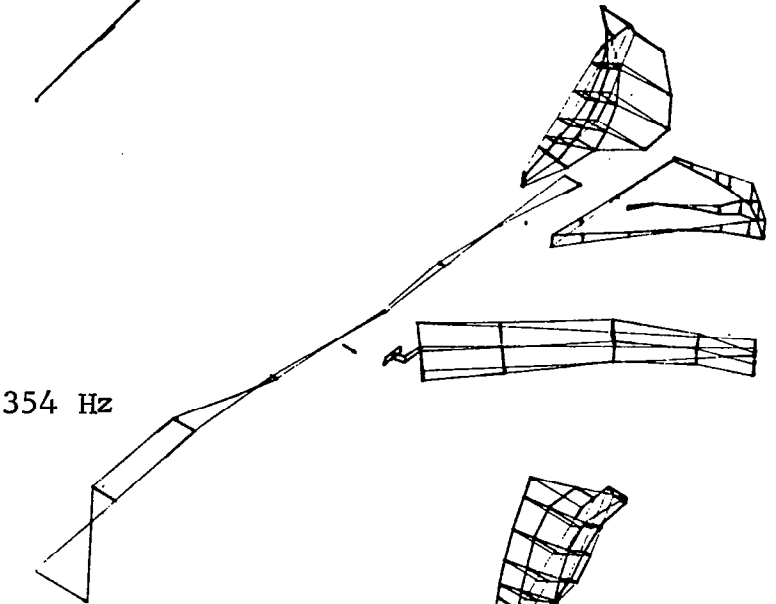

Mode 8 22.354 Hz

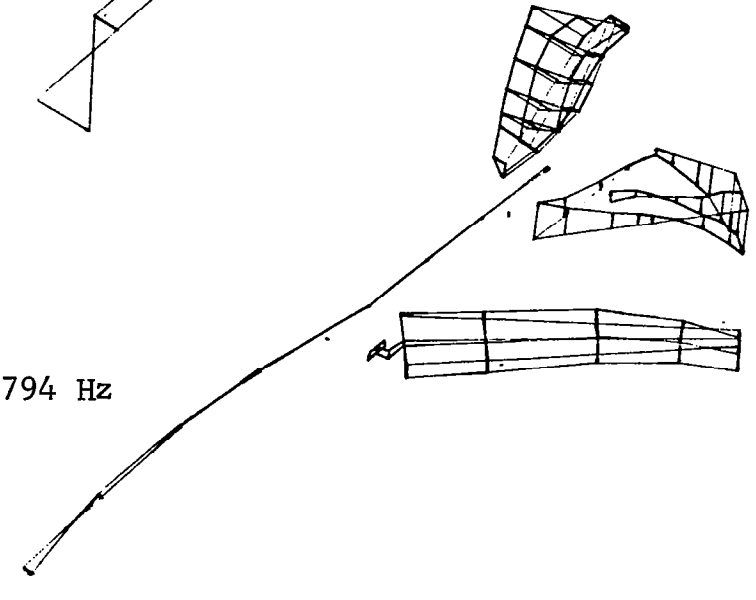

Mode 9 23.794 Hz

Figure 25.-(continued)

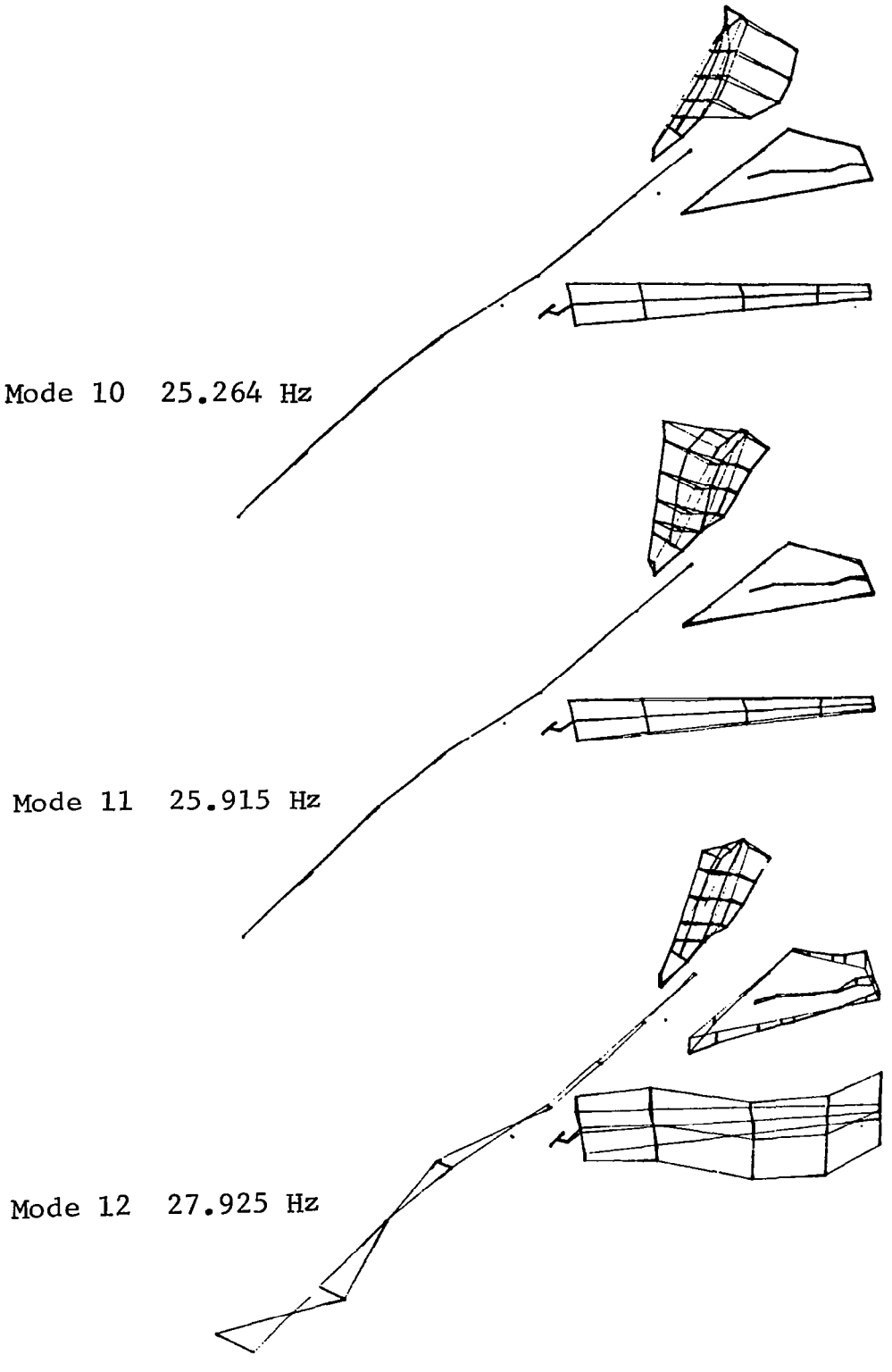

Figure 25.-(continued)

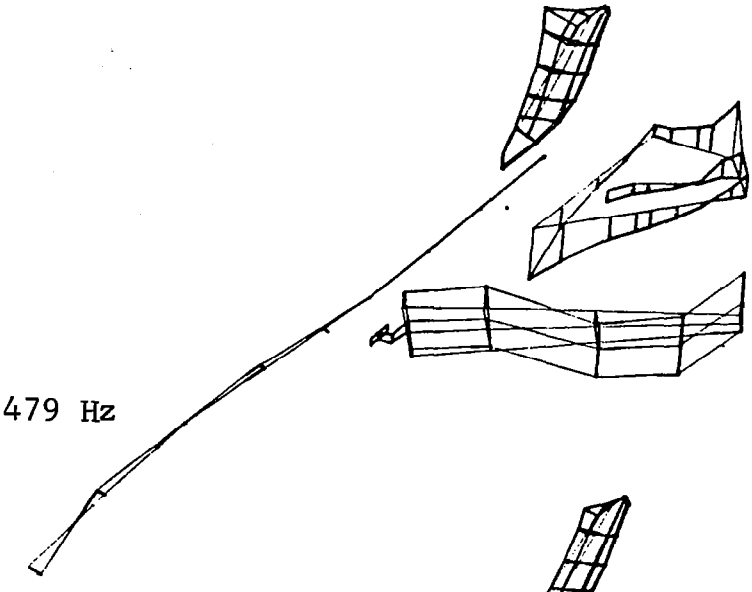

Mode 13 29.479 Hz

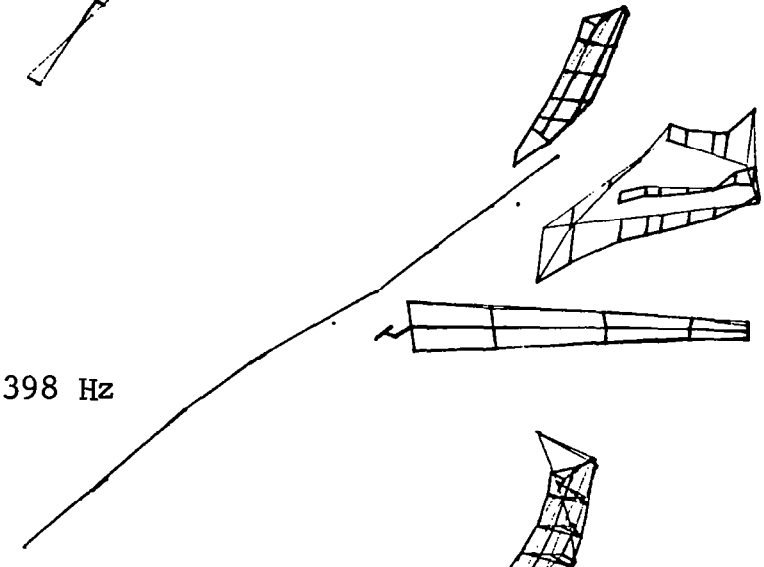

Mode 14 31.398 Hz

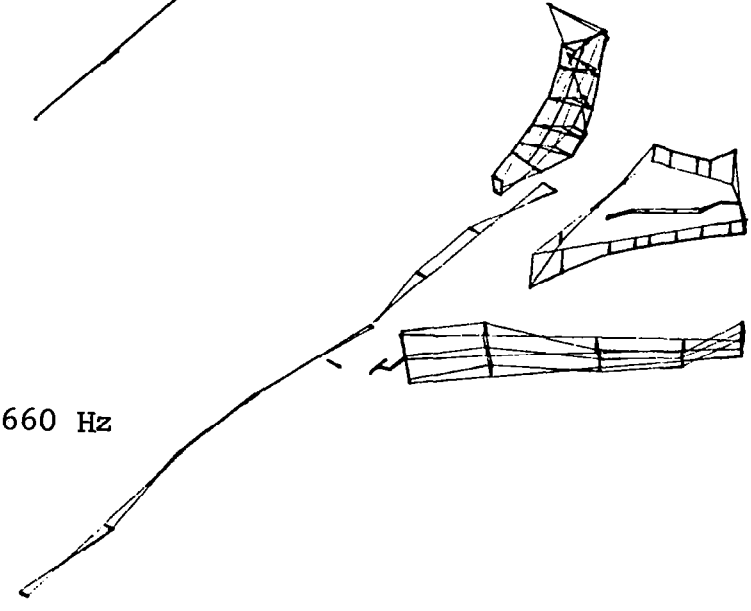

Mode 15 34.660 Hz

Figure 25.-(continued)

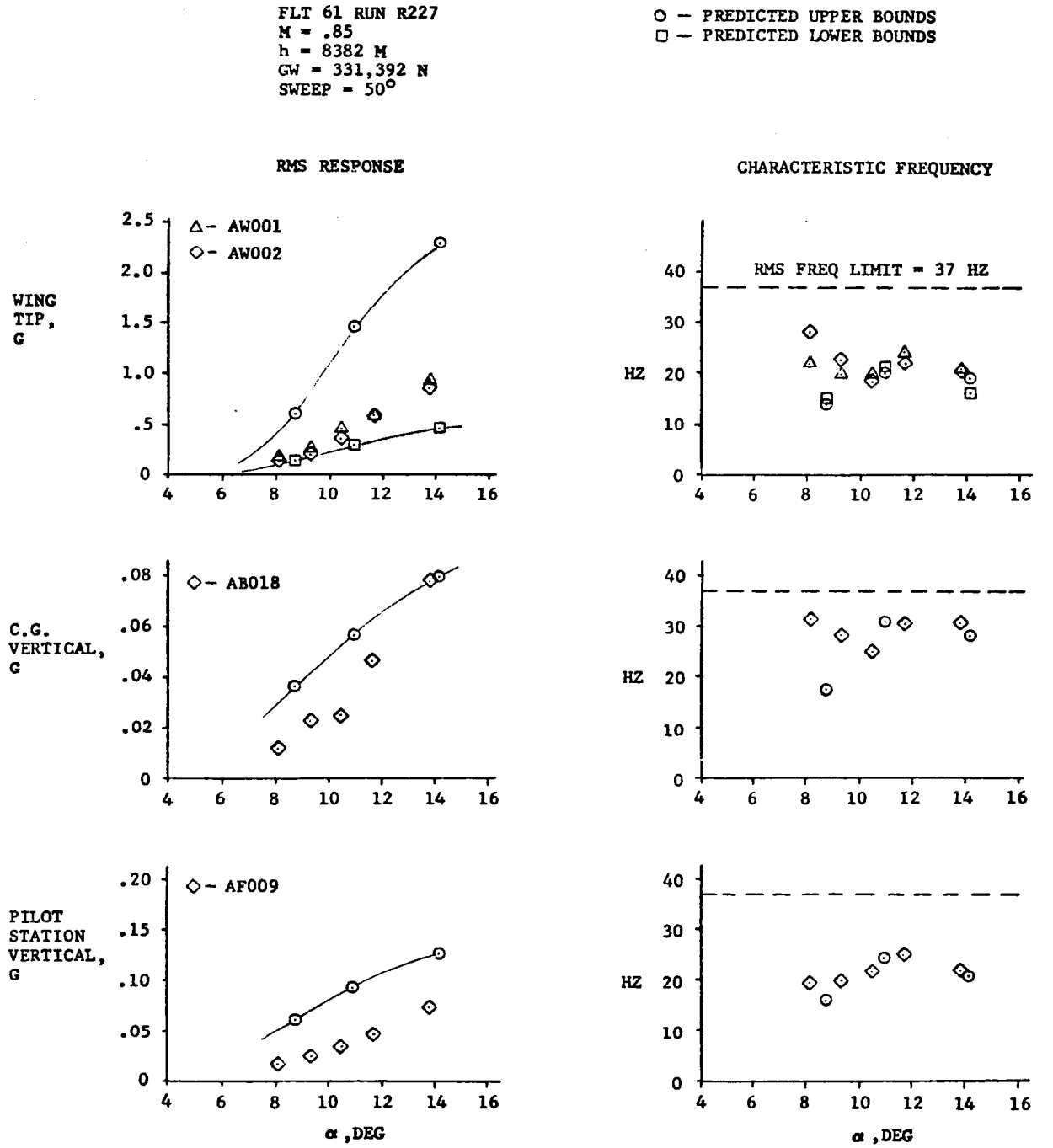

Figure 26.- Response predictions for case 4

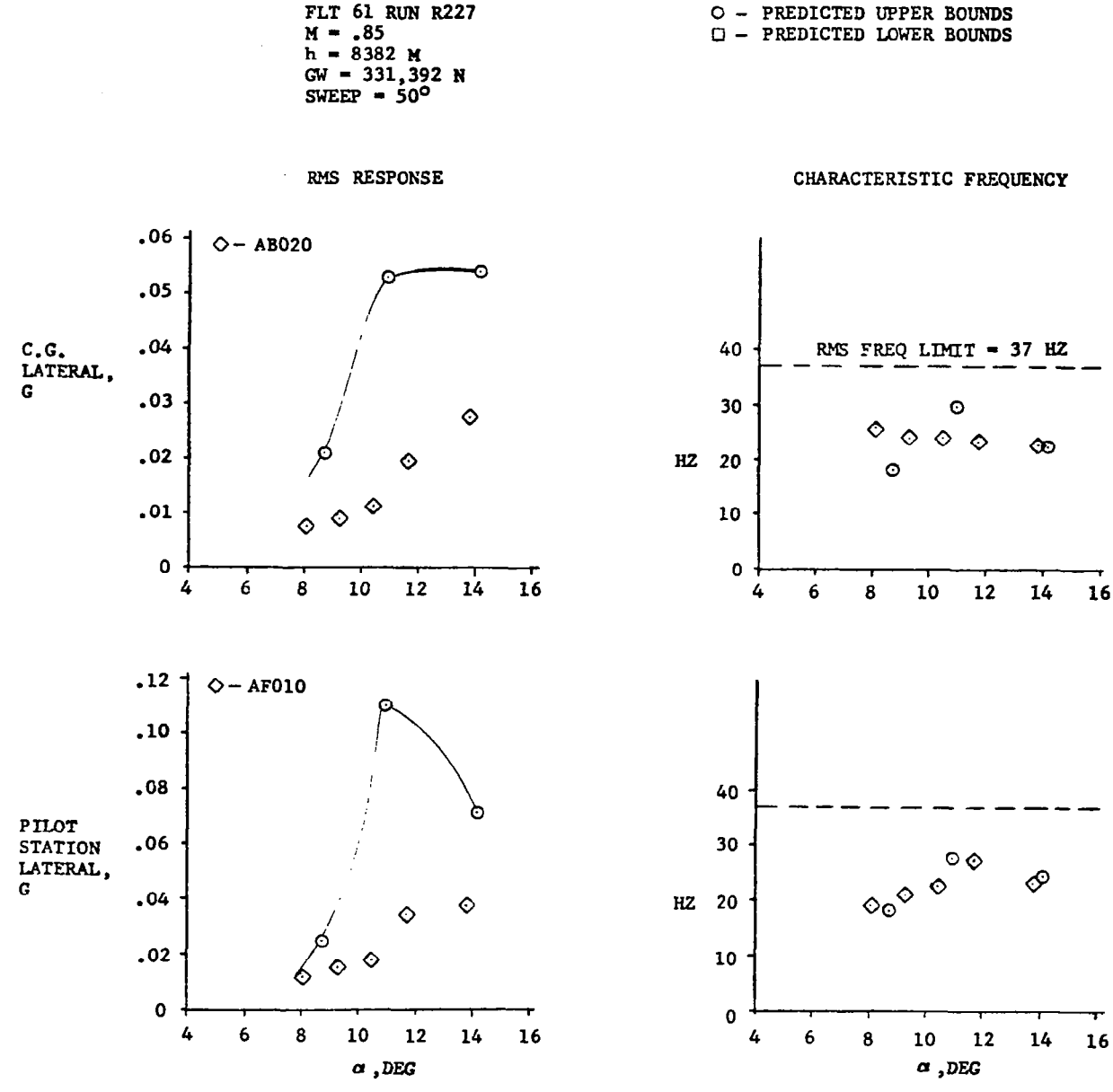

Figure 26.-(continued)

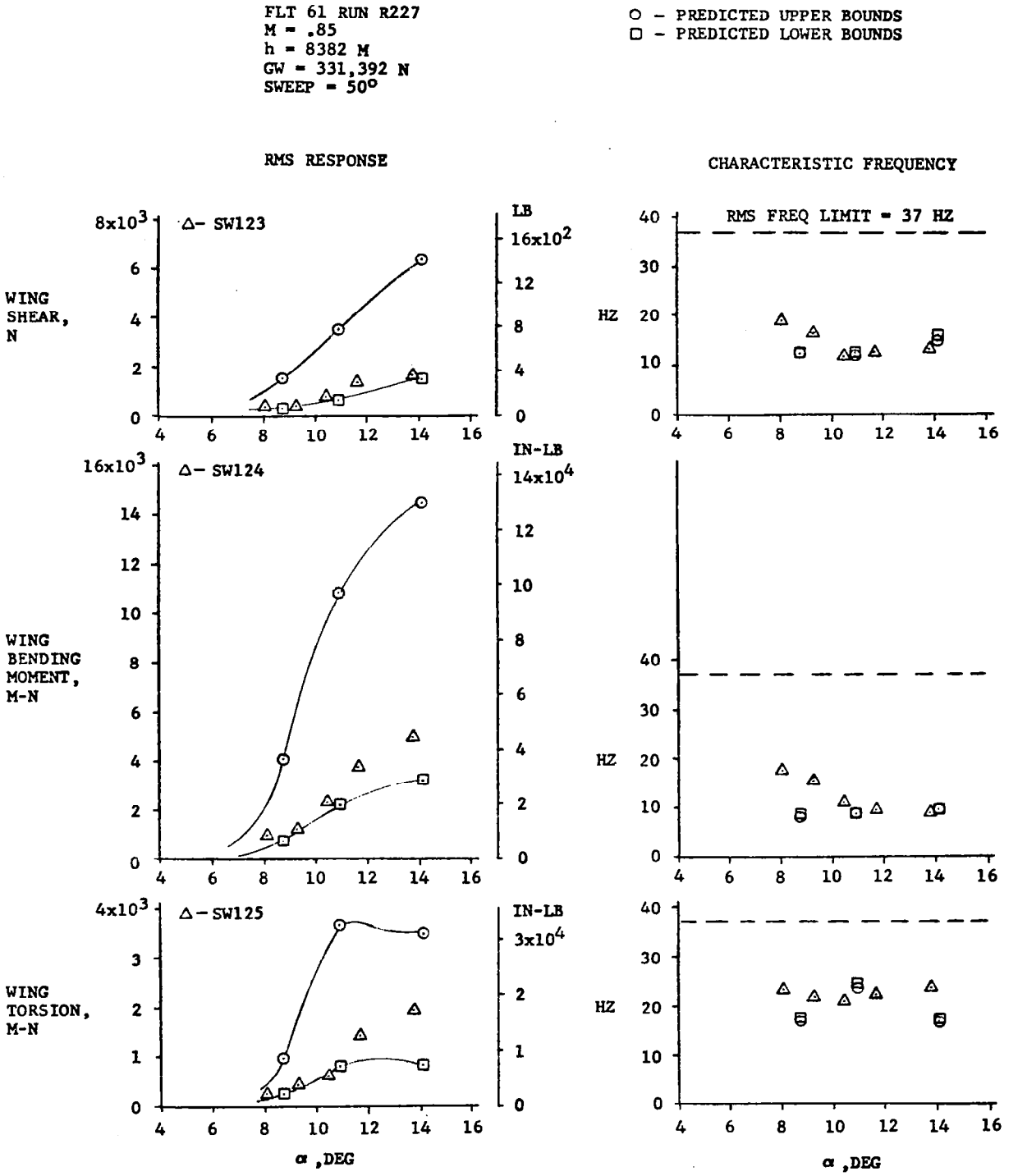

Figure 26.-(continued)

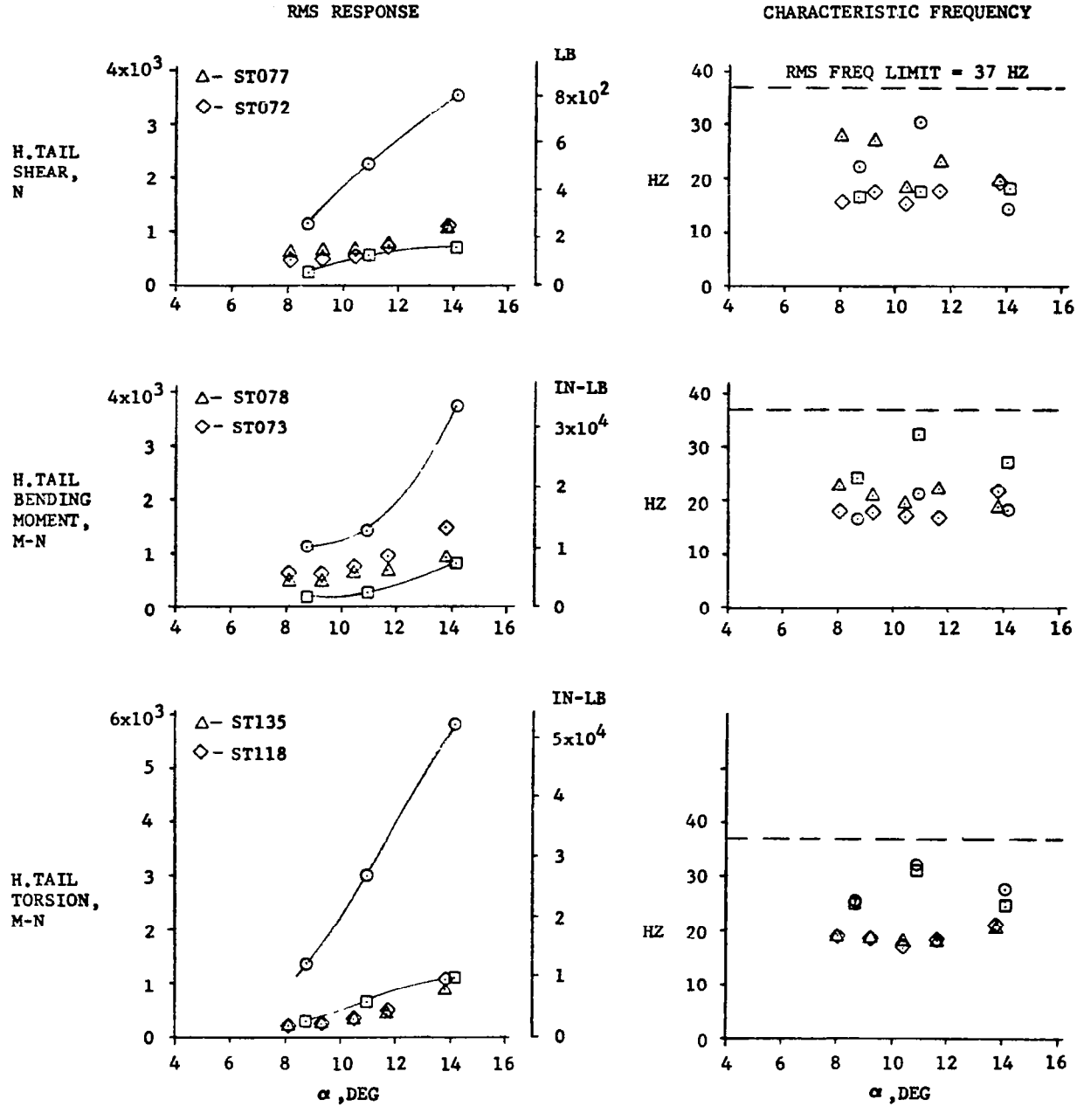

Figure 26.-(continued)

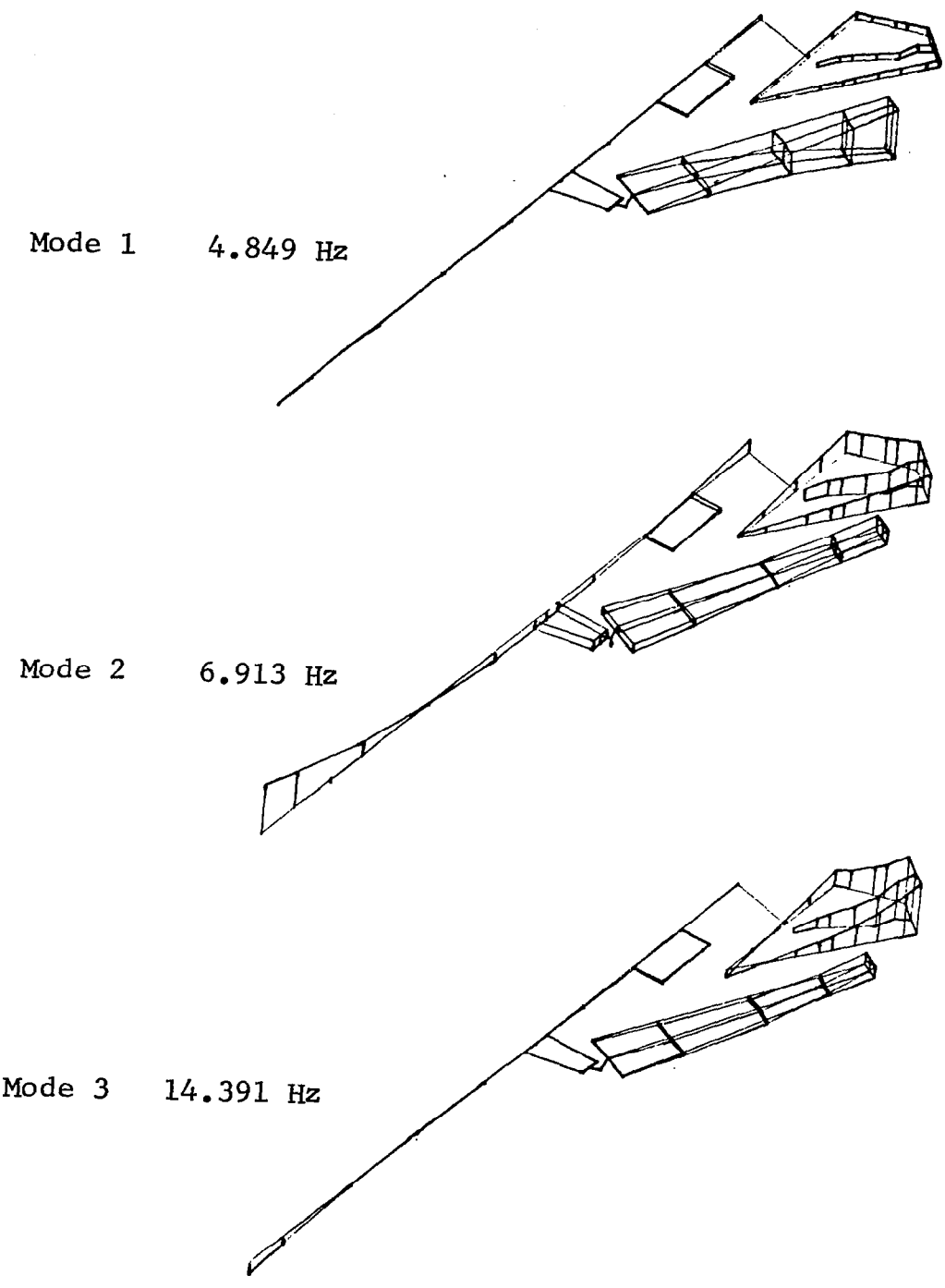

Figure 27.- Calculated symmetric natural modes for cases 5 and 7, $\Lambda=72.5^{o}$ and G.W.=268,673N

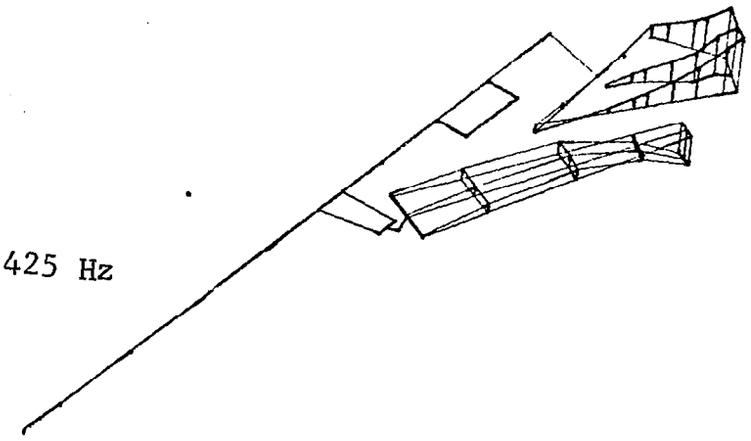

Mode 4 15.425 Hz

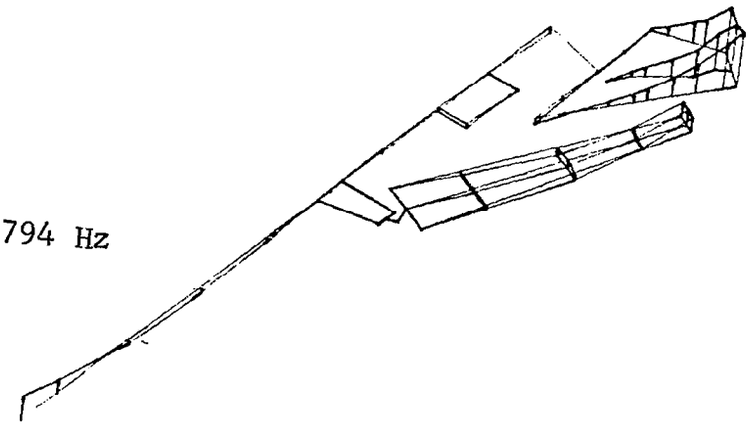

Mode 5 17.794 Hz

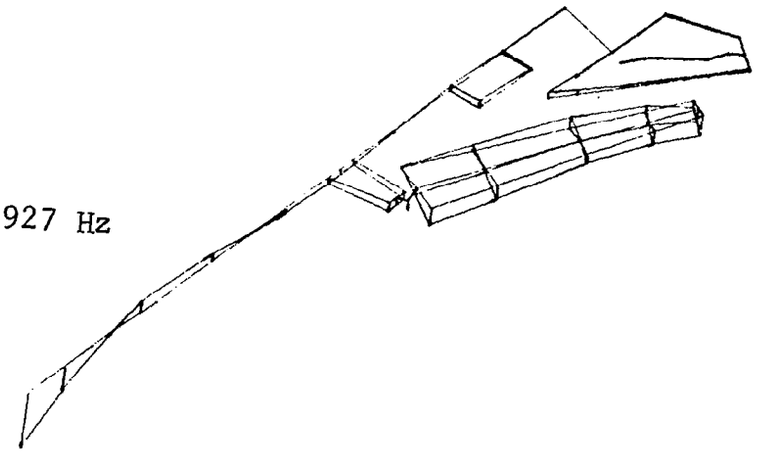

Mode 6 22.927 Hz

Figure 27.-(continued)

Mode 7 24.571 Hz

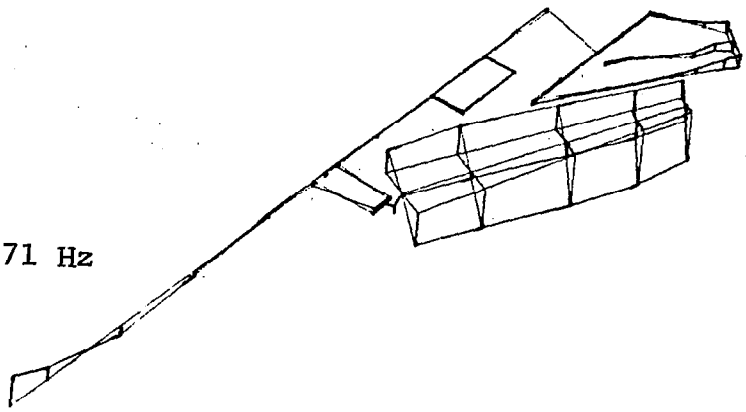

Mode 8 27.448 Hz

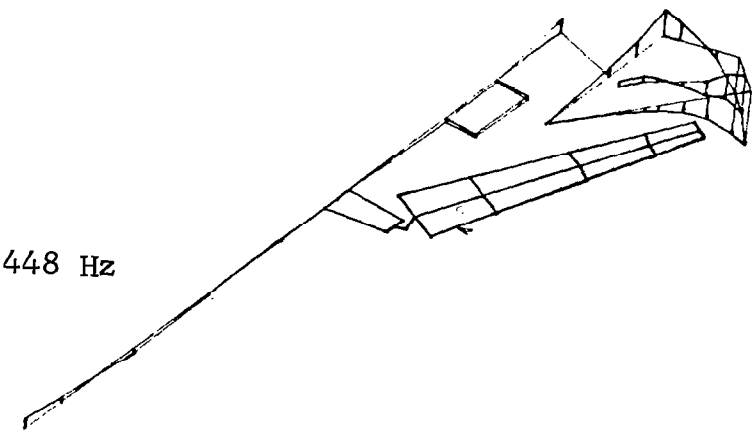

Mode 9 31.927 Hz

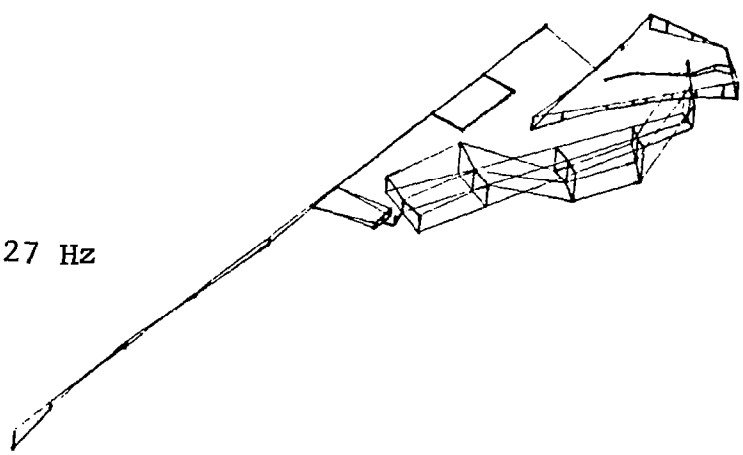

Figure 27.-(continued)

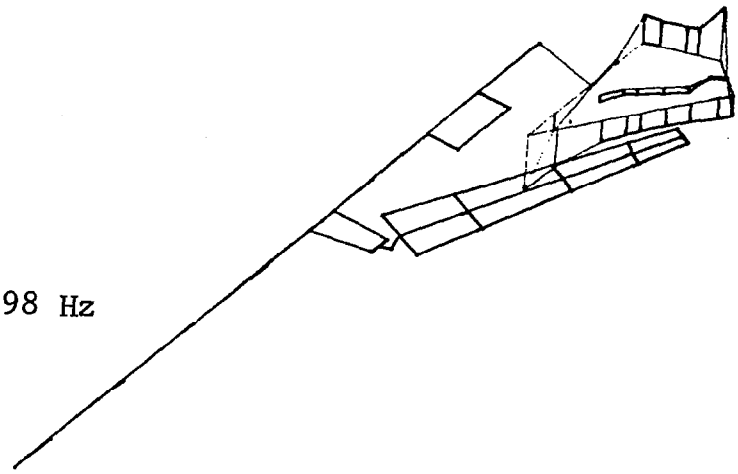

Mode 10 33.898 Hz

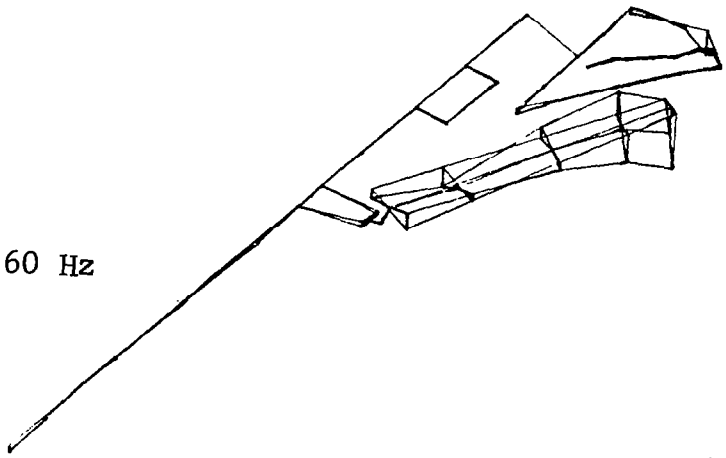

Mode 11 39.260 Hz

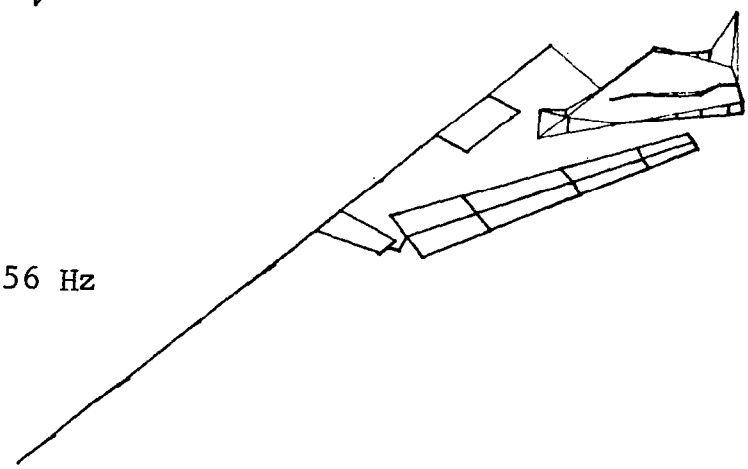

Mode 12 39.856 Hz

Figure 27.-(continued)

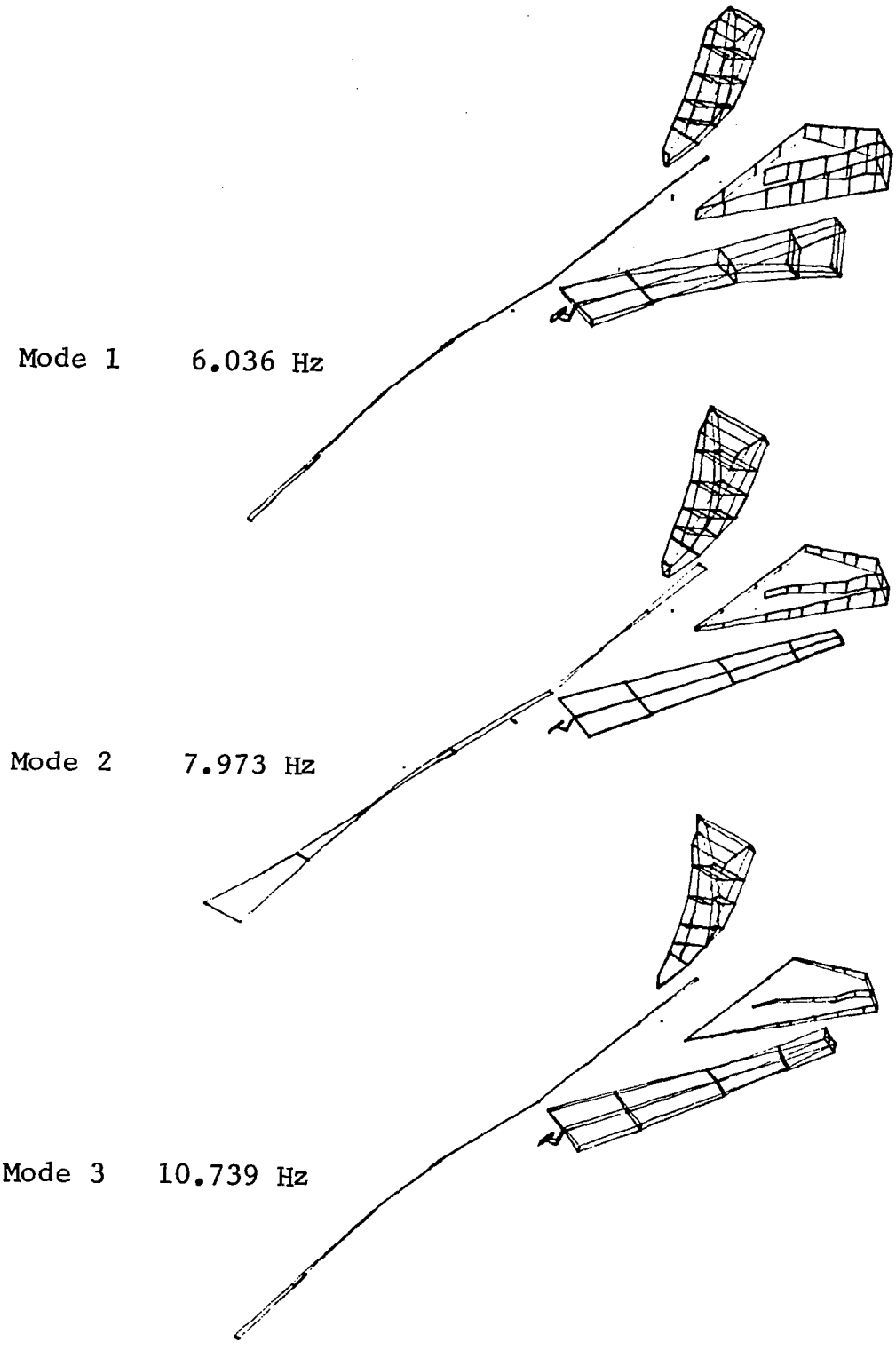

Figure 28.- Calculated antisymmetric natural modes for cases 5 and 7, $\Lambda=72.5^{o}$ and G.W.=268,673N

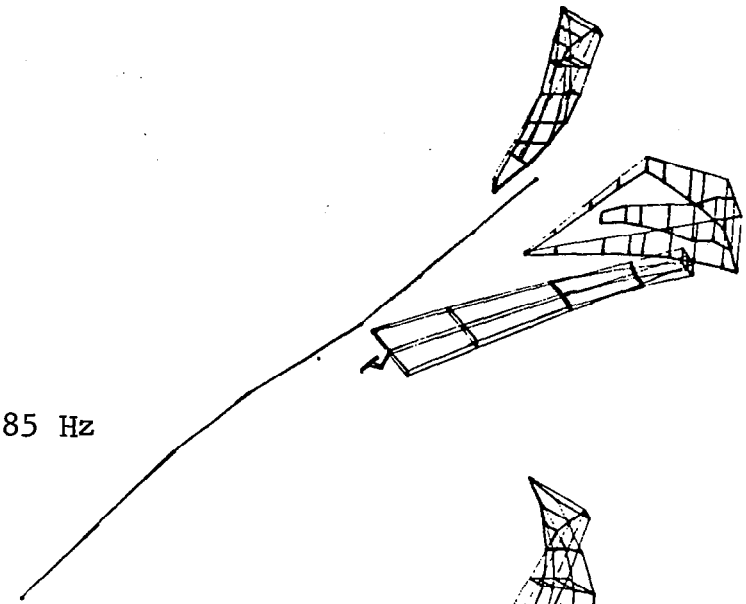

Mode 4 12.385 Hz

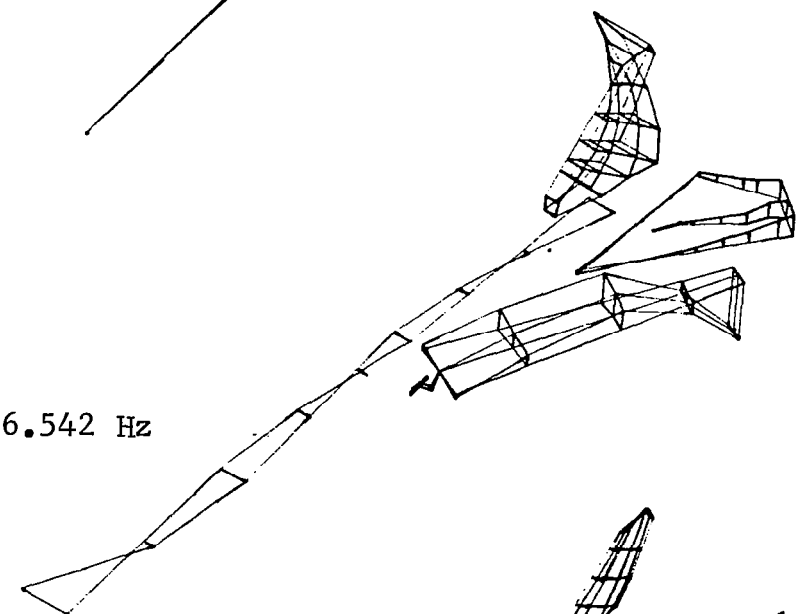

Mode 5 16.542 Hz

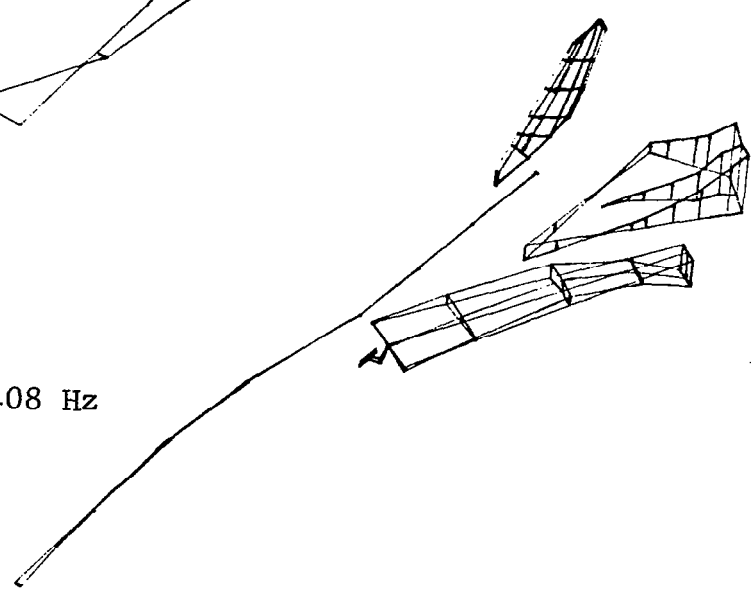

Mode 6 17.408 Hz

Figure 28.-(continued)

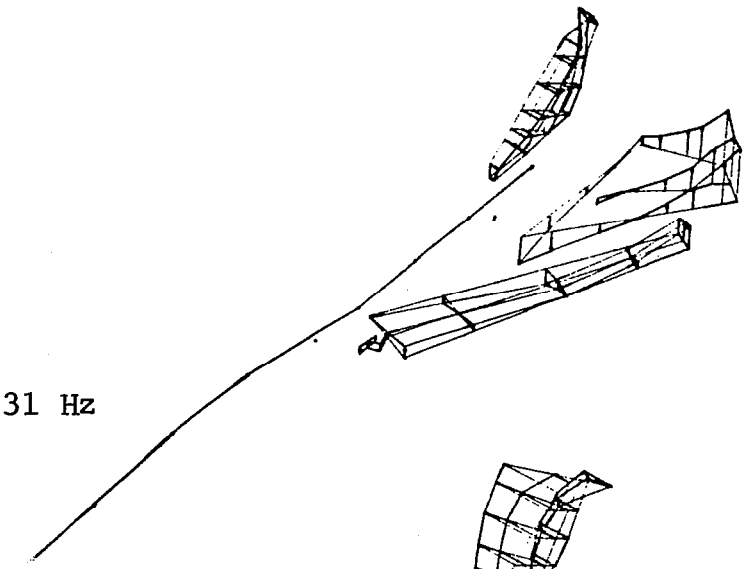

Mode 7 20.631 Hz

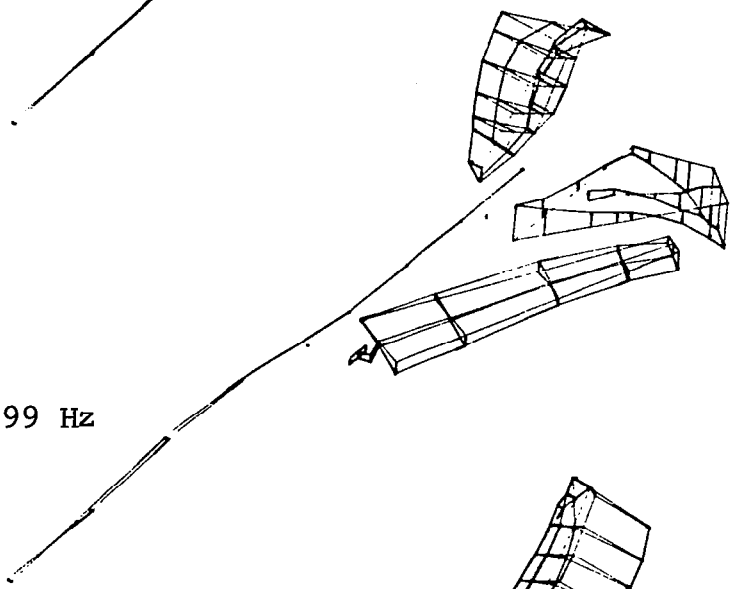

Mode 8 23.599 Hz

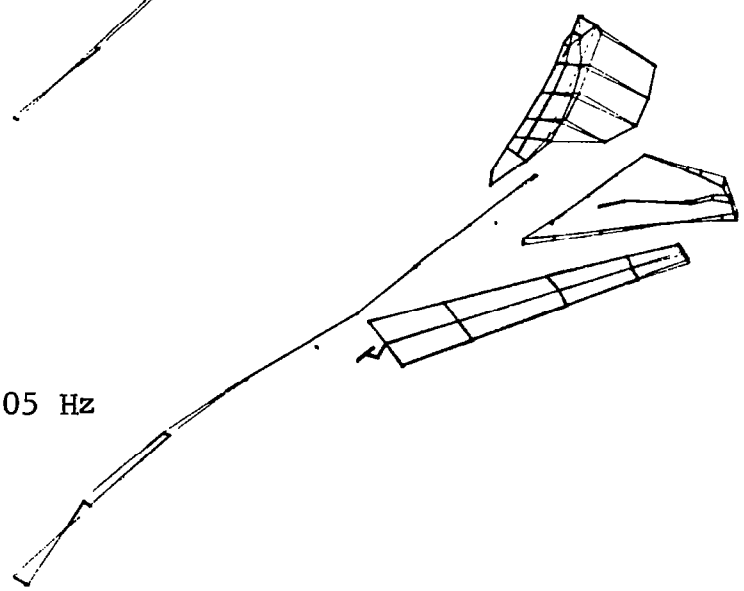

Mode 9 24.805 Hz

Figure 28.-(continued)

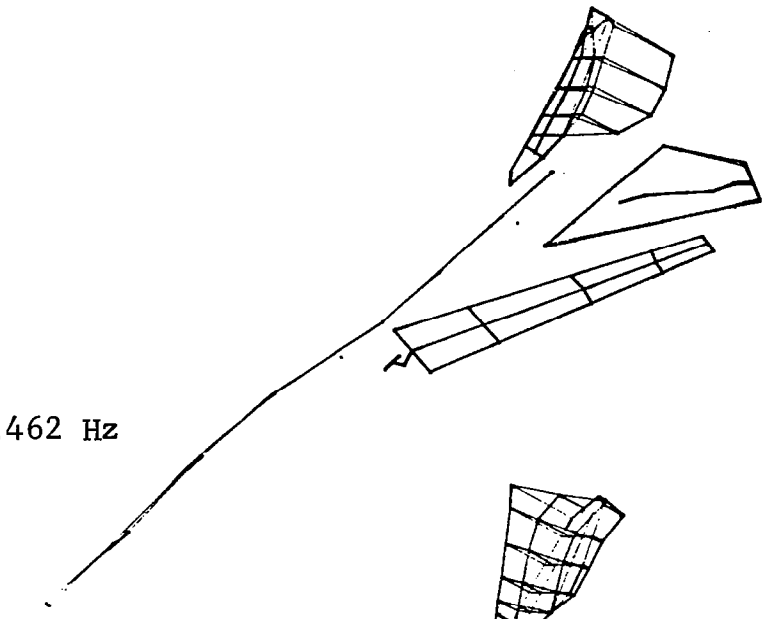

Mode 10 25.462 Hz

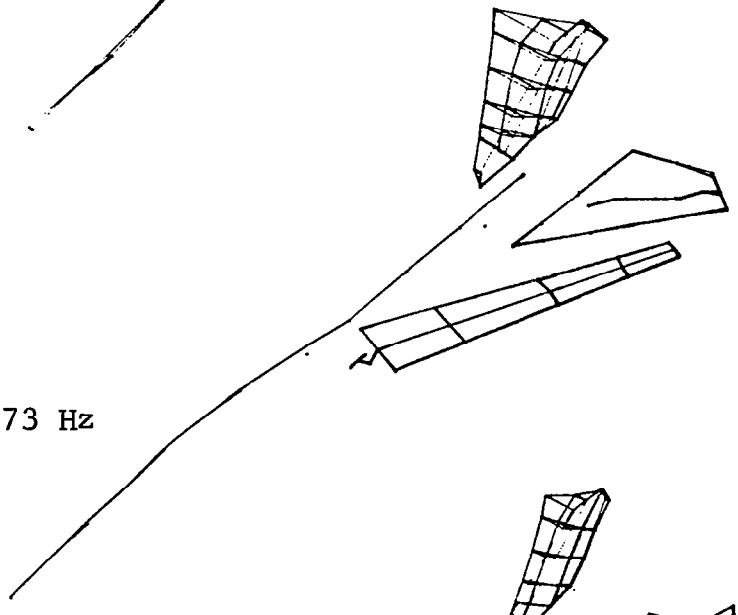

Mode 11 25.973 Hz

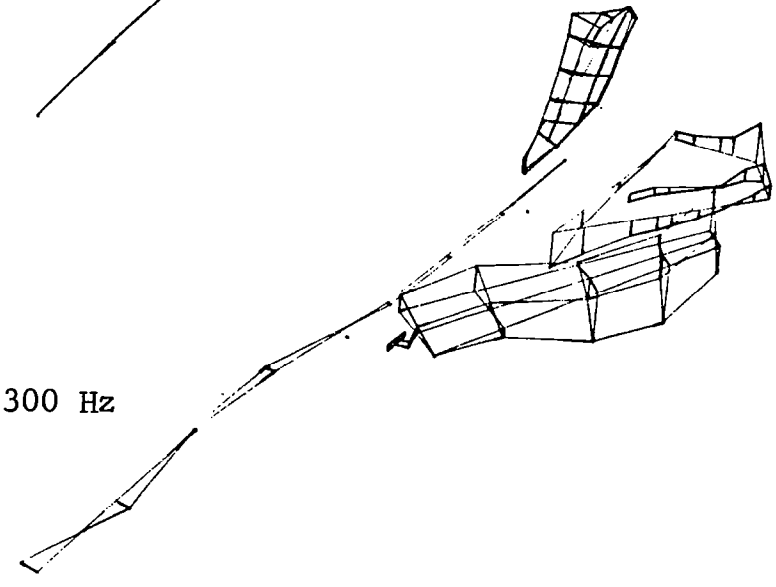

Mode 12 29.300 Hz

Figure 28.-(continued)

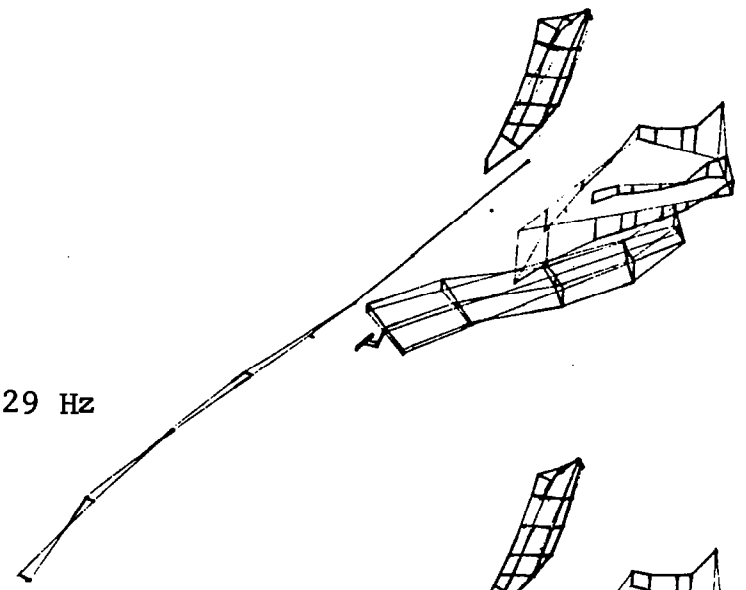

Mode 13 30.429 Hz

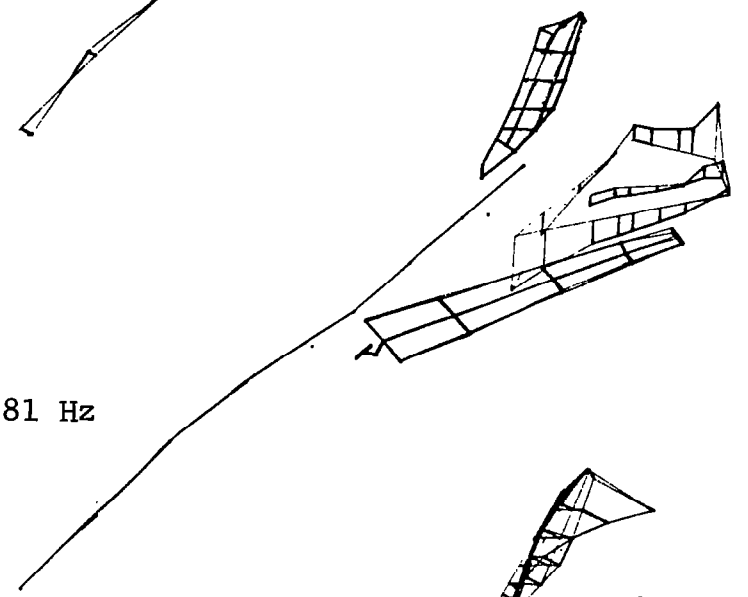

Mode 14 31.581 Hz

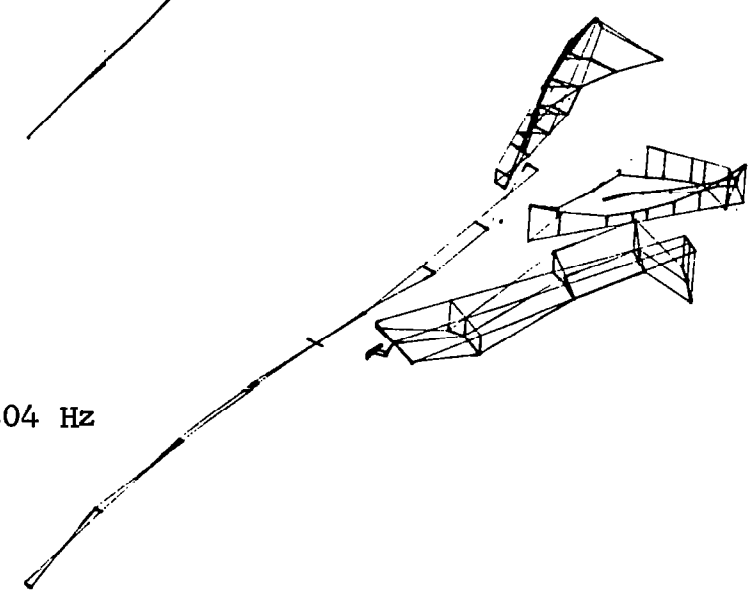

Mode 15 36.404 Hz

Figure 28.-(continued)

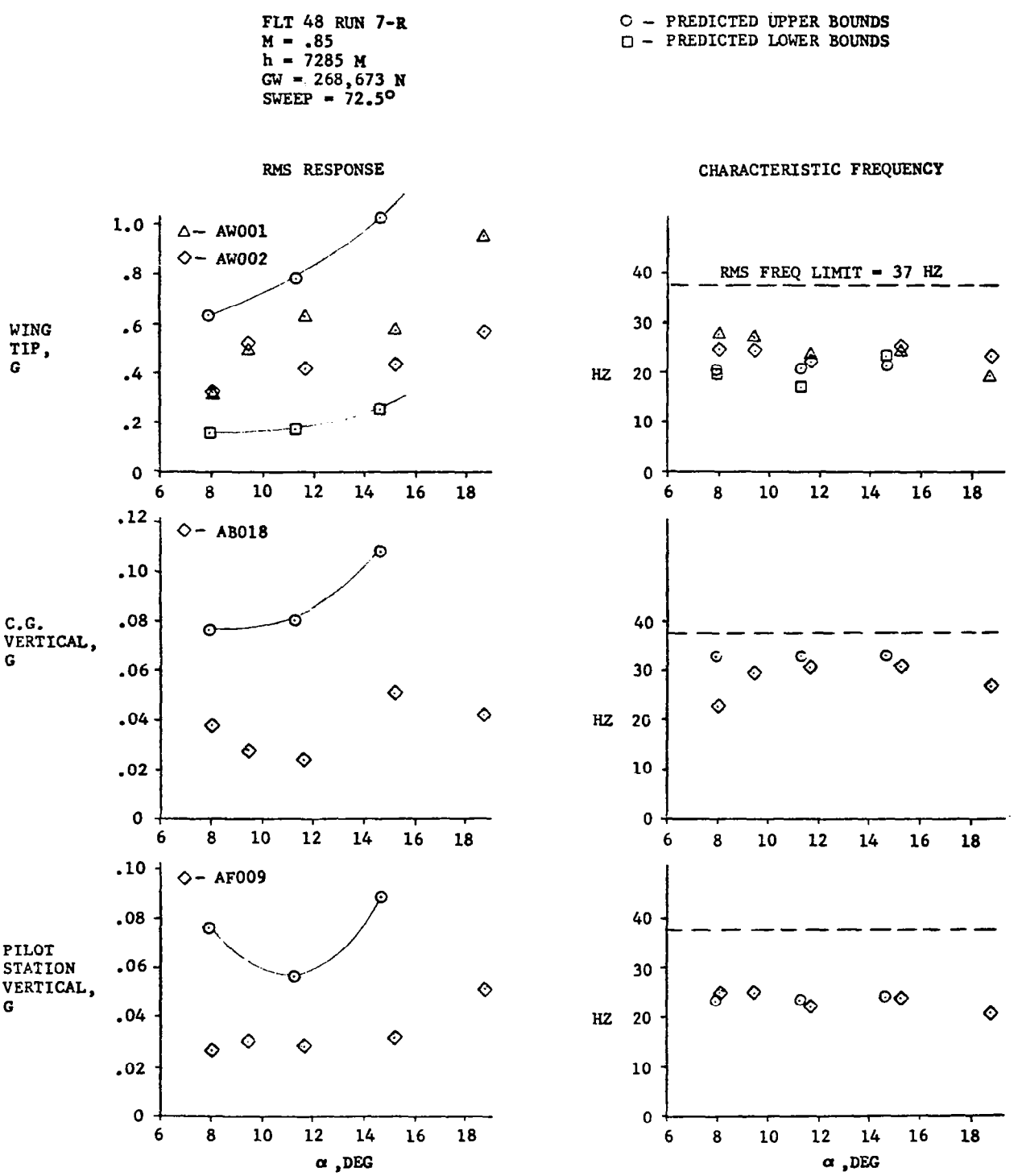

Figure 29.- Response predictions for case 5

FLT 48 RUN 7-R
M = .85
h = 7285 M
GW = 268,673 N
SWEEP = 72.5°

○ – PREDICTED UPPER BOUNDS
□ – PREDICTED LOWER BOUNDS

RMS RESPONSE

CHARACTERISTIC FREQUENCY

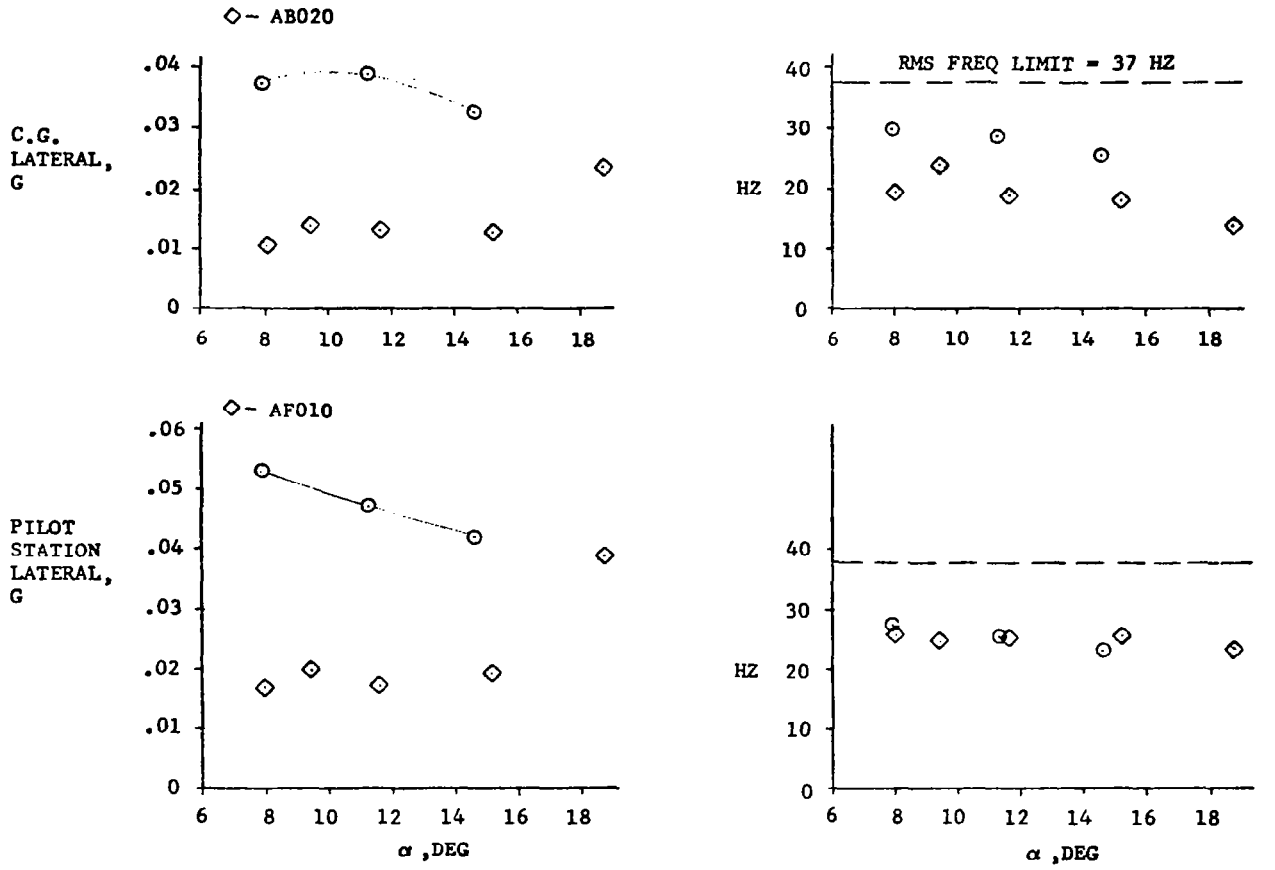

Figure 29.-(continued)

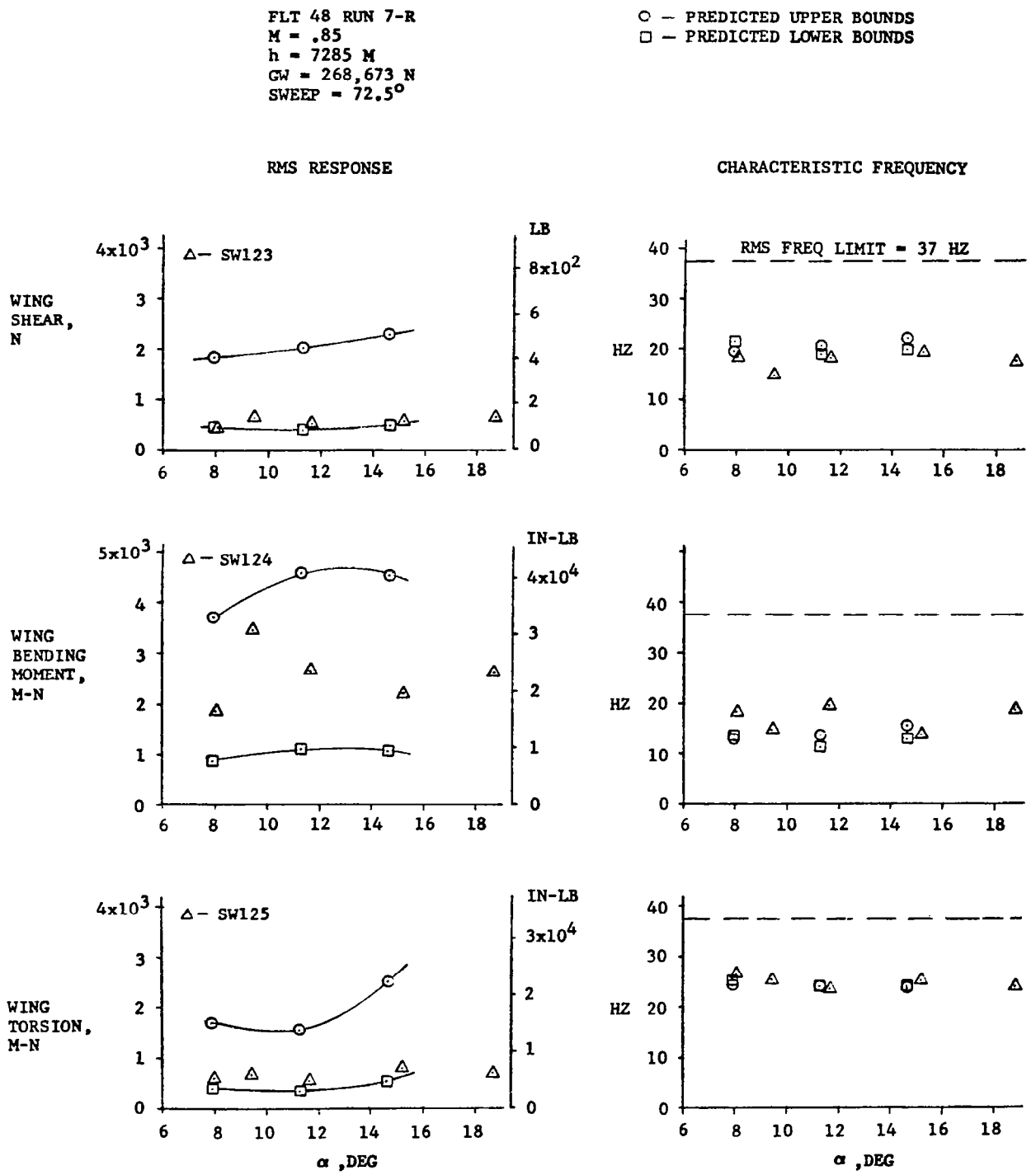

Figure 29.-(continued)

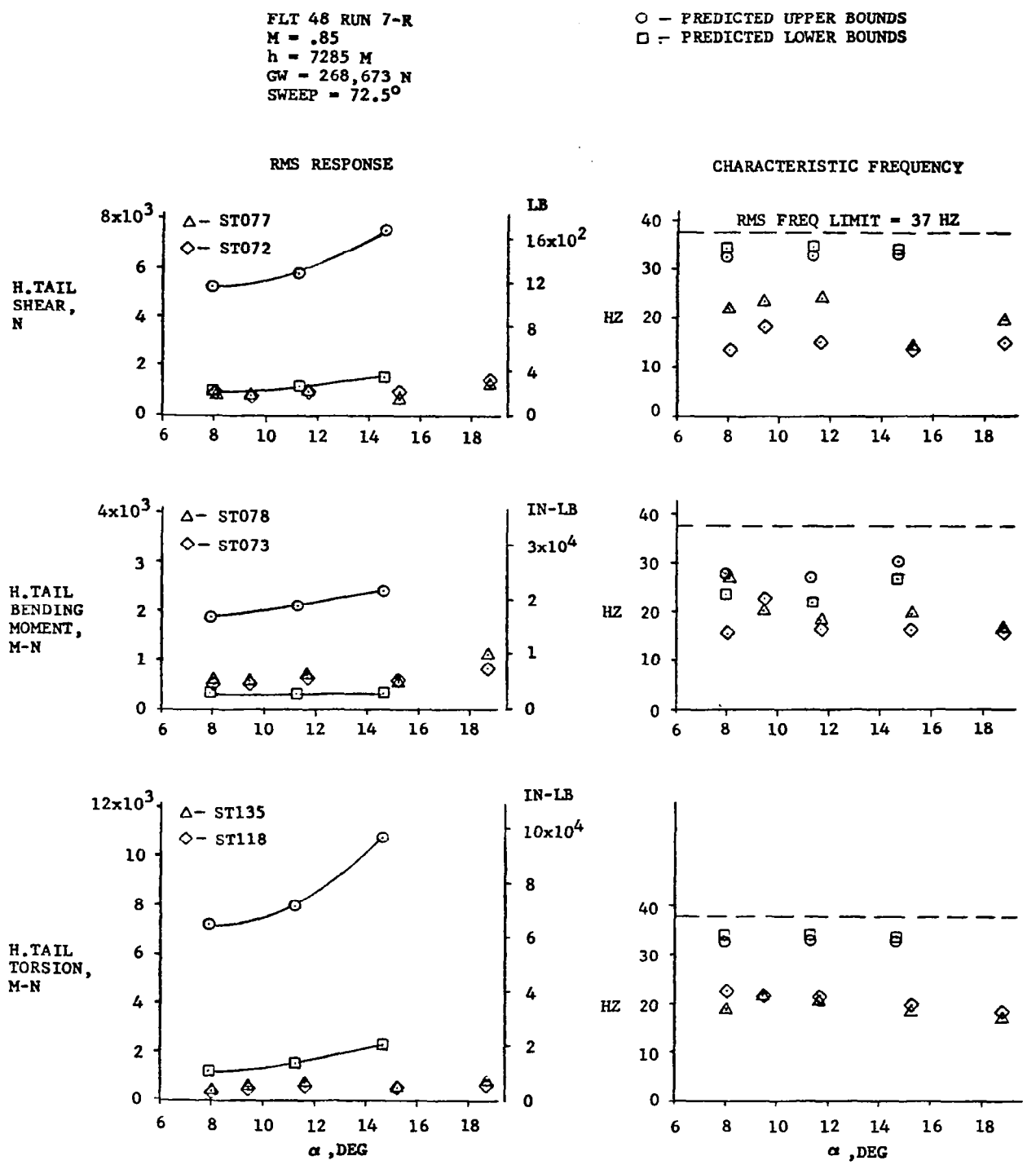

Figure 29.-(continued)

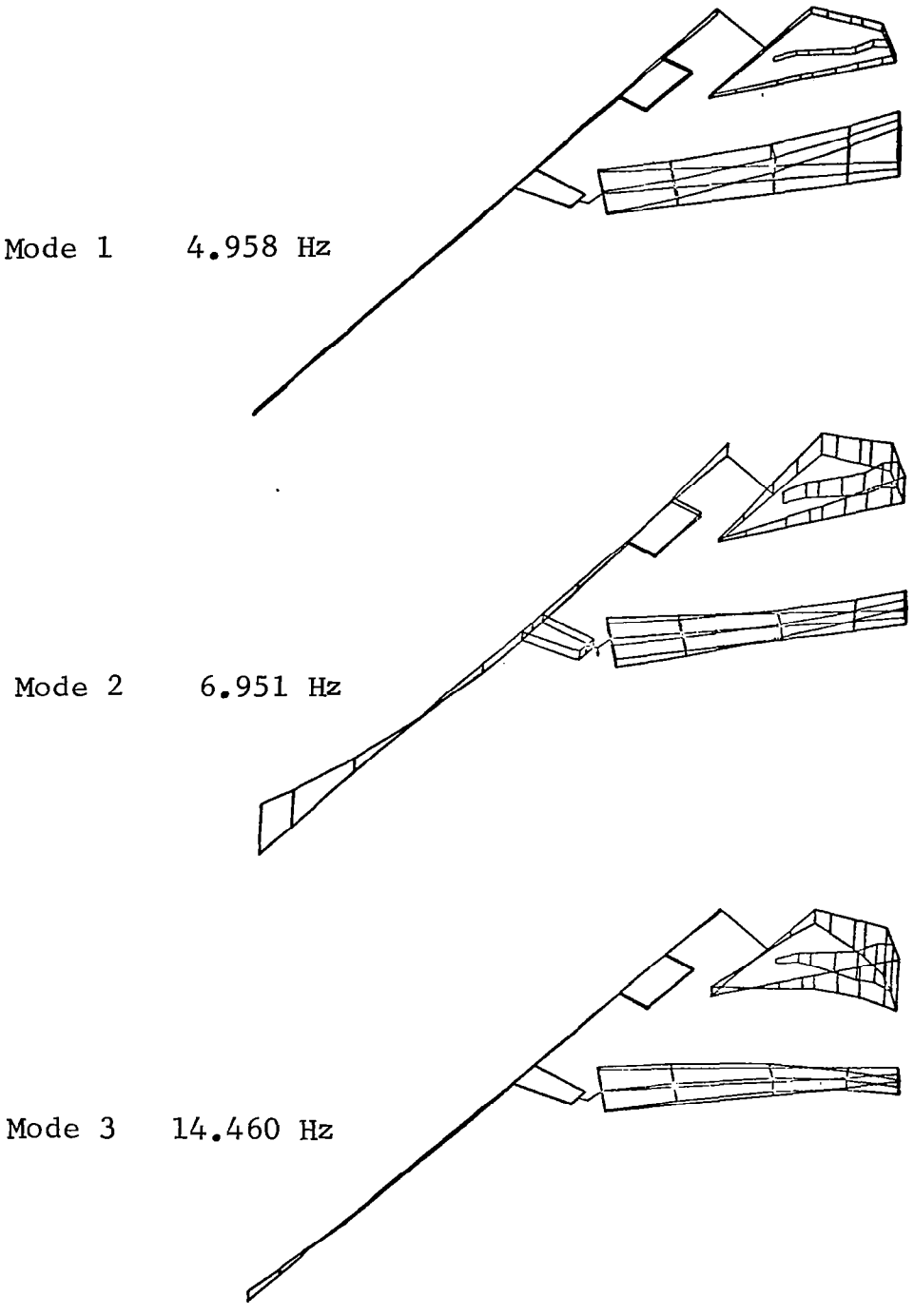

Figure 30.- Calculated symmetric natural modes for case 6, $\Lambda=50.0^{o}$ and G.W.=261,778N

Mode 4 15.372 Hz

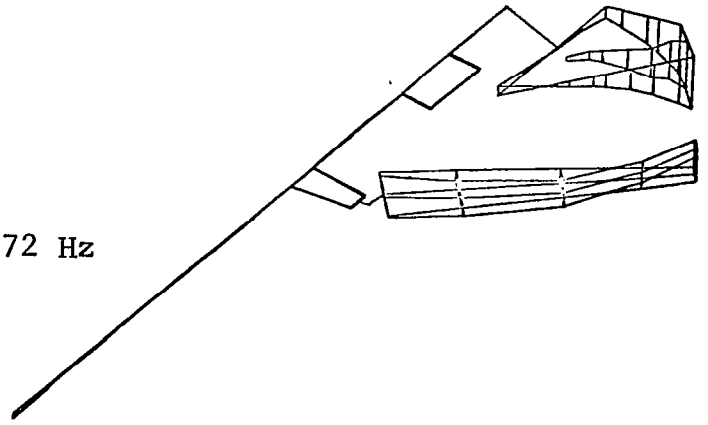

Mode 5 17.892 Hz

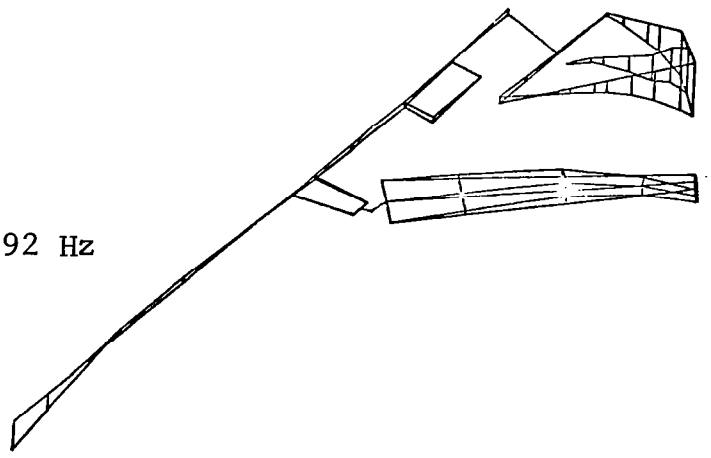

Mode 6 22.934 Hz

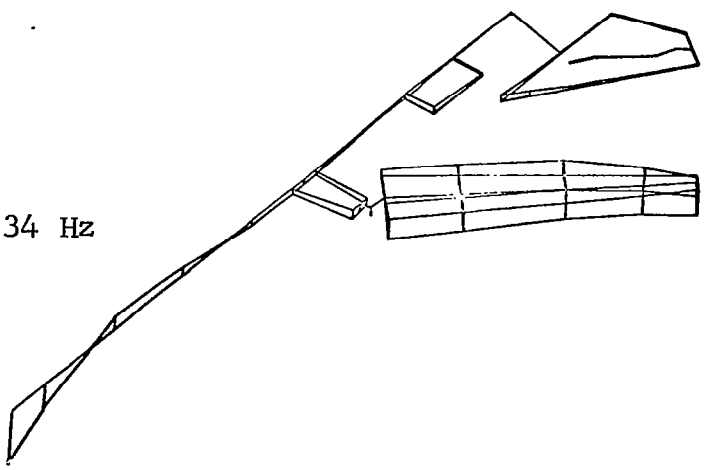

Figure 30.-(continued)

Mode 7 24.386 Hz

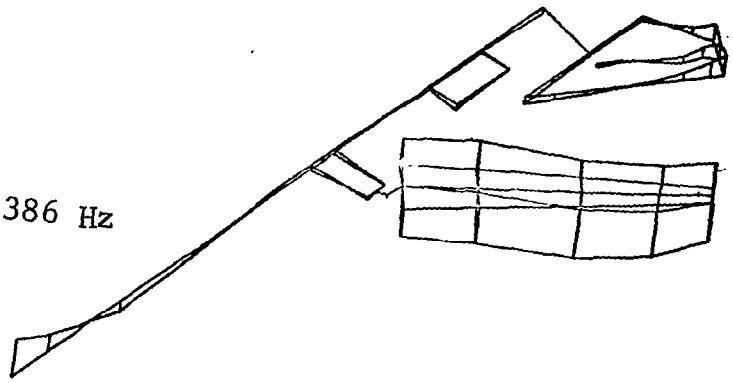

Mode 8 27.707 Hz

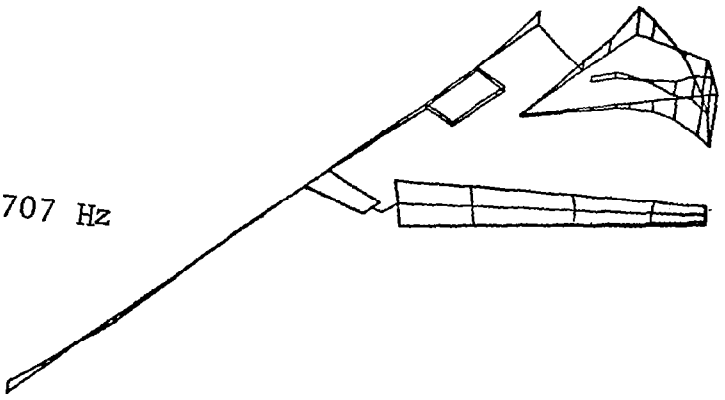

Mode 9 31.619 Hz

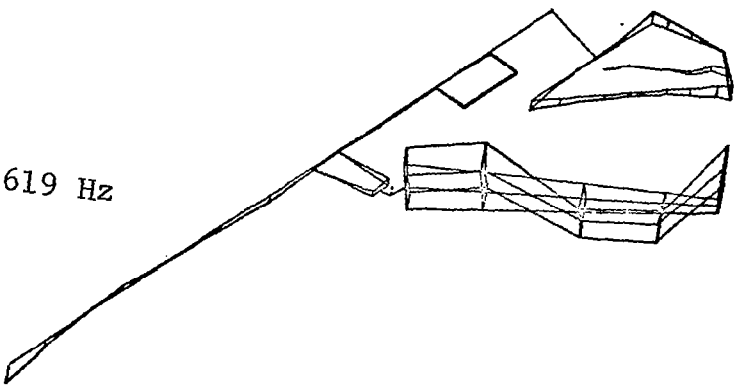

Figure 30.-(continued)

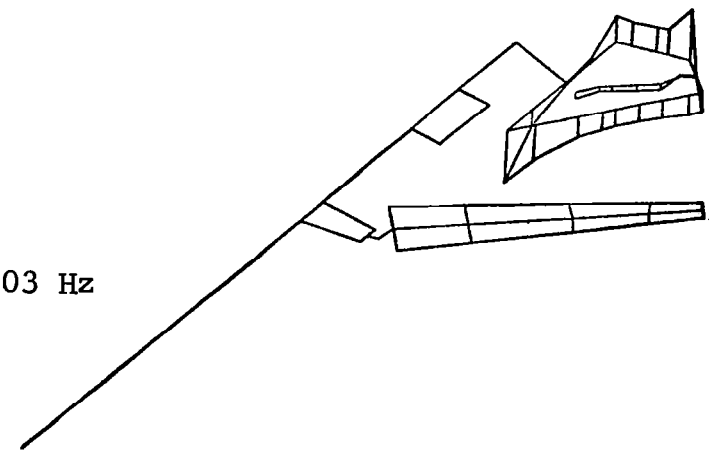

Mode 10 33.903 Hz

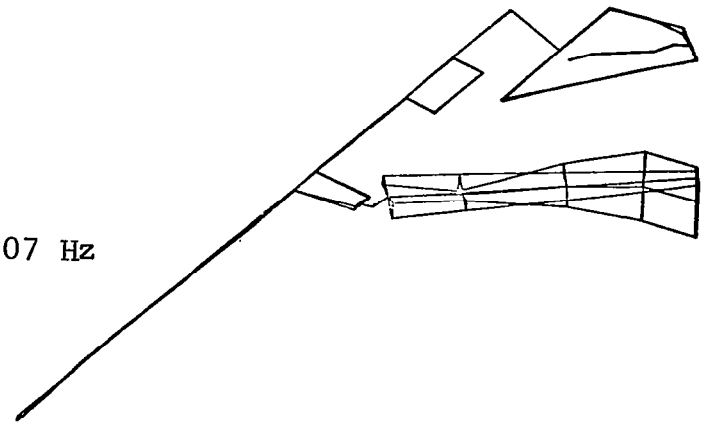

Mode 11 39.307 Hz

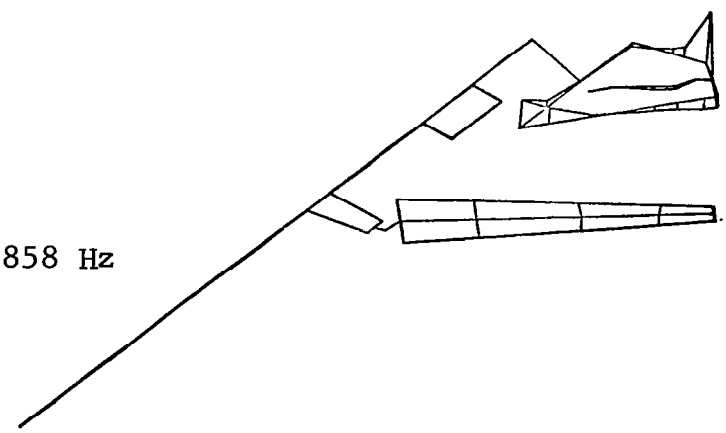

Mode 12 39.858 Hz

Figure 30.-(continued)

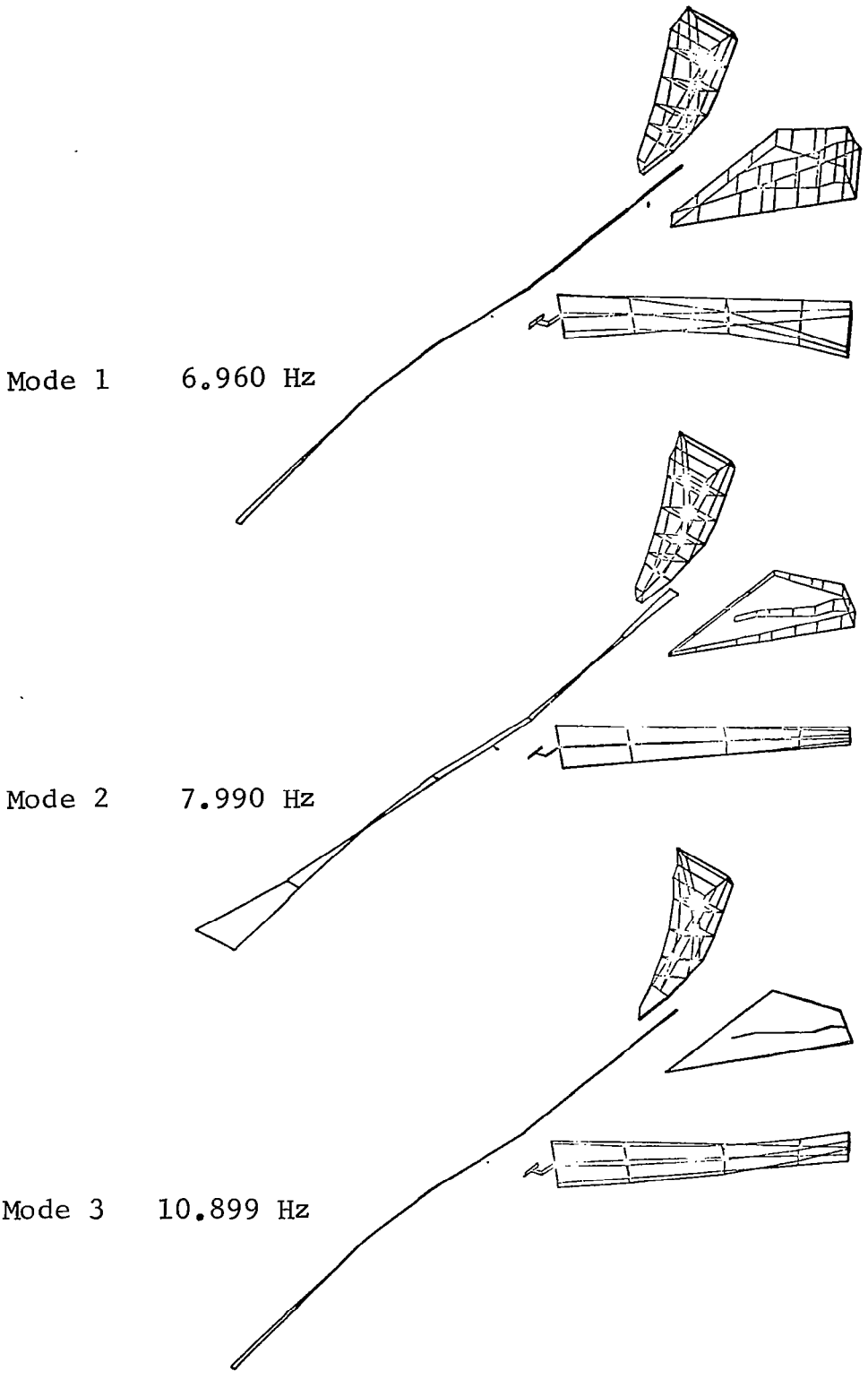

Figure 31.- Calculated antisymmetric natural modes for case 6, $\Lambda=50.0^{o}$ and G.W.=261,778N

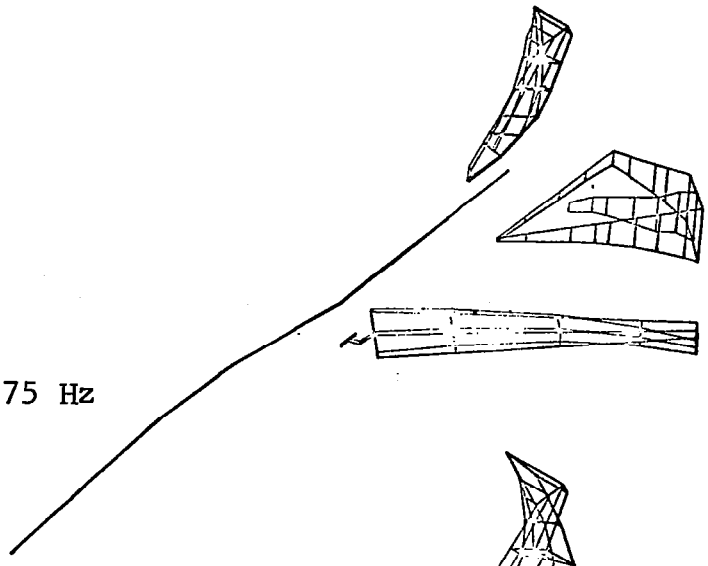

Mode 4 12.375 Hz

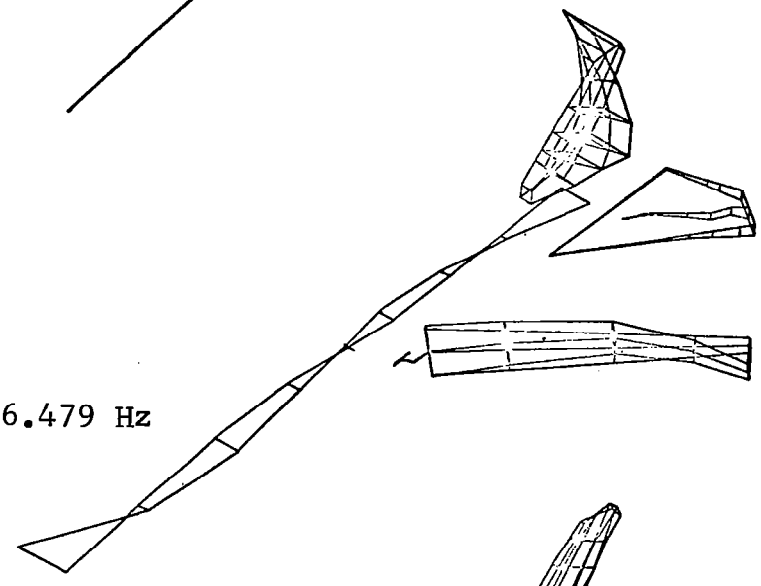

Mode 5 16.479 Hz

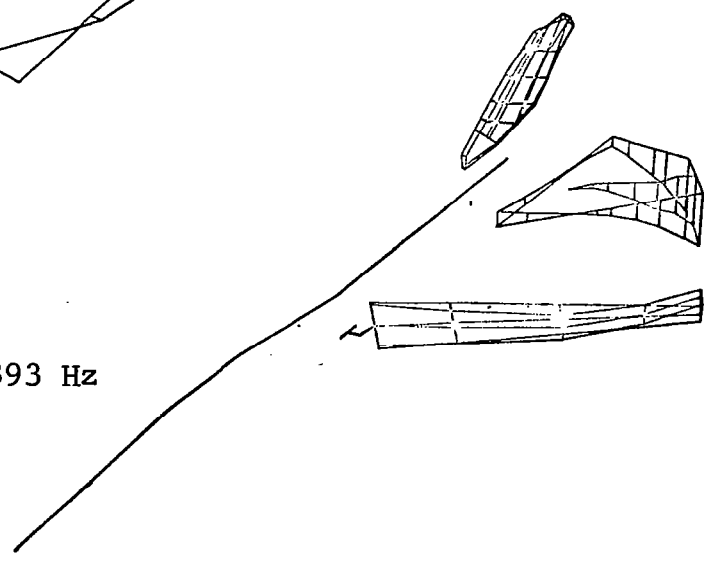

Mode 6 17.893 Hz

Figure 31.-(continued)

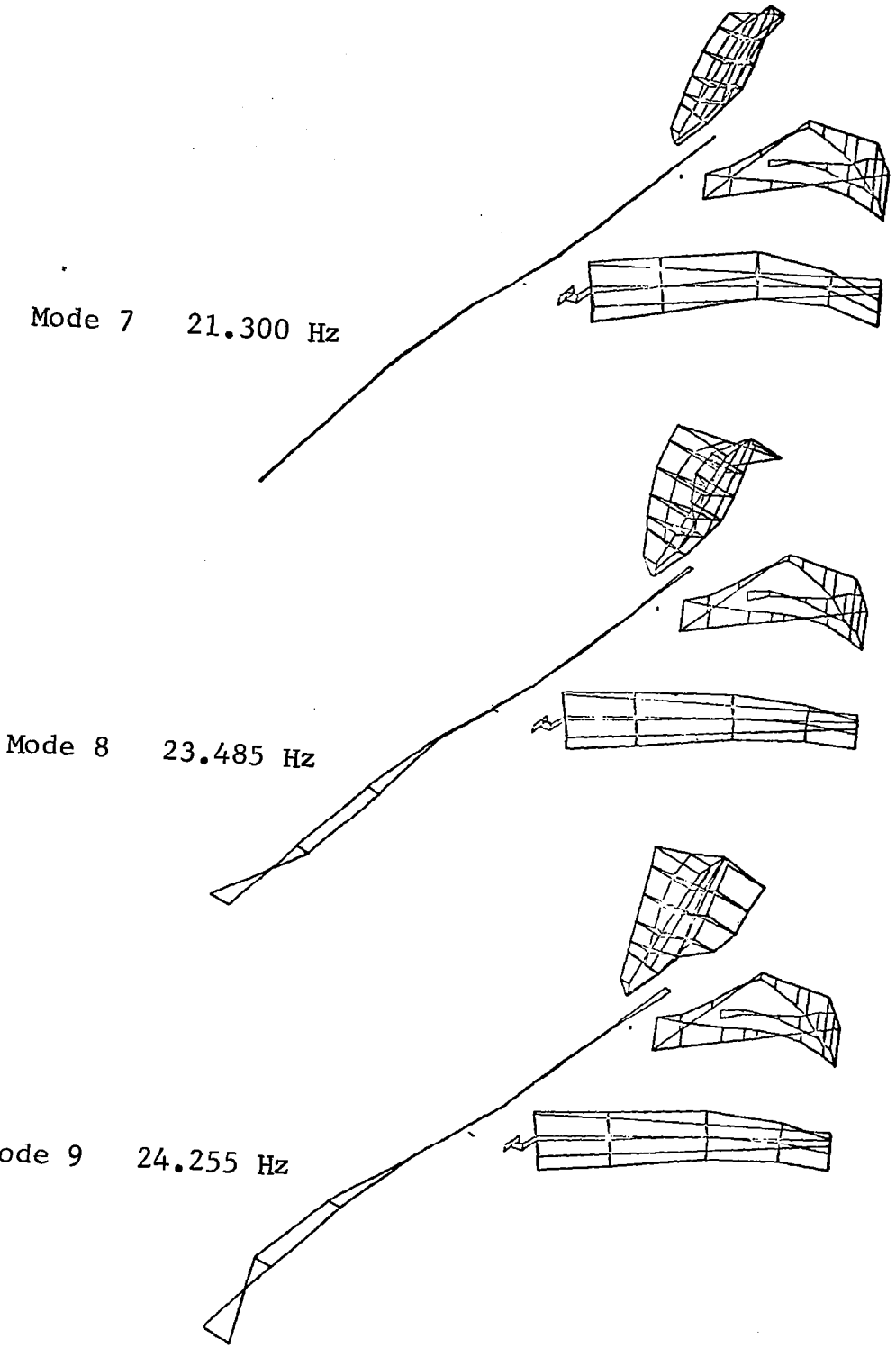

Figure 31.-(continued)

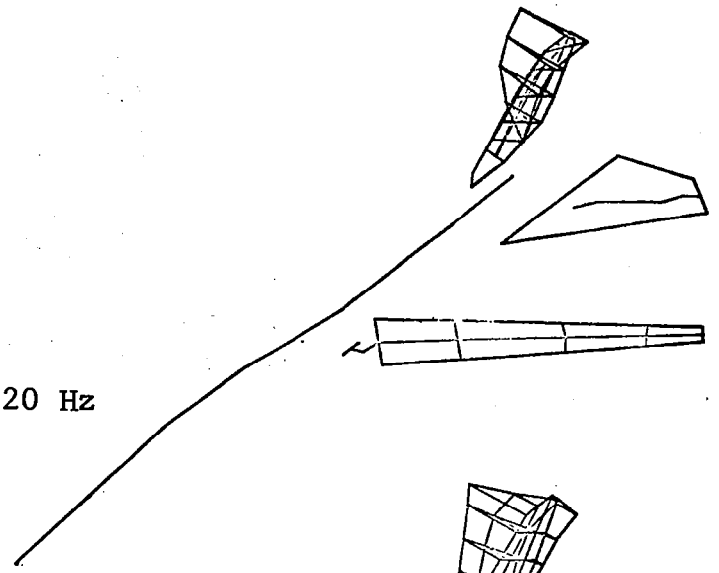

Mode 10 25.320 Hz

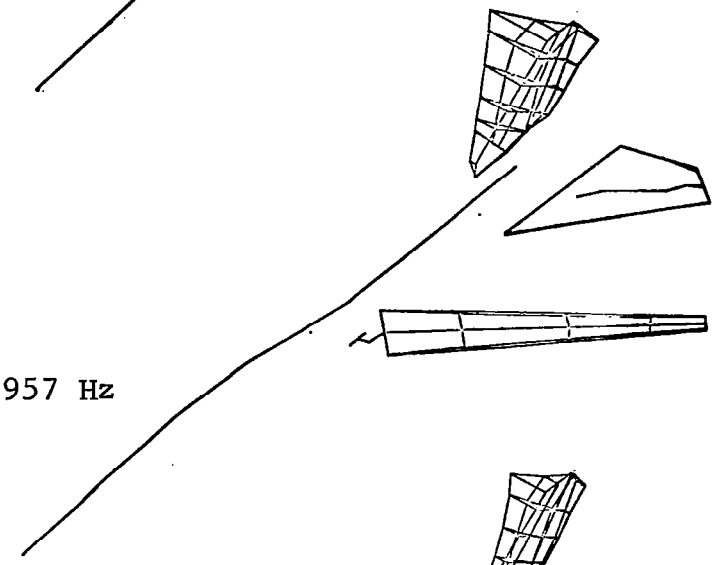

Mode 11 25.957 Hz

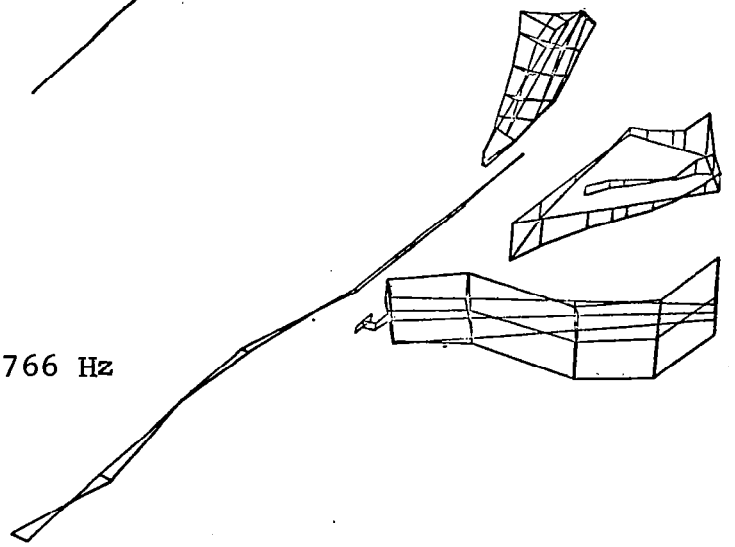

Mode 12 28.766 Hz

Figure 31.-(continued)

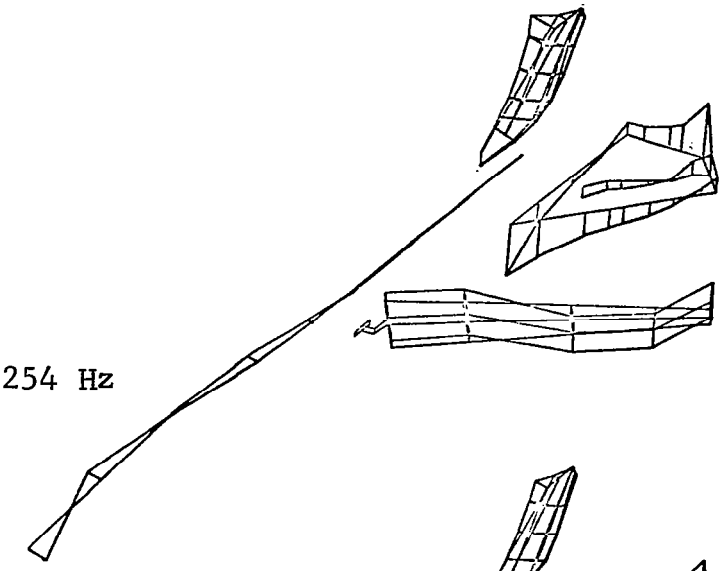

Mode 13 30.254 Hz

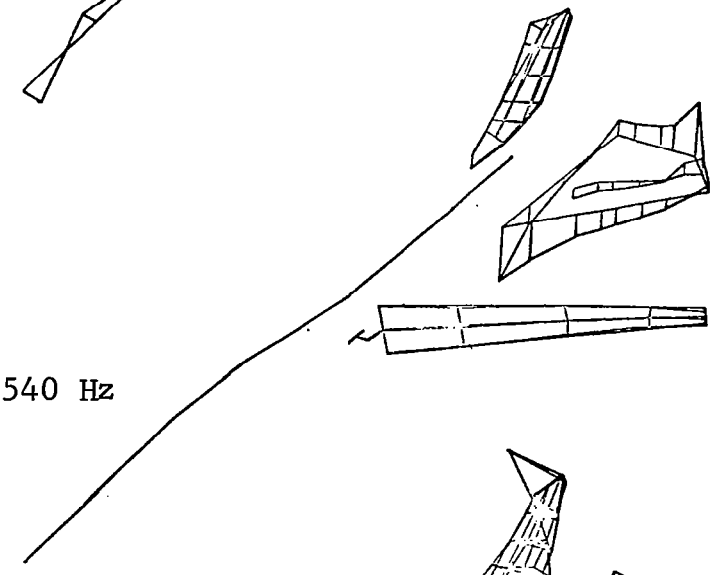

Mode 14 31.540 Hz

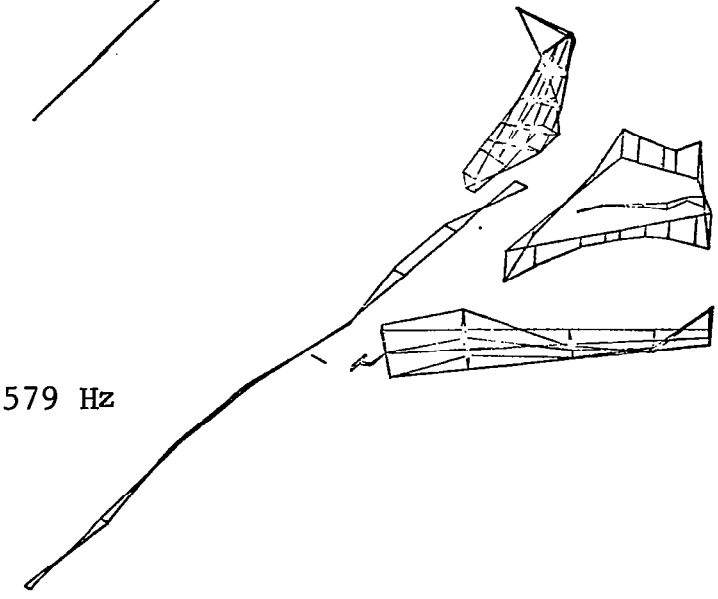

Mode 15 36.579 Hz

Figure 31.-(continued)

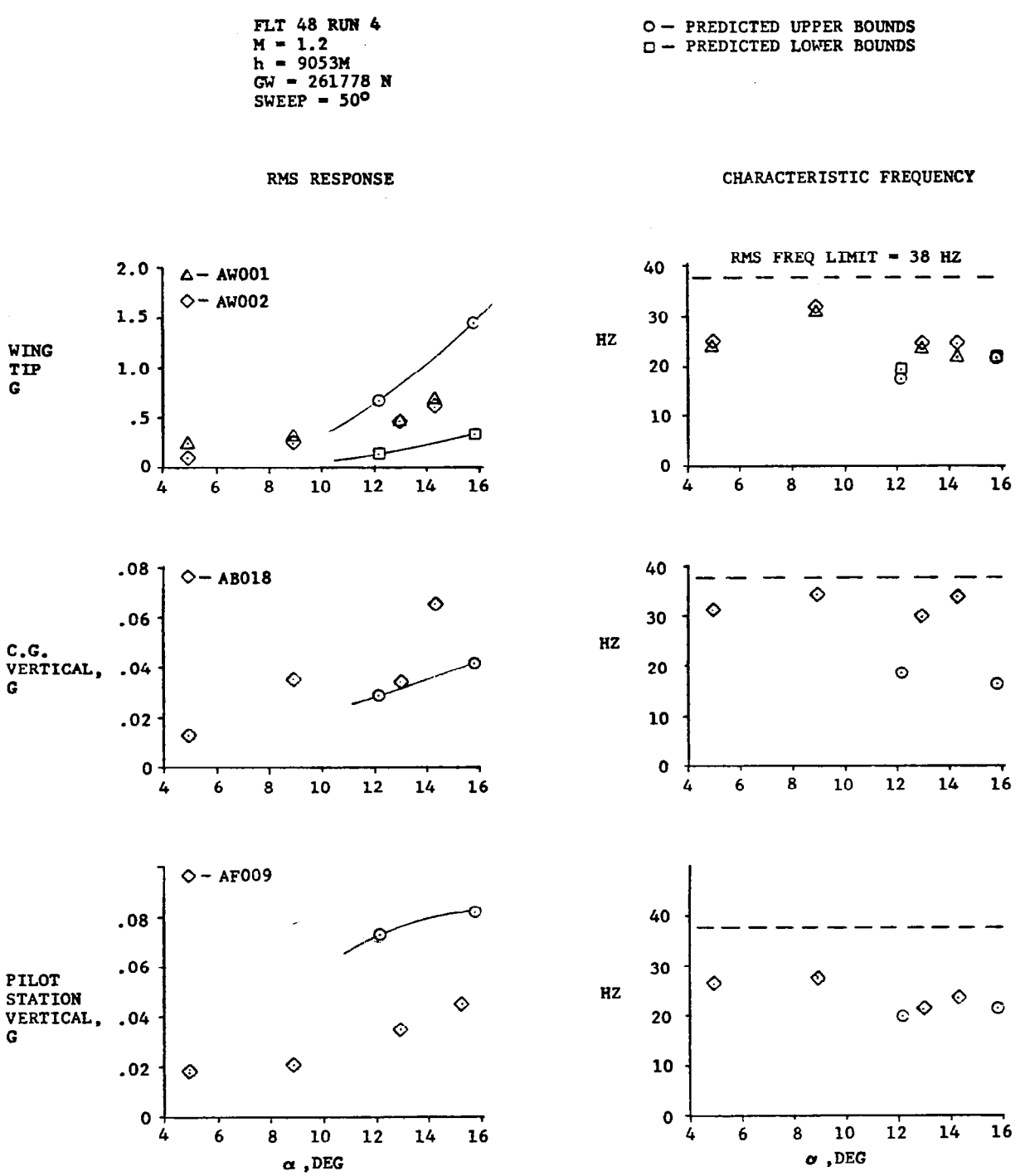

Figure 32.- Response predictions for case 6

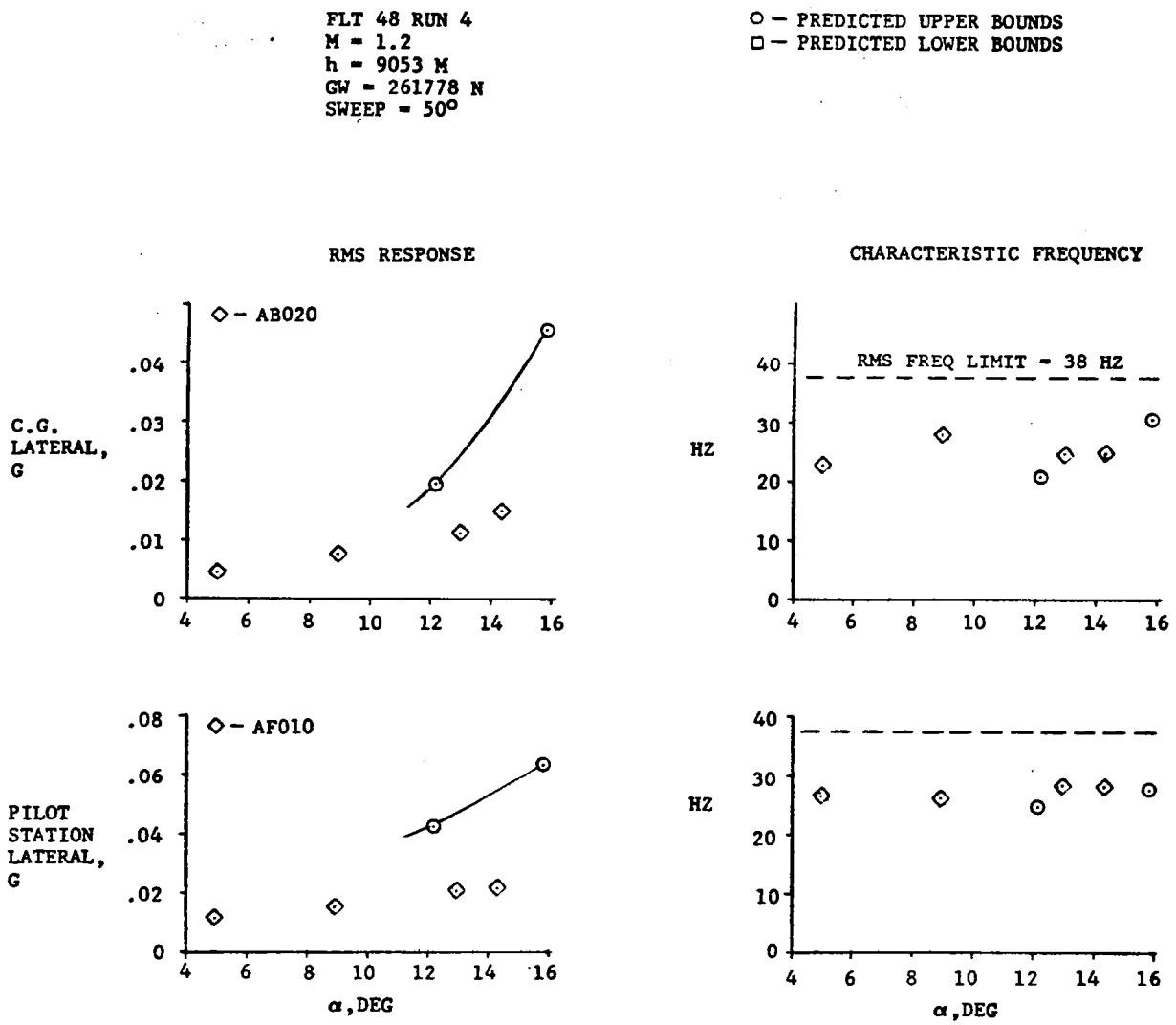

Figure 32.-(continued)

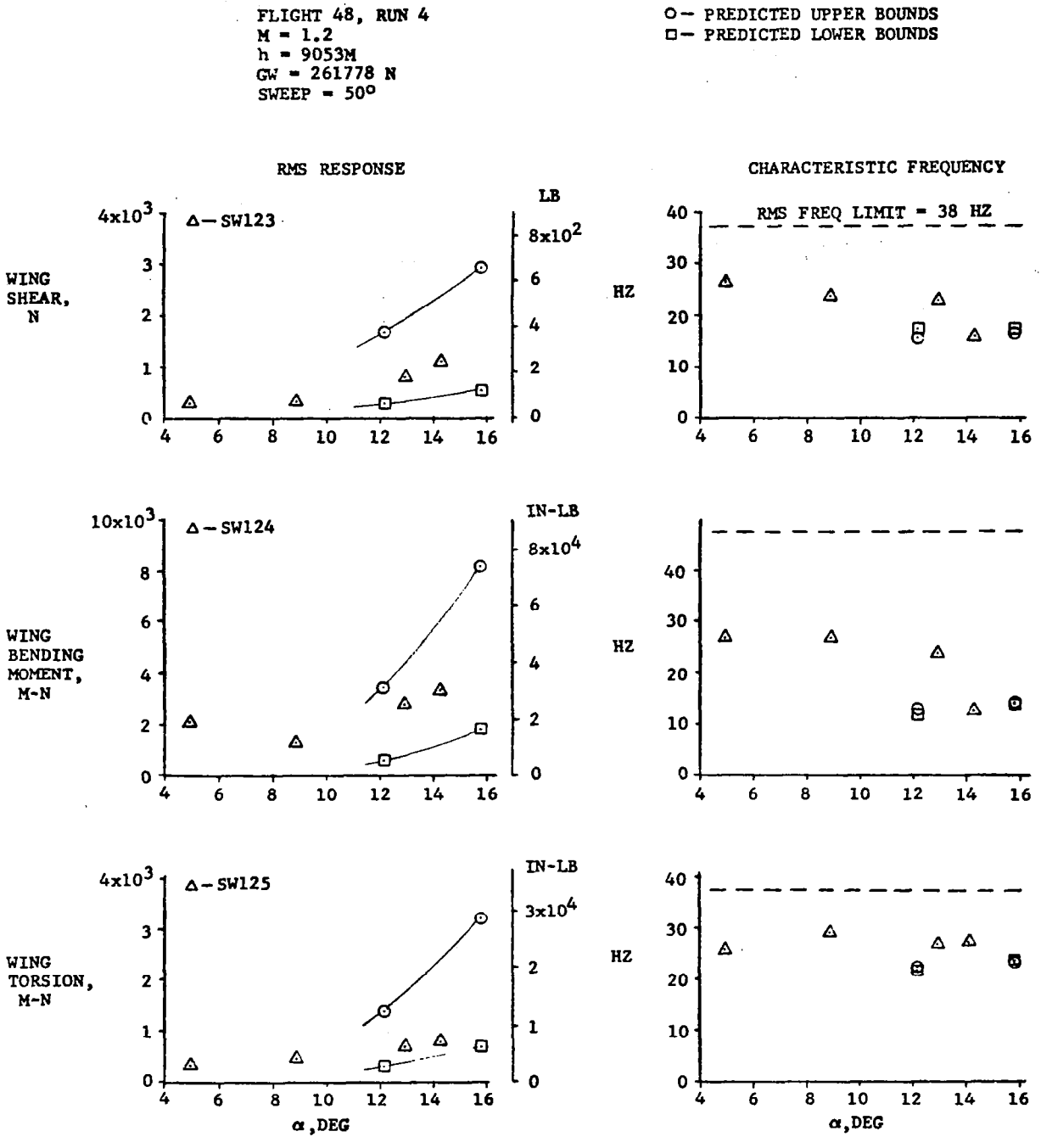

Figure 32.-(continued)

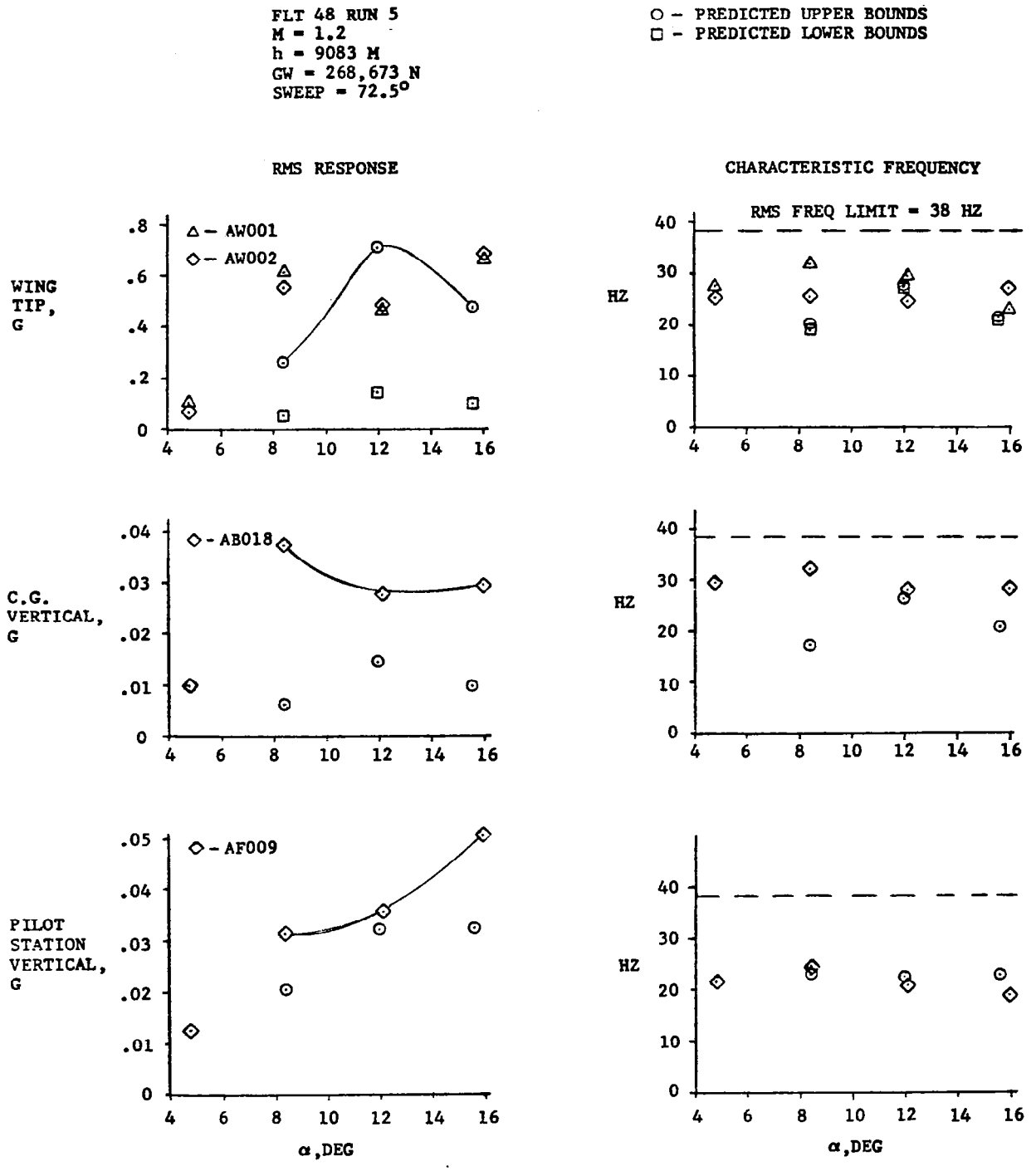

Figure 33.- Response predictions for case 7

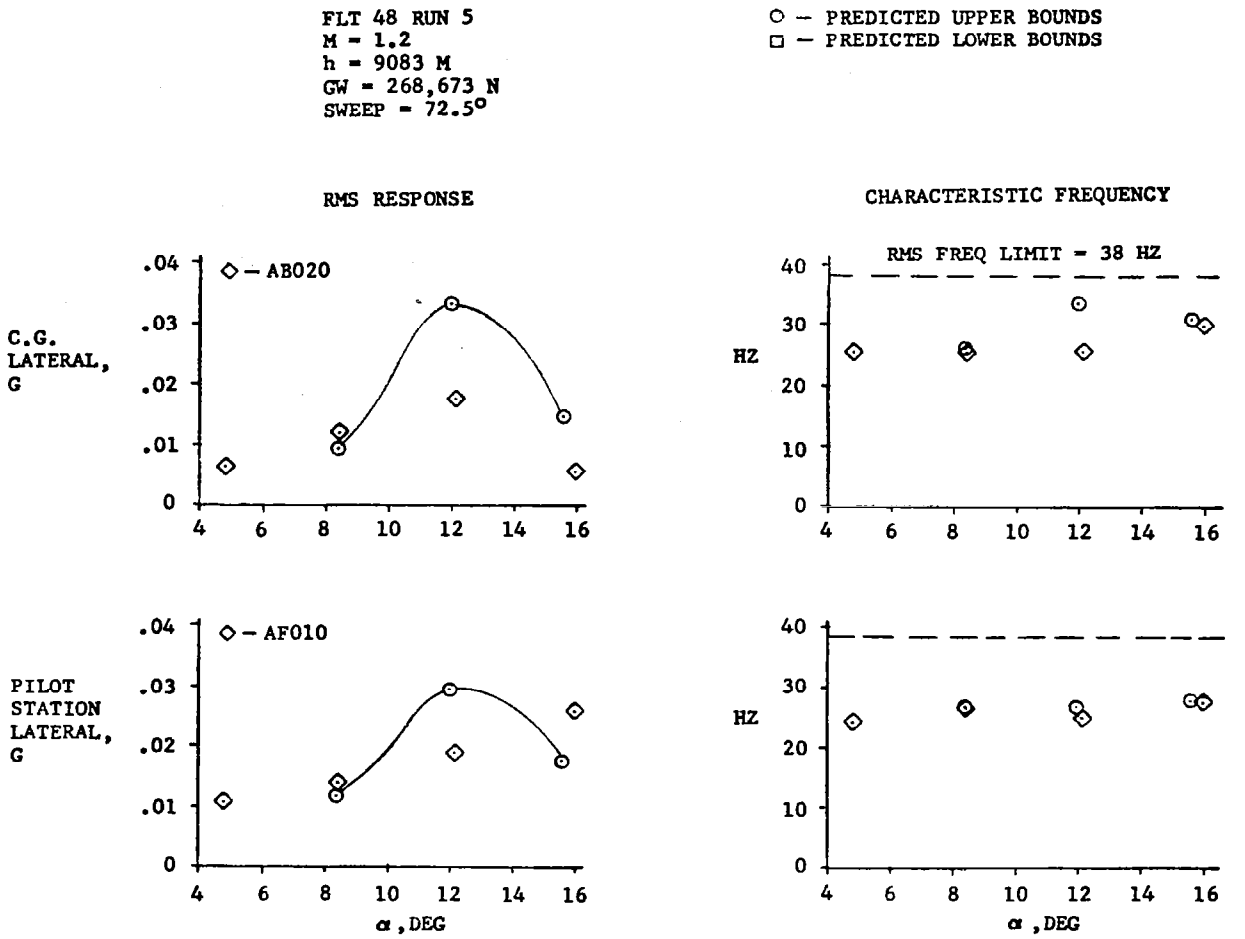

Figure 33.-(continued)

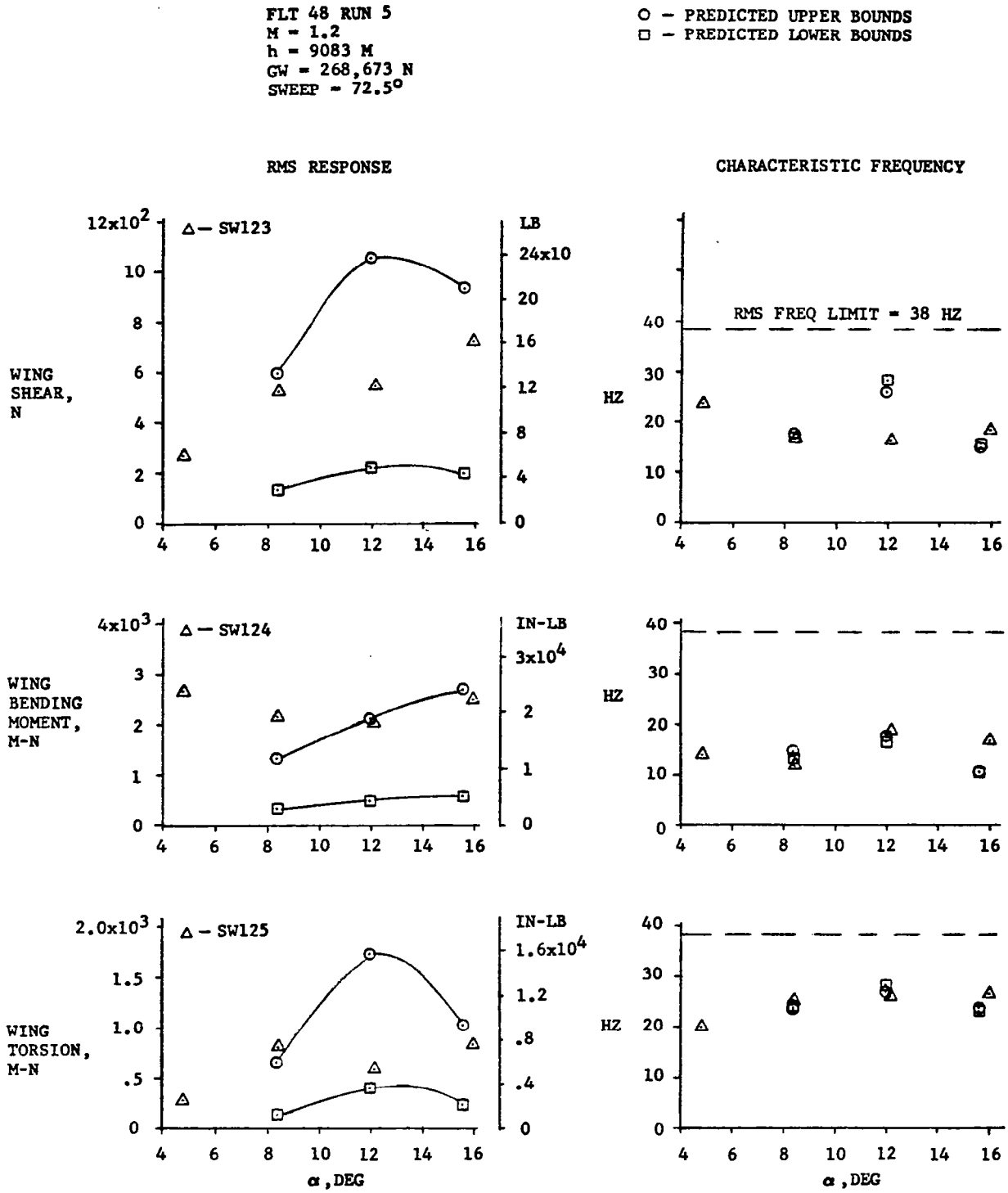

Figure 33.-(continued)

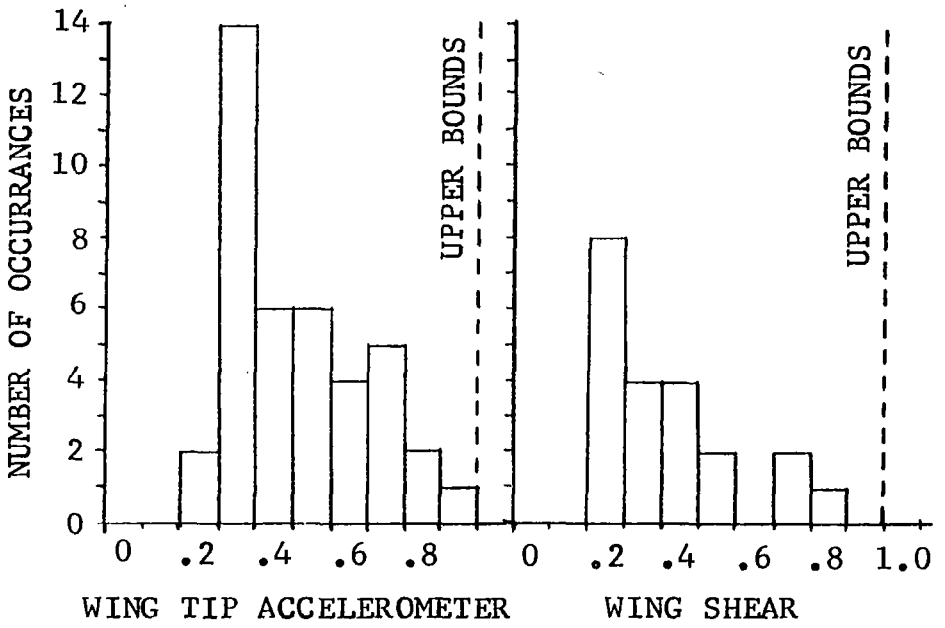

Figure 34.- Frequency of flight test data distribution as fraction of upper bounds